Control of Synchronous Motor Drives with an LC Filter

Roman Suran

School of Electrical Engineering

Thesis submitted for examination for the degree of Master of Science in Technology.

Espoo August 21, 2022

Supervisor

Prof. Marko Hinkkanen

Advisor

MSc.(Tech.) Lauri Tiitinen

Aalto University
School of Electrical
Engineering

Aalto University
School of Electrical
Engineering

Aalto University, P.O. BOX 11000, 00076 AALTO
www.aalto.fi
Abstract of the master's thesis

Author Roman Suran

Title Control of Synchronous Motor Drives with an LC Filter

Degree programme Electronics and electrical engineering

Major Electrical Power and Energy Engineering **Code of major** ELEC3024

Supervisor Prof. Marko Hinkkanen

Advisor MSc.(Tech.) Lauri Tiitinen

Date August 21, 2022 **Number of pages** 71+3 **Language** English

Abstract

Electric motors can experience voltage stress over the motor terminals due to the short rise time of the voltage pulse at the inverter output and the impedance mismatch between the lead cables and the motor. This overvoltage degrades the motor insulation, thus reducing the motor lifespan. The problems can be avoided by using a sinusoidal LC filter in the inverter output, limiting the overvoltage and dampening high-order harmonics. However, the existing control methods for LC-filtered synchronous motors are infeasible for plug-and-play drives, in which the motor data or user input are not required. This is because the methods either contain several cascaded control loops, require cumbersome parameter tuning, are sensitive to parameter errors, or the range of operating speeds is limited. Nevertheless, recently developed observer-based volts-per-hertz control shows advantages through relatively low sensitivity to parameter errors, simplicity and generality of the control algorithm, and reliance on common control gains for all synchronous motor types. These attributes indicate that the observer-based volts-per-hertz control can be used for medium-performance drives ensuring robust and stable operation at a wide range of speeds. This thesis develops observer-based volts-per-hertz control for synchronous motor drives with an LC filter. The two designed methods are based on two different observer types (reduced-order and full-order) with two state feedback control laws. The methods are further linearized by means of small-signal linearization, the control strategies are simulated in Simulink, and experimental measurements validate the simulations. The measurement results show a satisfactory performance of the permanent magnet synchronous motor with both methods. However, the control performance of the synchronous reluctance motor is poor when the full-order observer is used. The thesis subsequently provides several suggestions for future work improvements.

Keywords LC filter, observer, sensorless, state feedback, synchronous motor, V/Hz control

Preface

This thesis work has been conducted at Aalto University in the department of Electrical Engineering and Automation between January 2022 and August 2022. This project was funded by Aalto University and ABB Oy Drives in Helsinki as a part of ongoing research for sensorless AC drives.

I would like to express my deepest gratitude to my supervisor Professor Marko Hinkkanen and instructor MSc. Lauri Tiitinen for an excellent opportunity to work on this research topic. I would like to thank them for their professional guidance, valuable feedback and helpful corrections in academic writing. I would also like to thank Aalto University and ABB for funding this project.

Espoo, August 21, 2022

Roman Suran

Contents

Symbols and abbreviations

Latin symbols

Scalars

C_f	filter capacitance
$\hat{C}_\mathrm{f}$	estimated filter capacitance
$d_\mathrm{a}, d_\mathrm{b}, d_\mathrm{c}$	duty ratios
f_r	resonance frequency
f_s	sampling frequency
$F(s)$	transfer function of HPF
g	LC filter damping gain
g_τ	damping of the HPF using $\hat{\tau}_\mathrm{m}$
i_α, i_β	real and imaginary components of current space vector in stator coordinates
$i_\mathrm{a}, i_\mathrm{b}, i_\mathrm{c}$	stator phase currents
$i_\mathrm{d}, i_\mathrm{q}$	real-valued components of current space vector in rotor coordinates
$i_\mathrm{sx}, i_\mathrm{sy}$	real-valued components of stator current vector in control coordinates
$i_\mathrm{cx}, i_\mathrm{cy}$	real-valued components of converter current vector in control coordinates
i_F	field current of the rotor winding
J_m	total moment of inertia
$L_\mathrm{d}, L_\mathrm{q}$	stator inductance components in rotor coordinates
$\hat{L}_\mathrm{d}$	estimated stator d-component inductance
L_f	filter inductance
$\hat{L}_\mathrm{f}$	estimated filter inductance
p	number of pole pairs
$q_\mathrm{a}, q_\mathrm{b}, q_\mathrm{c}$	switching vector elements
R_f	filter resistance
$\hat{R}_\mathrm{f}$	estimated filter resistance
R_s	resistance of the stator winding
$\hat{R}_\mathrm{s}$	estimated stator resistance
t	time
T_s	sampling period
T_sw	switching period
$u_\mathrm{aN}, u_\mathrm{bN}, u_\mathrm{cN}$	phase voltages with respect to negative DC bus
$u_\mathrm{d}, u_\mathrm{q}$	real-valued components of voltage space vector in rotor coordinates
u_DC	DC bus voltage
$u_\mathrm{sx}, u_\mathrm{sy}$	real-valued components of voltage space vector in control coordinates
u_LL	line-to-line voltage

Vectors

$\boldsymbol{a}_\delta$	vector used in the linearized LPF expression
$\boldsymbol{a}_\omega$	vector used in the linearized mechanical dynamics expression
$\boldsymbol{b}_{\mathbf{m}}$, $\boldsymbol{b}_{\mathbf{mo}}$, $\boldsymbol{b}_{\mathbf{s}\omega}$	input vectors for $\Delta\omega_\mathrm{m}$
$\boldsymbol{b}_\omega$, $\boldsymbol{b}_\mathrm{c}$, $\boldsymbol{b}_\mathrm{o}$, $\boldsymbol{b}_{\mathbf{s}\omega,\mathbf{ref}}$, $\boldsymbol{b}_\mathrm{M}$	input vectors for $\Delta\omega_\mathrm{c}$
$\boldsymbol{b}_\tau$	input vector for $\Delta\tau_\mathrm{L}$
$\boldsymbol{c}_\tau^\mathrm{T}$	output vector for $\Delta\tau_\mathrm{m}$
$\boldsymbol{d}_\mathrm{abc}$	duty ratios column vector
$\boldsymbol{e}$	correction vector
$\boldsymbol{i}_\mathrm{c}$	converter current in control coordinates
$\boldsymbol{i}_\mathrm{c0}$	operating point converter current
$\tilde{\boldsymbol{i}}_\mathrm{c}$	converter current estimation-error
$\hat{\boldsymbol{i}}_\mathrm{c}$	estimated converter current
$\boldsymbol{i}_\mathrm{s}$	stator current in control coordinates
$\boldsymbol{i}_\mathrm{s0}$	operating point stator current
$\hat{\boldsymbol{i}}_\mathrm{s}$	estimated stator current
$\boldsymbol{i}_\mathrm{s}^\mathrm{s}$	stator current in stator coordinates
$\boldsymbol{k}$	input vector in state feedback for $\Delta\omega_\mathrm{c}$
$\boldsymbol{k}_\mathrm{o}^\mathrm{T}$	observer gain vector of the load angle
$\boldsymbol{k}_\sigma^\mathrm{T}$	state vector of linearized HPF
$\boldsymbol{q}_\mathrm{abc}$	switching states column vector
$\boldsymbol{u}_\mathrm{c}$	converter voltage in control coordinates
$\boldsymbol{u}_\mathrm{c0}$	operating point converter voltage
$\boldsymbol{u}_\mathrm{c,ref}$	converter voltage reference in control coordinates
$\boldsymbol{u}_\mathrm{c}^\mathrm{s}$	converter voltage in stator coordinates
$\boldsymbol{u}_\mathrm{s}$	stator voltage in control coordinates
$\tilde{\boldsymbol{u}}_\mathrm{s}$	stator voltage estimation-error
$\boldsymbol{u}_\mathrm{s0}$	operating point stator voltage
$\hat{\boldsymbol{u}}_\mathrm{s}$	estimated stator voltage
$\boldsymbol{u}_\mathrm{s,ref}$	stator voltage reference in control coordinates
$\boldsymbol{u}_\mathrm{s,ref}^\mathrm{s}$	stator voltage reference in stator coordinates
$\boldsymbol{x}$	state vector
$\tilde{\boldsymbol{x}}$	observer error state vector
$\boldsymbol{x}_\mathrm{s}$	state vector of the overall system without mechanical and LPF dynamics
$\boldsymbol{x}_\mathrm{T}$	state vector of the final system with mechanical and LPF dynamics

Matrices

$\boldsymbol{A}$	system matrix of the plant model
$\boldsymbol{A}_{\mathrm{c}}$	system matrix of the closed-loop system (plant model with state feedback)
$\boldsymbol{A}_{\mathrm{M}}$	system matrix of the pre-final closed-loop system (without HPF)
$\boldsymbol{A}_{\mathrm{o}}$	system matrix of the observer model
$\boldsymbol{A}_{\mathrm{s}}$	system matrix of the closed-loop system (plant model with state feedback and observer model)
$\boldsymbol{A}_{\mathrm{T}}$	system matrix of the final closed-loop system
$\boldsymbol{B}$	input matrix of the plant model
$\boldsymbol{B}_{\psi}$	input matrix for flux reference
$\boldsymbol{C}$	output matrix for converter flux linkage
$\mathbf{I}$	identity matrix 2X2
$\mathbf{I}_{\mathrm{m}}$	identity matrix with dimensions mXm
$\mathbf{J}$	rotational matrix
$\boldsymbol{K}$	state matrix of state feedback control law
$\tilde{\boldsymbol{K}}$	observer-error state matrix of state feedback control law
$\boldsymbol{K}_{\mathrm{c}}$	state feedback control gain
$\boldsymbol{K}_{\mathrm{L}}$	converter current observer gain
$\boldsymbol{K}_{\mathrm{o}}$	flux observer gain
$\boldsymbol{K}_{\mathbf{t}}$	input matrix of state feedback for $\Delta\boldsymbol{\psi}_{\mathrm{c,ref}}$
$\boldsymbol{L}_{\mathrm{s}}$	stator inductance
$\boldsymbol{L}_{\mathrm{s0}}$	operating point stator inductance
$\boldsymbol{L}_{\mathrm{sys}}$	equivalent system inductance
$\mathbf{0}$	zero matrix 2X2
$\mathbf{0}_{\mathrm{m,n}}$	zero matrix with dimensions mXn

Greek symbols

Scalars

α_c	closed-loop controller bandwidth
α_f	bandwidth of low-pass filter (as a part of HPF)
α_L	converter current estimation bandwidth
α_o	load angle estimation bandwidth
α_ω	damping gain of HPF using $\hat{\delta}$
δ	load angle
δ_0	operating point load angle
$\tilde{\delta}$	load angle estimation-error
$\hat{\delta}$	estimated load angle
ζ_∞	damping ratio for flux observer
ϑ_c	electrical angle of the coordinate system (with LC filter)
ϑ_m	electrical angle of the rotor
ϑ_s	electrical angle of the coordinate system (without LC filter)
σ_o	decay rate of the flux estimation error
τ_L	motor load torque
τ_m	electromagnetic torque of the motor
$\hat{\tau}_\mathrm{m}$	estimated electromagnetic torque
τ_ref	low-pass-filtered torque estimate
ψ_f	permanent magnet flux linkage
$\psi_\mathrm{d}, \psi_\mathrm{q}$	real-valued components of voltage space vector in rotor coordinates
$\psi_\mathrm{sx}, \psi_\mathrm{sy}$	real-valued components of voltage space vector in control coordinates
ω_c	angular speed of the control coordinate system (with LC filter)
ω_c0	operating point angular speed
ω_m	angular rotor speed
ω_n	rated angular rotor speed
$\omega_\mathrm{m,ref}$	reference of angular speed of the rotor
ω_r	resonance frequency of the LC filter in radians
ω_s	angular speed of the control coordinate system (without LC filter)

Vectors

$\hat{\boldsymbol{\psi}}_{\mathrm{a}}$	auxiliary flux linkage
$\boldsymbol{\psi}_{\mathrm{a0}}$	operating point of auxiliary flux linkage
$\boldsymbol{\psi}_{\mathrm{c}}$	converter flux linkage in control coordinates
$\boldsymbol{\psi}_{\mathrm{c0}}$	operating point converter flux linkage
$\tilde{\boldsymbol{\psi}}_{\mathrm{c}}$	converter flux linkage estimation-error
$\hat{\boldsymbol{\psi}}_{\mathrm{c}}$	estimated converter flux linkage
$\boldsymbol{\psi}_{\mathrm{F}}$	permanent magnet flux linkage
$\boldsymbol{\psi}_{\mathrm{f0}}$	operating point permanent magnet flux linkage
$\boldsymbol{\psi}_{\mathrm{s}}$	stator flux linkage in control coordinates
$\boldsymbol{\psi}_{\mathrm{s0}}$	operating point stator flux linkage
$\hat{\boldsymbol{\psi}}_{\mathrm{c}}$	estimated converter flux linkage
$\hat{\boldsymbol{\psi}}_{\mathrm{s}}$	estimated stator flux linkage
$\boldsymbol{\psi}_{\mathrm{s,ref}}$	stator flux linkage reference

Operators

$\|x\|$	absolute value of x
Δ	linearized quantity
e	Euler number
$\frac{\mathrm{d}}{\mathrm{d}t}$	derivative with respect to time t
$\int$	integral
s	Laplace operator
$\sin(), \cos()$	sine and cosine trigonometric functions
T	transpose

Abbreviations

A/Hz	amps-per-hertz
AC	alternating current
ADC	analog-to-digital converter
CT	continuous-time
DAC	digital-to-analog converter
DC	direct current
DT	discrete-time
HPF	high-pass filter
EMF	electromotive force
EMI	electromagnetic interference
GaN	gallium nitride
HF	high-frequency
HPF	high-pass filter
IEA	International Energy Agency
IGBT	Insulated-Gate Bipolar Transistor
IM	induction motor
IPM	interior permanent magnet synchronous motor
LC	inductor and capacitor
LCL	inductor, capacitor, and inductor
MOSFET	Metal Oxide Semiconductor Field Effect Transistor
MTPA	maximum torque per ampere
N	negative
PI	proportional-integral
PID	proportional-integral-derivative
PLL	phase-locked loop
PM	permanent magnet
PMSM	permanent-magnet synchronous motor
PM-SyRM	permanent-magnet synchronous reluctance motor
p.u.	per unit
PWM	pulse width modulation
rpm	revolutions per minute
SiC	silicon carbide
SM	synchronous motor
SPM	surface-mounted permanent magnet synchronous motor
SyRM	synchronous reluctance motor
V/Hz	volts-per-hertz
VSI	voltage source inverter
ZOH	zero-order hold

1 Introduction

1.1 Background and motivation

Over the last two decades, electric drives have become increasingly popular due to the growth in electrical energy consumption, leading to a significant rise in electric drive applications. A recent survey by the International Energy Agency (IEA 2017) shows that electric motor-driven systems consume more than half of the total produced electrical energy and more than 70% of the electrical energy in the industry [1]. Hence, the system efficiency is vital in reducing total costs and carbon emissions.

Most electric motors used for general purposes and in industrial processes consist of alternating current (AC) motors. AC motors can be divided into two types: induction motors (IMs) and synchronous motors (SMs). The IM is the most common motor type in the industry. In contrast, certain SM types have become the main competitors of IMs due to their high efficiency, such as permanent magnet synchronous motors (PMSMs), synchronous reluctance motors (SyRMs), and permanent-magnet synchronous reluctance motors (PM-SyRMs). IMs are superior to PMSMs in terms of their robust construction, price and simplicity of self-starting in direct connection with the mains. Nevertheless, the absence of rotor winding in SMs offers higher efficiency and energy savings [2], as well as a higher torque-per-ampere ratio and power density than IMs of the same size [3]. SMs are utilized in a whole range of power for applications, such as robot actuators, electric and hybrid vehicles, avionics, navy as well as industrial pumps, fans and paper mills.

The speed of a motor is typically controlled using frequency converters. Frequency converters convert supply voltage and frequency into a variable output voltage and frequency. One essential component in frequency converters is a power transistor, which is used as a switching device to convert DC (direct current) to AC. Most frequency converters are still equipped with conventional silicon switches due to their reliability and costs. Nevertheless, with the development of semiconductor technology, wide-bandgap converters with silicon carbide (SiC) or gallium nitride (GaN) switches outperform standard converters with silicon switches in many aspects, including higher switching frequency ratings, lower switching losses, higher efficiency, lower weight, improved quality of the current, and smaller carbon footprint [4]. Additionally, higher switching frequencies improve the quality of the converter output current, thereby reducing the noise and vibrations of the machine. On the other hand, the fast switching action that enables higher switching frequencies also introduces high $\mathrm{d}u/\mathrm{d}t$ differential-mode and common-mode voltage pulses.

The operation of the converter-fed electric motor can be impeded when using long lead cables between the converter and the motor. Long lead cables are typically used in industrial applications, such as air ventilation fans in the mining industry and submersible pumps in well applications at lengths up to 3 km [5]. Long leads therefore introduce an additional impedance to the system. When a high $\mathrm{d}u/\mathrm{d}t$ voltage pulse travels through a long cable for a time longer than the half rise time of the pulse, the reflected pulse combines with the incident pulse. As a result, motor terminals can experience voltage reflection and high-frequency ringing, thus amplifying the voltage

by 200-300% in the worst case [5]. Voltage stress strains the motor insulation, thus degrading the insulation properties and shortening the operating life. Moreover, the common-mode voltage pulses between the rotor shaft and the motor enclosure can yield to bearing currents, thus reducing the lifespan of the bearings.

One potential solution for mitigating the effects of voltage reflections and high-frequency ringing is to use an LC filter in the inverter output ("L" represents an inductor and "C" a capacitor). LC filters can be classified based on the resonance frequency of the filter into sinusoidal and $\mathrm{d}u/\mathrm{d}t$ LC filters. Although a $\mathrm{d}u/\mathrm{d}t$ filter can effectively suppress the short rise time of the voltage pulses, it can only be used for short cable lengths and cannot sufficiently filter the high-order harmonics. For example, $\mathrm{d}u/\mathrm{d}t$ filter in [6] uses switching frequencies lower than 4 kHz and cable lengths up to 300 m. High-order harmonics can be reduced using a sine wave LC filter, thus supplying the load with a sinusoidal voltage with a small residual ripple. This type of LC filter is also capable of suppressing the high $\mathrm{d}u/\mathrm{d}t$ of the voltage pulses. Additionally, a proper LC filter design can increase the motor efficiency and lifespan [7].

Various methods have been developed for controlling SMs, including vector control and volts-per-hertz (V/Hz) control. The vector control method is based on controlling the current space vector in an orthogonal frame that rotates synchronously with the rotor. V/Hz control maintains the flux linkage (and hence the ratio voltage per frequency) constant in a motor operation below and at rated speeds.

High-performance vector control can require speed or position sensors to make the control more robust against parameter errors but also mechanically more fragile than its sensorless modification. On the contrary, sensorless vector control is less susceptible to electromagnetic noise, more reliable, less complex, and less expensive than its sensored version [8]. However, the cascaded control loops and cumbersome controller parameters tuning for vector control demands a large computational complexity.

On the contrary, scalar control does not require complicated parameter settings and is handled by simpler control algorithms, which obviate the need for cascaded control loops. V/Hz control also allows multiple parallel-connected motors to be simultaneously controlled with a single converter [9]. On the other hand, fast acceleration action can cause the machine to pull out of synchronism because of an abrupt change in the load torque. In the case of vector control, the acceleration is limited by the torque limits. In other words, no rate limiters are needed for the speed reference in vector control, and the speed can be changed step-wise. V/Hz control is therefore suitable for moderate dynamic performance applications, such as pumps and fan drives.

Despite the advantages of V/Hz control, little work has focused on applying V/Hz control to SMs with LC filters. Sensorless control of SMs with LC filters becomes complicated due to the resonance frequency of the filter and the voltage drop over the filter inductor. Additionally, the control can be problematic if only either filter input or output current is measured due to the inaccurate estimation of the filter parameters. Recently, two methods have been applied for sensorless control with LC filters: vector control structures with speed estimation [10, 11] and A/Hz (amps-per-hertz) control [12, 13]. Existing A/Hz control structures using an LC

filter have only been implemented for startup procedures in specific applications, for example, PMSM drive for downhole electric drilling [13]. In addition, these control strategies have a limited operating range and require cumbersome parameter tuning, thus making them unsuitable for plug-and-play industrial applications, where the motor nameplate data or the user input are not required.

Recently, an observer-based V/Hz control method [14] has been proposed for SMs. Such an observer-based V/Hz control achieves a completely stable and passive system and could be utilized for any SM type. Furthermore, there is no need for a speed controller or additional field-weakening method; full available DC bus voltage can be utilized, and the parameter error sensitivity is reduced in comparison with sensorless vector control [14]. Hence, one of the key features of this control method is its plug-and-play ability. However, no work has yet attempted to integrate LC filters into this method.

1.2 Objectives

This thesis aims to develop observer-based V/Hz control strategies by adding LC filter dynamics to the observer-based V/Hz control method employed in [14]. The scope of the thesis is limited to PMSMs and SyRMs. Nevertheless, the augmented control strategies can apply to other SM types. To accomplish this task, the existing state-of-the-art control methods are first reviewed together with the other relevant literature. The observer-based V/Hz methods are then linearized by means of small-signal linearization to illustrate the root loci of dominating system poles. The linearization in the continuous-time domain is followed by developing the simulation model with a discrete-time controller. The purpose of the simulations is to unveil possible problems before executing the experiments. Finally, the measurements are taken from a prototype electric drive setup to validate the developed control methods.

1.3 Thesis structure

The thesis comprises six chapters. Chapter 2 describes the system model used in this thesis, the modeling approach, and basic theory concepts to analyze a three-phase SM drive with an LC filter. Chapter 3 reviews control methods for SMs with the LC filter, with an emphasis on sensorless control strategies. The chapter also develops the observer-based V/Hz control strategies with the LC filter. Chapter 4 presents small-signal linearized models of the developed control methods. Chapter 5 discusses the results obtained from the small-signal linearization, simulations, and experimental measurements. Finally, Chapter 6 concludes the thesis by discussing motor control performance and suggesting directions for future work.

2 System model

A basic structure of an electric drive system with an additional sinusoidal LC filter can be found in Figure 1. The electric drive system includes the frequency converter, the electric motor, and the mechanical load. However, the electric drive is defined as a system for electro-mechanical energy conversion, which incorporates transferring, processing, and generating control signals. Therefore, the electric drive consists of the frequency converter and the motor, and in some cases, it includes a filter and other auxiliary electrical equipment. The following sections describe the main parts of an SM drive with an LC filter.

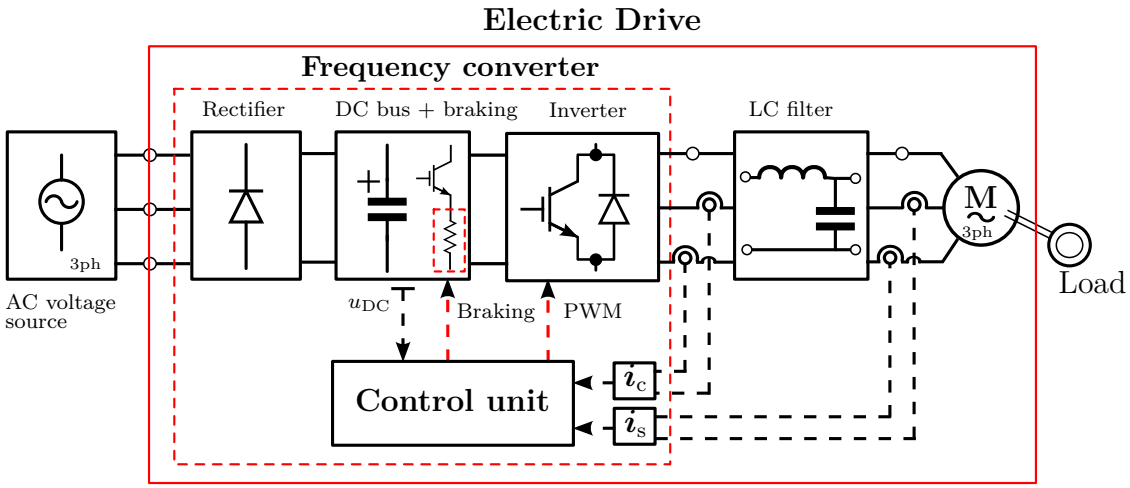

Figure 1: A structure of the electric drive system with an LC filter.

2.1 Synchronous motors

The objective of this chapter is to describe a continuous-time (CT) dynamic model of the SM. First, SMs are classified based on their construction. Secondly, the basic concepts of space vectors and coordinate transformations are presented to build the SM model. Finally, the dynamic model of the SM is expressed in rotor and control coordinates at the end of this chapter.

2.1.1 Classification and basic construction

The construction of the SM is comprised of a static part (stator) and a rotating part (rotor) separated by an air gap. A phase winding is inserted into the slots located in the inner periphery of the stator to create sinusoidal distribution of magnetic flux in space.

SM variants can be classified according to different rotor structures. Depending on the presence of an excitation winding in the rotor, SMs can be broadly divided into excited and non-excited motors. The excited rotor of the motor requires external

DC (direct current) supply to create magnetic flux linkage in the rotor. Non-excited rotor of the SM relies on permanent magnet flux linkage or on the saliency of poles.

Non-salient synchronous machines have a constant mutual inductance between the stator and the rotor along the whole rotor periphery [15]. The ratio between stator inductance components in rotor coordinates (L_q and L_d) is therefore close to one. Conversely, the inductance components (L_q and L_d) vary from each other in salient synchronous motors.

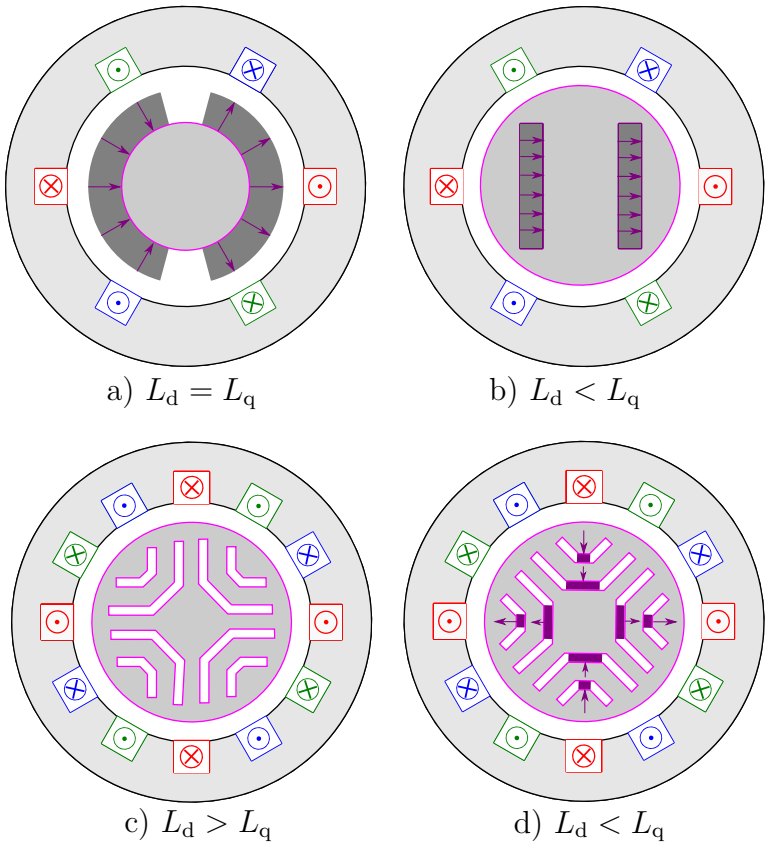

Figure 2: Cross-section selection of synchronous machine types: (a) 2-pole SPM, (b) 2-pole salient IPM, (c) 4-pole SyRM, (d) 4-pole PM-SyRM. Each phase of stator winding is marked with different color. The orientation of the PM flux is marked with the violet arrow. The orientation of the current marked with the "cross" or "dot" means that the current flows inside or outside the screen, respectively. One end of the winding is connected to the voltage source, the other end is connected to the other phases ends, thus creating a neutral point.

Based on the shape and location of PMs, PMSMs can be divided into surface-mounted permanent magnet motors (SPMs - Figure 2(a)), interior permanent magnet motors (IPMs: non-salient pole and salient pole Figure 2(b)). The rotor of the IPM is from the mechanical design point of view similar to the SPM with the difference of permanent magnets buried inside the rotor. Another SM type is the SyRM (Figure 2(c)), which does not have PMs nor excitation winding. A PM-assisted SyRM (PMSM-SyRM) is shown in the Figure 2(d).

2.1.2 Space vectors

Real space vectors are used throughout the thesis. The vectors are denoted with lowercase boldface letters and matrices with uppercase boldface letters. Furthermore, it is worth defining some of the common matrices when calculating with real space vectors, such as the identity matrix $\mathbf{I} = \left[\begin{smallmatrix} 1 & 0 \\ 0 & 1 \end{smallmatrix}\right]$, the orthogonal rotation matrix $\mathbf{J} = \left[\begin{smallmatrix} 0 & -1 \\ 1 & 0 \end{smallmatrix}\right]$ and the zero matrix $\mathbf{0} = \left[\begin{smallmatrix} 0 & 0 \\ 0 & 0 \end{smallmatrix}\right]$.

A space vector describes the instantaneous magnitude and angle of the sinusoidal distribution in the space. Space vector representation is commonly used in analysis, modelling and control of three-phase systems.

Three-phase winding of the stator can be linked with an orthogonal axis $\alpha\beta$ plane and the three-phase stator currents can be transformed into the real space vector. The main benefit of this transformation is to simplify the three-phase system by a two-element space vector. The transformation of phase quantities to the space vector is called $\alpha\beta$ transformation, which is defined as

$$\boldsymbol{i}_\mathrm{s}^\mathrm{s} = \begin{bmatrix} i_\alpha \\ i_\beta \end{bmatrix} = \frac{2}{3} \begin{bmatrix} 1 & -\frac{1}{2} & -\frac{1}{2} \\ 0 & \frac{\sqrt{3}}{2} & -\frac{\sqrt{3}}{2} \end{bmatrix} \begin{bmatrix} i_\mathrm{a} \\ i_\mathrm{b} \\ i_\mathrm{c} \end{bmatrix} \tag{1}$$

where superscript s denotes the stator coordinates, the subscript s refers to the stator quantities, subscripts a, b and c mark the phases, and subscripts α and β mark the real-valued vector components in stator coordinates. Other space vector quantities, such as stator voltage and flux linkage, are defined in similar manner.

The stator winding is in a delta connection or in a star connection without a neutral conductor. Therefore, the zero-sequence stator current cannot flow. Hence, the sum of the three phase currents at each time instant is zero. Consequently, one phase current can be expressed by the other two phases without any loss of information.

The inverse $\alpha\beta$ transformation is used in order to obtain phase quantities from a magnitude and phase. It is defined as

$$\begin{bmatrix} i_\mathrm{a} \\ i_\mathrm{b} \\ i_\mathrm{c} \end{bmatrix} = \begin{bmatrix} 1 & 0 \\ -\frac{1}{2} & \frac{\sqrt{3}}{2} \\ -\frac{1}{2} & -\frac{\sqrt{3}}{2} \end{bmatrix} \begin{bmatrix} i_\alpha \\ i_\beta \end{bmatrix} \tag{2}$$

2.1.3 Direct-quadrature transformation

Direct-quadrature (dq) transformation transforms a rotating space vector in a stationary coordinate system to a stationary space vector with a rotating orthogonal plane. Therefore, harmonically varying quantities in stator coordinates become DC quantities in rotor coordinates. Direct-quadrature real-valued space vector is defined as

$$\boldsymbol{i}_\mathrm{s} = \begin{bmatrix} i_\mathrm{d} \\ i_\mathrm{q} \end{bmatrix} = \mathrm{e}^{-\mathbf{J}\vartheta_\mathrm{m}} \boldsymbol{i}_\mathrm{s}^\mathrm{s} = \begin{bmatrix} \cos\vartheta_\mathrm{m} & \sin\vartheta_\mathrm{m} \\ -\sin\vartheta_\mathrm{m} & \cos\vartheta_\mathrm{m} \end{bmatrix} \begin{bmatrix} i_\alpha \\ i_\beta \end{bmatrix} \tag{3}$$

where missing superscript denotes the vector in dq coordinates and ϑ_m is the electrical angle of the rotor, equivalently interpreted as the angle of the rotating dq frame. The

components of space vector in dq coordinates are constant in the steady-state. The electrical angle of the rotor ϑ_m can be obtained as

$$\vartheta_\mathrm{m} = \int \omega_\mathrm{m} \, \mathrm{d}t \tag{4}$$

where ω_m is an angular speed of the rotating dq frame (electromagnetic speed of the rotor). The d-axis of the coordinate system can be aligned with the direction of the rotor magnetic field. Examples of the orthogonal axis alignment and coordinate transformations are shown at two pole surface-mounted PMSM in the Figure 3.

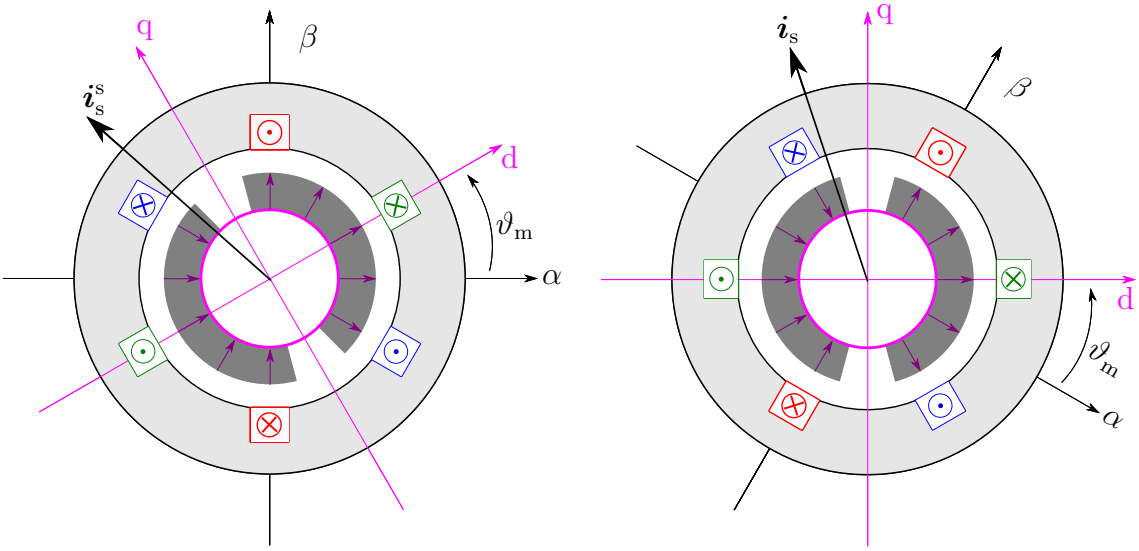

Stator coordinates ($\alpha\beta$) Rotor coordinates (dq)

Figure 3: Coordinate transformations.

2.1.4 Dynamic model in rotor coordinates

Block diagram in Figure 5 illustrates the SM model in rotor coordinates together with a mechanical subsystem. The stator voltage $\boldsymbol{u}_\mathrm{s}$ of the synchronous motor in rotor coordinates is

$$\boldsymbol{u}_\mathrm{s} = \begin{bmatrix} u_\mathrm{d} \\ u_\mathrm{q} \end{bmatrix} = R_\mathrm{s}\boldsymbol{i}_\mathrm{s} + \frac{\mathrm{d}\boldsymbol{\psi}_\mathrm{s}}{\mathrm{d}t} + \omega_\mathrm{m}\mathbf{J}\boldsymbol{\psi}_\mathrm{s} \tag{5}$$

where R_s denotes the stator resistance and $\boldsymbol{\psi}_\mathrm{s}$ is the stator flux linkage in rotor coordinates. Furthermore, a magnetic model can be derived from the stator flux linkage $\boldsymbol{\psi}_\mathrm{s}$, which is expressed as

$$\boldsymbol{\psi}_\mathrm{s} = \begin{bmatrix} \psi_\mathrm{d} \\ \psi_\mathrm{q} \end{bmatrix} = \boldsymbol{L}_\mathrm{s}\boldsymbol{i}_\mathrm{s} + \begin{bmatrix} \psi_\mathrm{f} \\ 0 \end{bmatrix} = \begin{bmatrix} L_\mathrm{d} & 0 \\ 0 & L_\mathrm{q} \end{bmatrix} \begin{bmatrix} i_\mathrm{d} \\ i_\mathrm{q} \end{bmatrix} + \begin{bmatrix} \psi_\mathrm{f} \\ 0 \end{bmatrix} \tag{6}$$

where $\boldsymbol{L}_\mathrm{s}$ is the stator inductance matrix in rotor coordinates. The PM flux linkage ψ_f is constant for PMSMs. Conversely, SyRMs do not include permanent magnets,

neither excitation winding, which leads to a zero PM flux linkage ($\psi_\mathrm{f} = 0$). The parallel branch of the current source in Figure 4 can be therefore omitted for SyRM.

Based on the above-mentioned expressions, an equivalent electrical circuit is constructed (Figure 4). The figure shows a decomposition of the voltage model (5) in dq components, which supports a visual understanding on how the stator voltage components depend on other quantities.

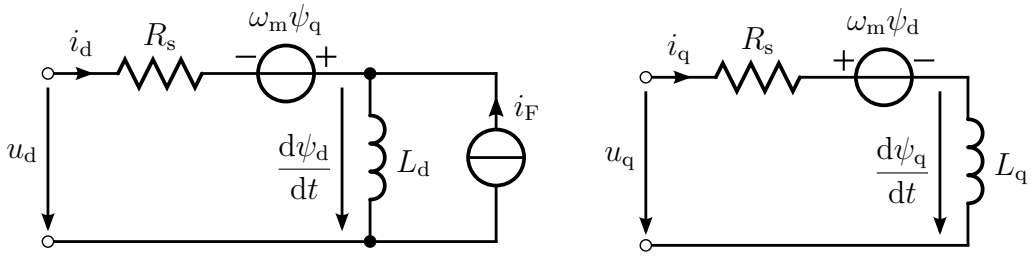

Figure 4: Equivalent electrical circuits of the SM in rotor coordinates. The PM flux linkage is $\psi_\mathrm{f} = L_\mathrm{d} i_\mathrm{F}$.

An electromagnetic torque τ_m of a rotating AC machine can be expressed as

$$\tau_\mathrm{m} = \frac{3p}{2} \boldsymbol{i}_\mathrm{s}^\mathrm{T} \mathbf{J} \boldsymbol{\psi}_\mathrm{s} \tag{7}$$

where p denotes the number of pole pairs. Mechanical dynamics of the motor are governed by

$$\frac{J_\mathrm{m}}{p} \frac{\mathrm{d}\omega_\mathrm{m}}{\mathrm{d}t} = \tau_\mathrm{m} - \tau_\mathrm{L} \tag{8}$$

where $\omega_\mathrm{m} = p\omega_\mathrm{M}$. Mechanical angular speed is denoted as ω_M and number of pole pairs is p. Furthermore, J_m is a total moment of inertia and τ_L is a load torque. For simplicity, the viscous damping is neglected.

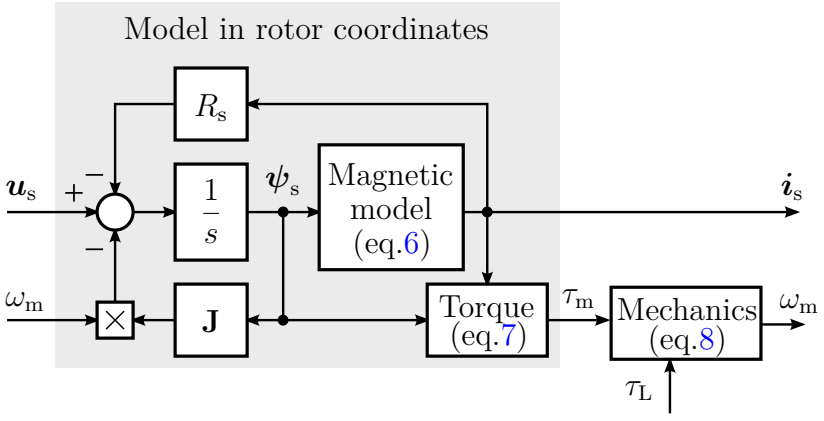

Figure 5: The SM model in rotor coordinates with a mechanical subsystem.

2.1.5 Dynamic model in control coordinates

For the purpose of defining control coordinates system, let us use the electrical angle of the rotor ϑ_m and the angle of the coordinate system ϑ_c, which are fixed with respect to stator coordinates. The angle difference $\delta = \vartheta_\mathrm{c} - \vartheta_\mathrm{m}$ represents the angle of the control coordinate system with respect to the d-axis of the rotor [14]. The angle δ can be named as a load angle, if the coordinate system were fixed to the stator flux [14]. However, in the case of using the LC filter, the coordinate system is fixed to the converter flux linkage $\boldsymbol{\psi}_\mathrm{c}$.

The control coordinates are used throughout the thesis. For simplicity, the notation for space vectors in control coordinates remains the same as for space vectors in rotor coordinates. The following equations in control coordinates (xy) are obtained by coordinate transformation from the equations (5) and (6) in rotor coordinates. Therefore, SM state equations are

$$\frac{\mathrm{d}\boldsymbol{\psi}_\mathrm{s}}{\mathrm{d}t} = \boldsymbol{u}_\mathrm{s} - R_\mathrm{s}\boldsymbol{i}_\mathrm{s} - \omega_\mathrm{c}\mathbf{J}\boldsymbol{\psi}_\mathrm{s} \tag{9a}$$

$$\frac{\mathrm{d}\delta}{\mathrm{d}t} = \omega_\mathrm{c} - \omega_\mathrm{m} \tag{9b}$$

where ω_c is a synchronous speed of the rotating coordinate system, $\boldsymbol{u}_\mathrm{s} = [u_\mathrm{sx}, u_\mathrm{sy}]^\mathrm{T}$ and $\boldsymbol{\psi}_\mathrm{s} = [\psi_\mathrm{sx}, \psi_\mathrm{sy}]^\mathrm{T}$. Furthermore, the stator inductance $\boldsymbol{L}_\mathrm{s}(\delta)$ and PM flux linkage $\boldsymbol{\psi}_\mathrm{F}(\delta)$ in control coordinates are

$$\boldsymbol{L}_\mathrm{s}(\delta) = \mathrm{e}^{-\delta\mathbf{J}} \begin{bmatrix} L_\mathrm{d} & 0 \\ 0 & L_\mathrm{q} \end{bmatrix} \mathrm{e}^{\delta\mathbf{J}} \qquad \boldsymbol{\psi}_\mathrm{F}(\delta) = \mathrm{e}^{-\delta\mathbf{J}} \begin{bmatrix} \psi_\mathrm{f} \\ 0 \end{bmatrix} \tag{10}$$

Finally, stator current $\boldsymbol{i}_\mathrm{s}$ in control coordinates can be expressed as

$$\boldsymbol{i}_\mathrm{s} = \boldsymbol{L}_\mathrm{s}^{-1}(\delta)\left[\boldsymbol{\psi}_\mathrm{s} - \boldsymbol{\psi}_\mathrm{F}(\delta)\right] \tag{11}$$

Figure 6 shows vector diagrams of the PMSM and SyRM with LC filters for two different operating conditions. Control coordinates are used, as well as rotor coordinates to show the relation between xy and dq orthogonal axes. The motor and filter parameters are taken from Appendix A.

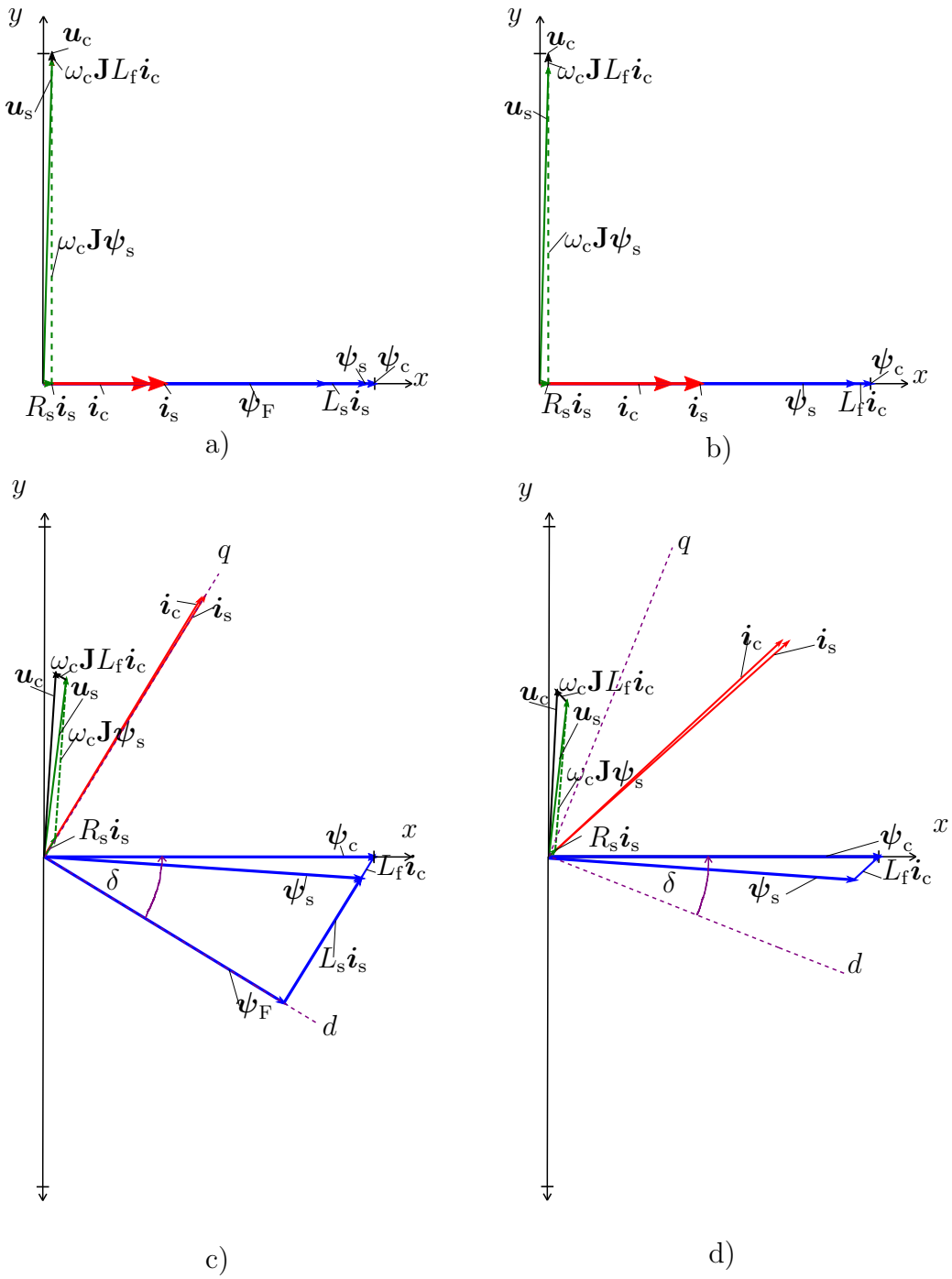

Figure 6: Vector diagrams of SMs with LC filters: (a) PMSM ($\omega_\mathrm{c} = 1$ p.u., $\tau_\mathrm{L} = 0$), (b) SyRM ($\omega_\mathrm{c} = 1$ p.u., $\tau_\mathrm{L} = 0$), (c) PMSM ($\omega_\mathrm{c} = 0.5$ p.u., $\tau_\mathrm{L} = 1$ p.u.), (d) SyRM ($\omega_\mathrm{c} = 0.5$ p.u., $\tau_\mathrm{L} = 1$ p.u.).

2.2 Inverter and Pulse Width Modulation

2.2.1 Basic structure of the VSI

The electrical energy is converted by the frequency converter stepwise: A rectifier converts an input AC voltage to a DC voltage and an inverter converts the DC voltage to a variable output voltage and frequency (Figure 1). The most common type of the inverter used in the electric drives is a voltage source inverter (VSI). The VSI is a power electronic device which is supplied by a stiff DC bus voltage. The constant voltage is realized by using a capacitor bank in the DC bus. The output current of the VSI depends on the impedance of the load.

Figure 7 shows a basic structure of a three-phase VSI. The VSI consists of three legs, which are divided into upper and lower branches. Each branch includes a power switch and a freewheeling diode in anti-parallel connection. Depending on the application, IGBTs or MOSFETs are used as power switches. The purpose of the freewheeling diode is to provide a current path when the switch is turned off and when the current needs to flow in the opposite direction.

Only one transistor in each leg is turned on and the other one is turned off. Simultaneous "ON" action causes a short circuit of the DC bus, which can damage the inverter. Real switches have non-zero turn on and turn off times. A dead-time is therefore implemented to prevent a short circuit caused by transient states of the real switch.

The output line voltages of the VSI contain bidirectional voltage pulses with the same magnitude but variable pulse widths. The connected AC motor then utilizes the fundamental harmonic of the incoming voltage signal to create a rotating magnetic field. The rest of the n^{th}-order harmonics are undesirable for the motor, causing noise, heat, and overvoltages on the motor terminals.

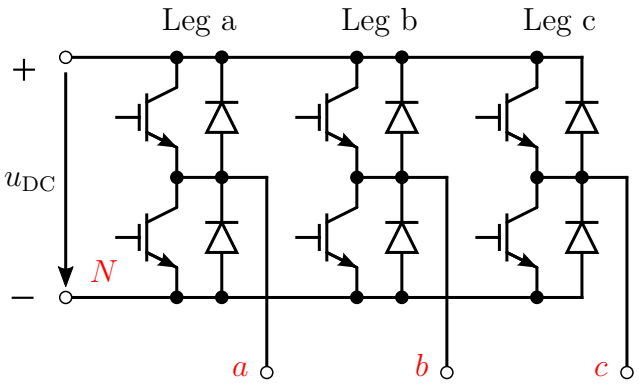

Figure 7: A basic concept of a three-phase two-level VSI circuit.

2.2.2 Switching state space vectors

Similarly as $\boldsymbol{i}_{\mathrm{s}}^{\mathrm{s}}$ in Section 2.1.2, converter output voltage vector $\boldsymbol{u}_{\mathrm{c}}^{\mathrm{s}}$ in stator coordinates is defined as

$$\boldsymbol{u}_{\mathrm{c}}^{\mathrm{s}} = \frac{2}{3}\begin{bmatrix} 1 & -\frac{1}{2} & -\frac{1}{2} \\ 0 & \frac{\sqrt{3}}{2} & -\frac{\sqrt{3}}{2} \end{bmatrix} \begin{bmatrix} u_{\mathrm{aN}} \\ u_{\mathrm{bN}} \\ u_{\mathrm{cN}} \end{bmatrix} = \frac{2}{3} u_{\mathrm{DC}} \begin{bmatrix} 1 & -\frac{1}{2} & -\frac{1}{2} \\ 0 & \frac{\sqrt{3}}{2} & -\frac{\sqrt{3}}{2} \end{bmatrix} \underbrace{\begin{bmatrix} q_{\mathrm{a}} \\ q_{\mathrm{b}} \\ q_{\mathrm{c}} \end{bmatrix}}_{\boldsymbol{q}_{\mathrm{abc}}} \tag{12}$$

where subscript N refers to negative DC bus reference. Alternatively, neutral point of star-connected stator winding can be chosen. Furthermore, u_{DC} refers to DC bus voltage and switching state vector is denoted as $\boldsymbol{q}_{\mathrm{abc}}$. An averaged inverter output voltage over the switching period can be then expressed by substituting $\boldsymbol{q}_{\mathrm{abc}}$ in (12) for duty ratios vector $\boldsymbol{d}_{\mathrm{abc}}$, whose values vary between 0...1.

Switching space vector elements $q_{\mathrm{a}}, q_{\mathrm{b}}$ and q_{c} can be either logical "1" or "0". Logical "1" is used to turn on the upper transistor in the inverter leg and logical "0" turns on the lower transistor of the given leg. Therefore, eight possible combinations exist, which can be substituted to (12).

Based on the switching state combination logic, eight switching state vectors in the complex plane can be found for the three-phase two-level VSI: six active and two zero switching state vectors (Figure 8). The voltage vector has a zero magnitude when all upper or all lower switches are closed. Zero state vectors are used when designing pulse width modulated (PWM) control strategies [16].

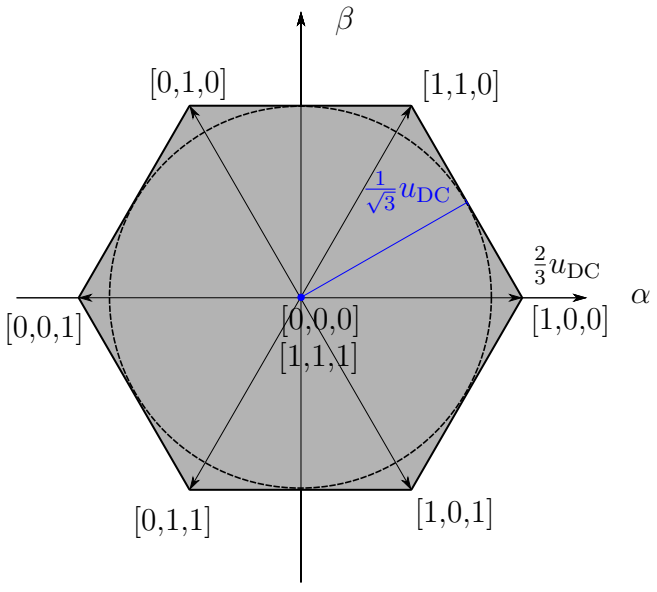

Figure 8: Voltage hexagon of two-level three-phase VSI in stator coordinates.

2.2.3 Pulse width modulator

The transistors in the VSI are controlled by voltage pulses obtained from a pulse width modulator, which is a part of the control unit (Figure 1). Figure 9 shows a model of the pulse width modulator. A modulating signal (voltage reference) is compared with the high-frequency (HF) carrier from the counter of a digital signal processor to obtain PWM output signals. A comparator output provides logical "1" if the modulating signal is higher than the carrier, otherwise the output is logical "0".

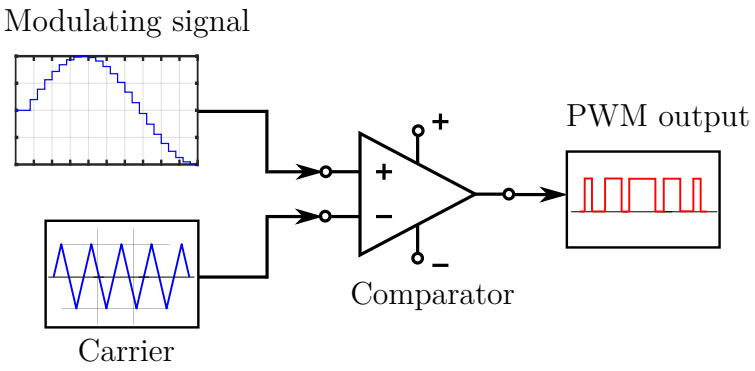

Figure 9: A basic model of the pulse width modulator.

A basic sinusoidal PWM utilizes roughly 87% of the maximum available voltage, which is $\frac{1}{\sqrt{3}}u_{\mathrm{DC}}$. This area in Figure 8 is limited with the dashed circle which represents the boundary of the linear modulation. Conversely, a space vector PWM is typically used in industrial drives to utilize full available voltage ($\frac{2}{3}u_{\mathrm{DC}}$) and hence the whole hexagon area. The modulation signal is not pure sinusoidal, but it follows a pattern similar to Figure 10.

A single-update space vector PWM is depicted in Figure 10. Duty ratios $d_{\mathrm{a}}, d_{\mathrm{b}}$ and d_{c} are updated once per the sampling period at the instant when the counter reaches the maximum. Therefore, the switching frequency is equal to the sampling frequency. The information about the phase currents are similarly taken at the same instant. Because of the synchronous sampling, no switching ripple is present in the phase currents measurements. An isosceles triangular carrier places the PWM pulses symmetrically between two consecutive PWM updates in the case of the single-update PWM. The advantage of using the isosceles triangular carrier in comparison with a saw-tooth carrier consists in eliminating even carrier harmonics as well as even side-band harmonics [17].

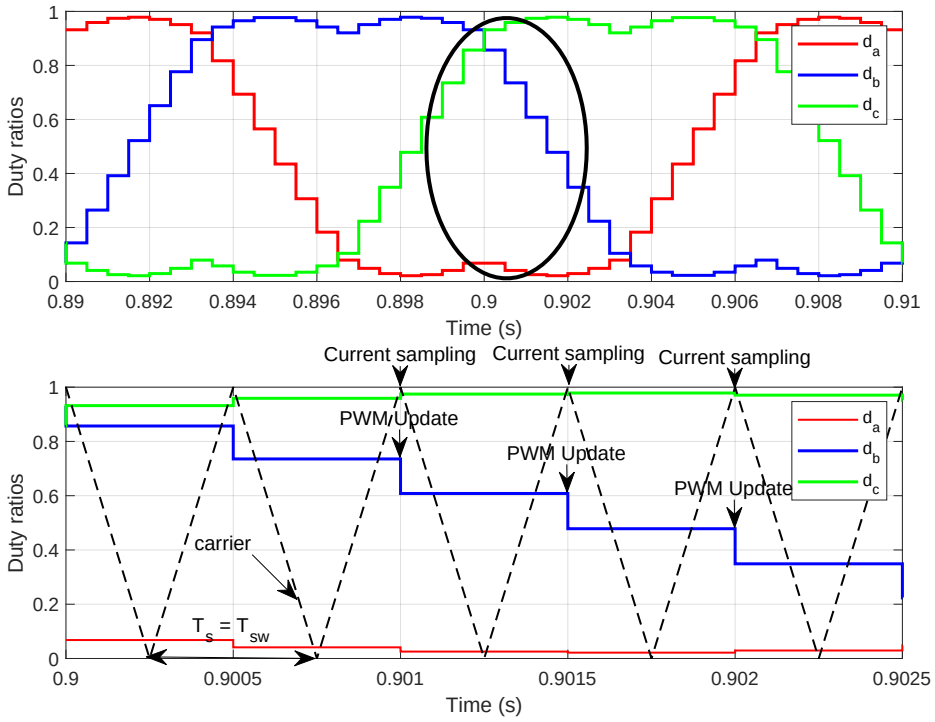

Figure 10: A carrier comparison with the single-update PWM. The sampling period T_s is equal to the switching period T_sw.

2.2.4 DT control system and DT delays

Figure 11 shows a basic structure of a digital control system. A DT controller receives input signals, processes the received data and sends output control signal to the inverter. The input signals can be references given by a user or plant model output feedback, which are predominantly continuous in nature. Therefore, the signals need to be sampled (typically voltage) and converted to a digital number via analog-to-digital converter (ADC).

The role of the inverter model is to convert digital signal to analog signal, which is sent to the plant model (SM with LC filter). The conversion from a digital number back to the analog voltage is performed by a digital-to-analog converter (DAC) and zero-order-hold (ZOH). ZOH keeps the same voltage during the whole T_s.

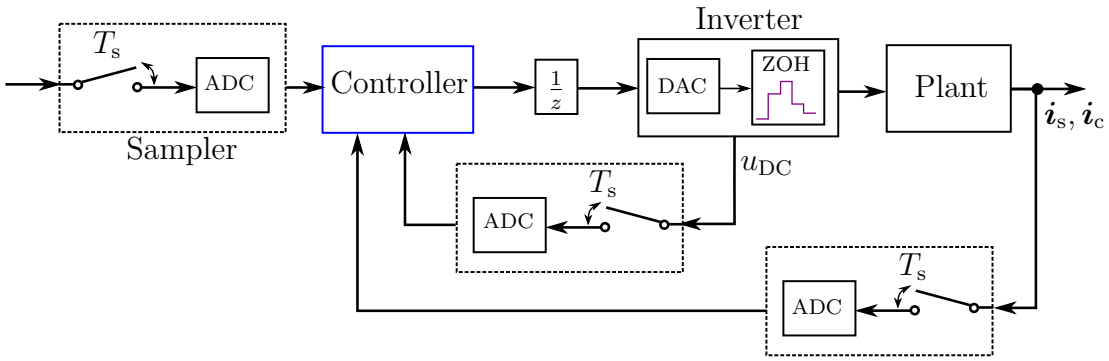

Figure 11: A simplified block diagram of a digital control system.

DT delays are always present when digital signal processors are used. The delay is caused by a controller computational time delay ($\frac{1}{z}$ block in Figure 11) and PWM delay [15]. The controller delay originates from the sampling circuitry, because the processor cannot manipulate with immediate sampled information, but only with previously sampled information. The PWM delay of $0.5T_s$ is obtained by reconstruction of the DT signal from the ZOH into the CT signal [18]. The minimal total time delay in the single-update PWM is therefore $1.5T_s$ [19]. Figure 12 visually demonstrates aforementioned digital delays.

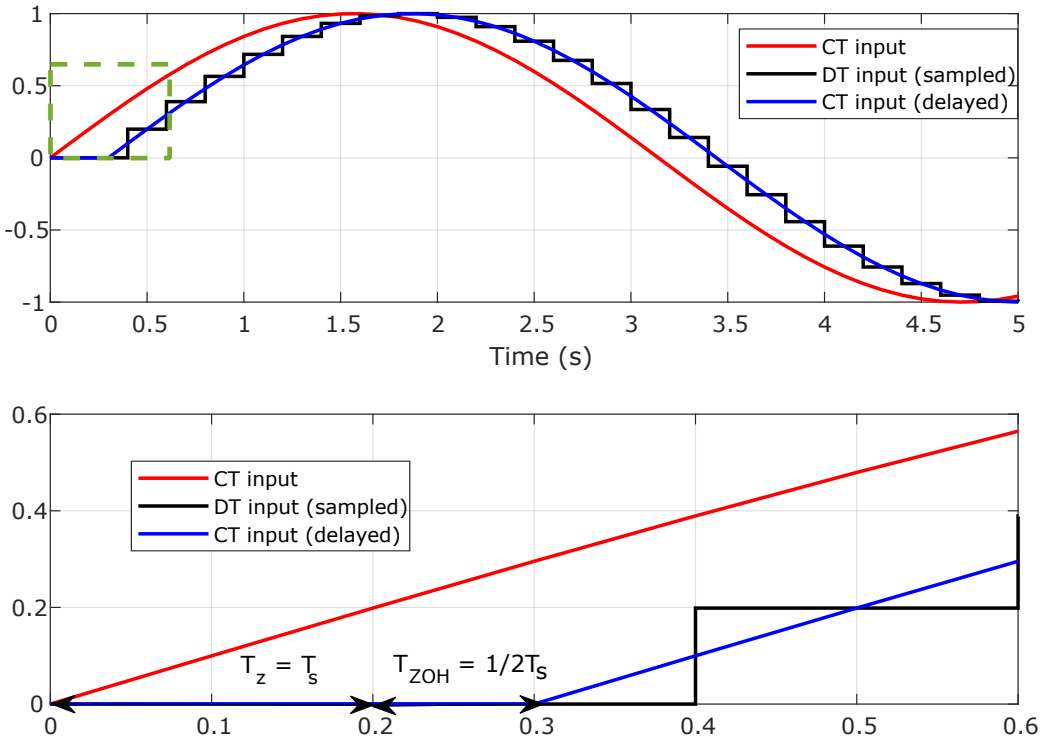

Figure 12: DT delays: the CT input signal (red line) is delayed by $1.5T_s$ (blue line) because of DT delays.

2.3 LC filter

Sine-wave LC filters are used throughout the thesis, therefore the terminology "LC filter" is strictly related to this type of the filter. Figure 13 shows a circuit diagram of an LC filter. The LC filter consists of passive components, such as inductors, capacitors and resistors. The role of clamping resistors (connected in parallel with capacitors) is to reduce the $\mathrm{d}u/\mathrm{d}t$ without using the $\mathrm{d}u/\mathrm{d}t$ filter.

The resonance frequency of the sine-wave LC filter is below the switching frequency to supply the motor with nearly sinusoidal voltage. The filtered line-to-line voltages are shown in Figure 14 for the selected PMSM and SyRM at nominal speed. The resonance frequency of the filter f_r is defined as

$$f_\mathrm{r} = \frac{1}{2\pi}\sqrt{\frac{1}{L_\mathrm{f} C_\mathrm{f}}} \tag{13}$$

where L_f is a filter inductance and C_f is a filter capacitance.

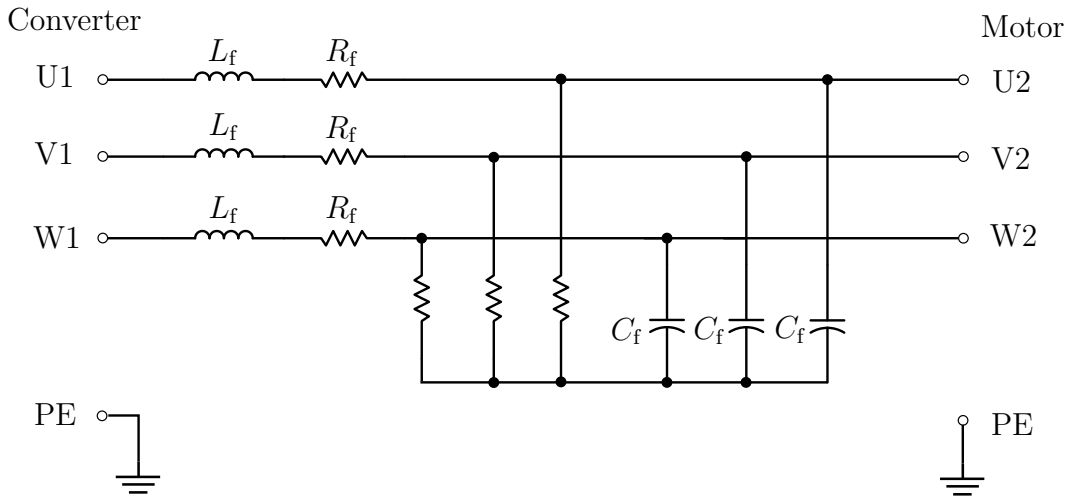

Figure 13: Circuit diagram of selected LC filters.

A frequency response for selected LC filters is illustrated in Figure 15 to examine the behaviour of an LC-filter over a wide range of frequencies. Hence, an open-circuit voltage transfer function of LC filter is expressed as

$$G(s) = \frac{\boldsymbol{u}_\mathrm{s}(s)}{\boldsymbol{u}_\mathrm{c}(s)} = \frac{1}{s^2 L_\mathrm{f} C_\mathrm{f} + s R_\mathrm{f} C_\mathrm{f} + 1} \tag{14}$$

where $\boldsymbol{u}_\mathrm{c}$ is converter voltage space vector.

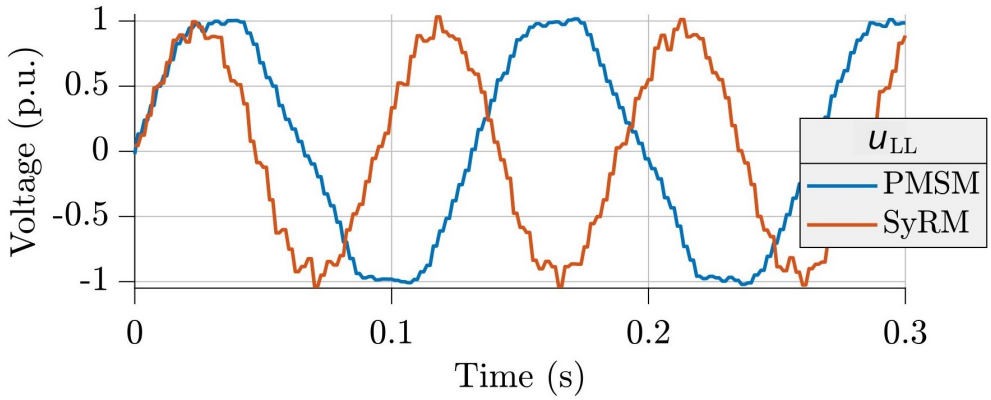

Figure 14: Measurement of the filtered line-to-line voltage (u_{LL}).

It is worth noticing that the filter resistance R_{f} does not influence the output voltage magnitude neither phase, only in the resonance frequency point. The resistance R_{f} can be therefore neglected for simplicity by assuming the worst-case scenario in the control model. However, it is later shown that this simplification cannot be performed in the measurements.

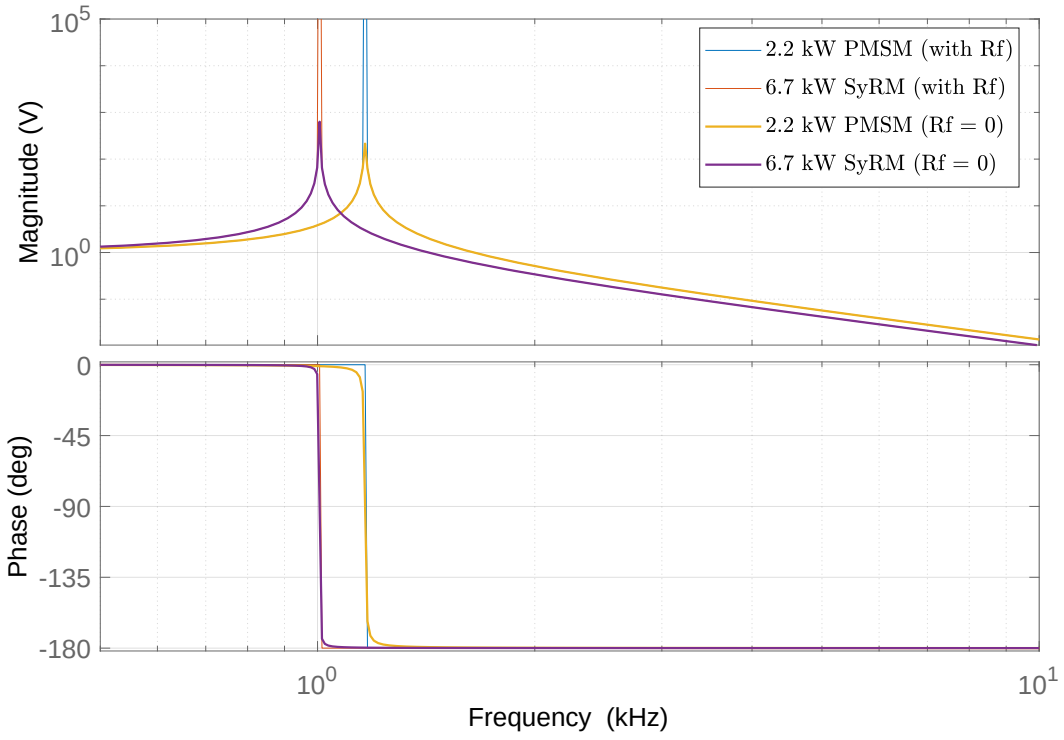

Figure 15: Frequency response of $G(s)$ for LC filters in Appendix A.

LC filter dynamic model

LC filter dynamic model consists of the states for stator voltage dynamics $\boldsymbol{u}_\mathrm{s}$ and converter current $\boldsymbol{i}_\mathrm{c}$ dynamics

$$L_\mathrm{f}\frac{\mathrm{d}\boldsymbol{i}_\mathrm{c}}{\mathrm{d}t} = \boldsymbol{u}_\mathrm{c} - \boldsymbol{u}_\mathrm{s} - \omega_\mathrm{c} L_\mathrm{f}\mathbf{J}\boldsymbol{i}_\mathrm{c} \tag{15a}$$

$$C_\mathrm{f}\frac{\mathrm{d}\boldsymbol{u}_\mathrm{s}}{\mathrm{d}t} = \boldsymbol{i}_\mathrm{c} - \boldsymbol{i}_\mathrm{s} - \omega_\mathrm{c} C_\mathrm{f}\mathbf{J}\boldsymbol{u}_\mathrm{s} \tag{15b}$$

Considering filter dynamics in SM drives, converter flux linkage $\boldsymbol{\psi}_\mathrm{c}$ can be defined as

$$\boldsymbol{\psi}_\mathrm{c} = L_\mathrm{f}\boldsymbol{i}_\mathrm{c} + \boldsymbol{\psi}_\mathrm{s} \tag{16}$$

Therefore, existing state equation for stator flux dynamics of the SM model (9) can be replaced by the state equation for converter flux linkage dynamics

$$\frac{\mathrm{d}\boldsymbol{\psi}_\mathrm{c}}{\mathrm{d}t} = \boldsymbol{u}_\mathrm{c} - R_\mathrm{s}\boldsymbol{i}_\mathrm{s} - \omega_\mathrm{c}\mathbf{J}\boldsymbol{\psi}_\mathrm{c} \tag{17}$$

3 Control model

This chapter is organized as follows. Section 3.1 introduces the recent development state in controlling SMs. Proposed observer-based V/Hz control methods are described in 3.2.

3.1 State-of-the-art of sensorless SM control

3.1.1 Sensorless vector control

Although sensorless vector control is not developed in this thesis, the control has been researched in the context of the observers because the observers can also be adapted to the V/Hz control. The following section provides background information about different sensorless vector control methods to show the observer benefits and vector control shortages in relation to medium-performance plug-and-play drives.

Rotor-position estimation

Sensorless vector control is based on the estimation of the rotor position. Rotor-position estimation methods can be divided into two groups [20]: fundamental-excitation-based and high-frequency signal injection methods. The excitation-based method is based on the back-electromotive force (EMF) technique, which originates from the voltage model of the SM (5). The operation at low speeds is unstable with the fundamental excitation-based methods [21] because of low back-EMF and measurement noises. Consequently, the excitation-based methods are further augmented with an HF signal-injection loop to provide a stable operation at low speeds [22]. However, the HF signal injection causes additional losses and noise, as well as poor dynamic performance [20].

Subsequently, a sensorless control strategy for PMSM with LC filter was introduced based on rotor position and velocity estimation [10]. Stator currents and voltages are measured to estimate the states. A low-pass filter was used in addition to the line filter to eliminate HF harmonics from the stator voltage measurement. The experimental results in [10] indicate that the drive is robust against load disturbances and uncertain motor parameters. Although the rotor angle estimation is accurate, the magnitude of the average error can increase proportionally to the rotor speed because of the low-pass filter delay. Additionally, the operation at low speeds is not recommended due to occasional velocity polarity errors. The absence of the speed sensor causes a challenge in speed tracking; therefore, the velocity controller should be improved.

Speed-adaptive full-order observer

The state estimation in modern drives is performed by a state observer. A speed-adaptive observer performs simultaneous estimation of the state variables ($\hat{\boldsymbol{\psi}}_\mathrm{s}$), and the unknown parameter ($\hat{\omega}_\mathrm{m}$) [23]. Speed-adaptive observer improves the motor performance by augmenting the state equation of voltage motor model (5) with

compensation of the stator current error [20]. The selection of observer gains allows placing the poles in desired locations, thus having more stable and less sensitive control. PI controller minimizes the stator current error, which is used for speed estimation. However, the interaction between the observer and the speed estimation may lead to unstable regions [24]. Therefore, the selection of the observer gains, which allows decoupling and enables pole placement, should be carefully chosen.

A full-order speed-adaptive observer for the PMSM drive with the LC filter is described in [11], which is augmented from a method without the filter [25]. Figure 16 shows a block diagram of sensorless vector control based on the speed-adaptive full-order observer for SMs with LC filters. The control is extended with an HF signal injection method (marked with red color). It can be noticed that the converter voltage vector is obtained from the output of the current controller, meaning that only the converter currents are measured. The integration of LC filters in electric drives without external current sensors is desired for medium-performance motor control. The adaptive observer in [11] includes a flux model (6) giving the reference model and a voltage model (5) as the adaptive model. According to [26], a linear mathematical derivation of the machine and the LC filter is used in [11] with nearly constant inductances. However, the inductances in other SMs can be non-linear. For example, the non-linear inductances are obtained from lookup tables [26]. Nevertheless, the method in [11] is claimed to have a satisfactory stability, solid robustness, and a good dynamic response. Additionally, a field weakening method enables maximum-torque operation. Furthermore, the maximum torque can be even higher with the LC filter than without it. The main issue of this method is a relatively small controller bandwidth of the stator current controller [11].

Literature source [27] names the speed-adaptive full-order observer as a dual observer, which estimates the filter output current (current observer) and output voltage (voltage observer). The dual observer is more robust against parameter errors than a conventional model-based estimation method because it neglects LC filter cross-coupling effects [27]. Furthermore, a capacitor parameter error does not significantly impact the observer estimation. However, the filter inductance error at high speeds affects the capacitor current estimation, causing a noticeable phase and magnitude difference between the stator and converter current [27].

Sliding-mode control with PI observer

Sliding-mode control based on PI (proportional-integral) observer in $\alpha\beta$ frame is described in [28] for the SPM with the LC filter. The sliding-mode observer observes back electromotive force, and the rotor angle is obtained by a phase-locked loop (PLL). However, the PLL can cause speed reversal issues, instability, and speed estimation errors [29]. Moreover, an additional PI controller needs to be employed to eliminate the estimation error [30]. The estimation error at lower speeds is affected by inverter non-linearities and back EMF harmonics [31]. Nevertheless, this control method is suitable for operation at medium and high speeds. It benefits from its simplicity, good dynamic performance, robustness against parameter errors, and ease of implementation according to [28]. Furthermore, the method is claimed to be

suitable for operation at medium and high speeds. However, overall, there are no convincing results for good parameter sensitivity in this type of control.

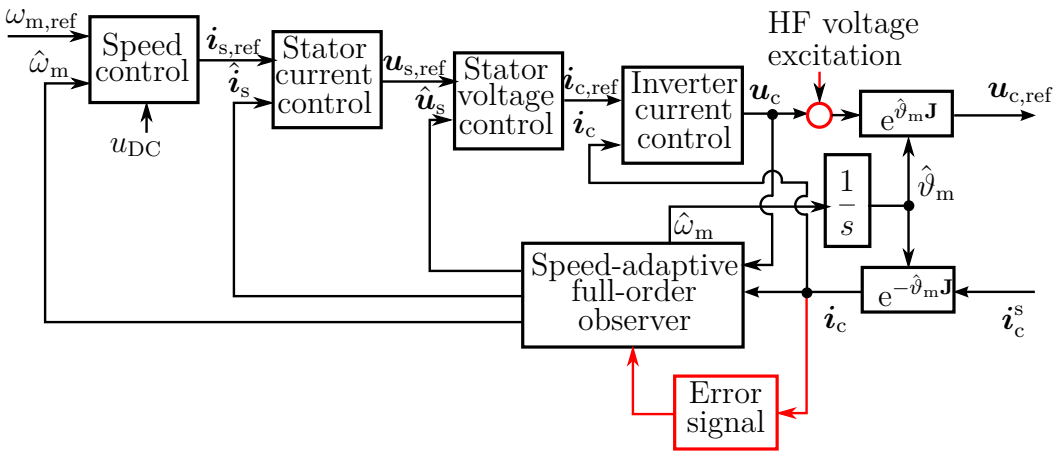

Figure 16: Block diagram of vector control with the speed-adaptive full-order observer and HF signal injection. Adapted from [11].

3.1.2 V/Hz and A/Hz control with stabilizing loop(s)

Open-loop V/Hz control is inherently unstable unless the SM is equipped with a damper winding [32], resulting from a weak coupling between the electrical and mechanical modes of the machine. In other words, slow rotor poles move from the stator poles after exceeding a certain angular speed. Therefore, slow rotor poles appear in the instability region, having small positive real parts. However, V/Hz control can be stabilized by implementing a frequency stabilization loop to locate the rotor poles in the stable region.

A stabilizing loop strategy is applied in the V/Hz control, in which the stabilizing frequency modulation signal is proportional to the input active power perturbations [32]. The active power perturbations are obtained from estimated active power by high-pass filtering. Despite the control being suitable at medium and high speeds for low-performance applications, this control method does not assure high power factor and operation at low speeds.

Consequently, two stabilizing correction loops are presented in [33]: A frequency stability loop, which uses active power variation; and a power factor regulation loop, also named an energy saving loop, is used in a voltage amplitude correction. The control performs well in steady and transient states and at low speeds with a nominal load. Furthermore, this control method has a high disturbance-rejection capability of the rotor speed during loading and unloading [33] (tested at rated speed with rated load). Similarly oriented research paper [34] benefits with having zero reactive power losses and non-oscillatory and robust behavior (tested at rated speed with half of the rated load). However, the control of PMSM drives in [33, 34] becomes challenging when operating at light loads [35]. Moreover, the maximum torque-per-ampere

(MTPA) operation is not assured, which can be optimized by integrating MTPA into the two-loop correction control structures by using two PI controllers [36].

The stability control structures [33,34] are augmented with the LC filter dynamics for industrial applications (mining industry) using the PMSM with the filter, a step-up transformer, and long leads [12,13]. Both methods are based on the amps-per-hertz (A/Hz) control startup procedure. The stability control principle is implemented with a current-regulated A/Hz control in an electric submersible pump application [12]. A similar control strategy is featured in the PMSM drive for a downhole electric drilling [13]. V/Hz control is unsuitable for applications with step-up transformers because the uncontrolled current can vary with the same voltage reference. Moreover, overcurrents may cause the transformer to saturate; hence, the required power is not delivered to the motor [13].

The startup process in [12,13] provides sufficient torque, and the transformer saturation is mitigated. Additionally, both strategies utilize only filter parameters, thus increasing the robustness against parameter errors. However, the performance of the motor drive is limited. The methods are used only in the startup period, and the acceleration of the motor is usually ramped to avoid overcurrent when using A/Hz control methods. After the startup, the A/Hz control is switched to sensorless vector control because of higher efficiency [37]. Based on the review, no convincing results show a scalar control for SMs with LC filters, which is feasible in the whole operating range under loaded conditions.

Control system

A generalized block diagram of the scalar control with stabilizing frequency correction is illustrated in Figure 17. A stabilizing frequency correction loop contains a proportional gain, a high-pass filter (HPF), and a frequency modulator. The proportional gain is used to scale the frequency correction signal. The proportional gain is constant in [13], but it can also be frequency dependent in [12]. The HPF ensures that the frequency correction signal is only effective in the transient state [12]. The algorithm for calculating the perturbation signal for the input of the HPF can vary based on the selected control strategy. The frequency compensation signal is calculated using three-phase currents and voltages (voltage command or voltage feedback) in the stator or rotor coordinates.

The voltage reference $\boldsymbol{u}_{\mathrm{s,ref}}$ for V/Hz control is obtained from the angular speed of the reference frame ω_{s} based on the relation given by

$$\boldsymbol{u}_{\mathrm{s,ref}} = R_{\mathrm{s}}\boldsymbol{i}_{\mathrm{s}} + \omega_{\mathrm{s}}\mathbf{J}\boldsymbol{\psi}_{\mathrm{s,ref}}, \tag{18}$$

where $\boldsymbol{u}_{\mathrm{s,ref}}$ is the stator voltage reference, and $\boldsymbol{\psi}_{\mathrm{s,ref}}$ is the stator flux linkage reference given by the user.

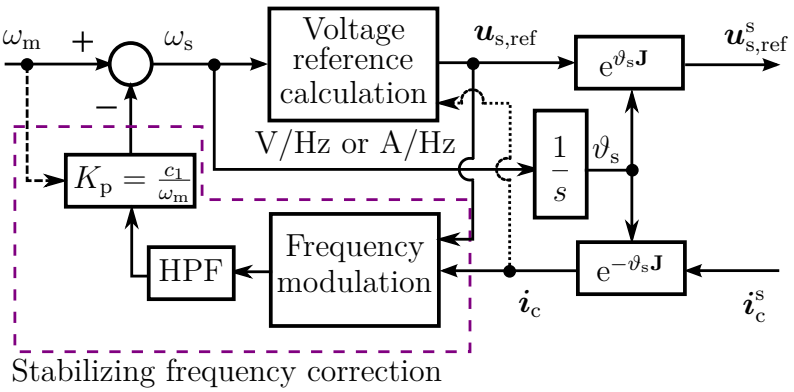

Figure 17: Generalized block diagram of V/Hz and A/Hz control with frequency correction stabilizing loop

3.1.3 Observer-based V/Hz control

A recently developed observer-based V/Hz control method [14] eliminates some of the drawbacks of previously described vector control [11, 27, 28] and V/Hz methods [12, 13, 32–34, 36]. Sensorless vector control methods are infeasible for medium-performance plug-and-play drives because of cascaded control loops and parameter tuning complexity, in some cases relatively high parameter sensitivity, and the need of a separate field-weakening algorithm. However, the observers enable arbitrary pole placement settings, which can be beneficial for stabilizing V/Hz control for SM drives with LC filters.

For the reason of desired pole placement, the heuristic compensators in standard V/Hz control are replaced by a state feedback control law and a flux observer [14]. Additionally, the parameter tuning is simplified by using physically meaningful design parameters according to design guidelines in [24], which originates from the design of observers for sensorless vector control. Furthermore, various SM types can directly apply the same control method because of their general control structure. Based on the system analysis, the entire system is stable and passive in the whole feasible operating range [14]. The observer-based V/Hz control also inherits low parameter sensitivity from the standard V/Hz control structure and automatic field weakening capability (no need to implement a separate field-weakening algorithm).

Control system

State feedback control stabilizes the SM dynamics by a feedback controller, which regulates the system output by tracking a reference input [38]. State feedback calculates the control action for specified system dynamics using a state vector [39]. The state vector consists of state variables, either measured ($\boldsymbol{i}_\mathrm{s}$) or estimated ($\hat{\boldsymbol{\psi}}_\mathrm{s}$; estimated states are marked with the hat). The main benefit of the state feedback control is that the system poles can be arbitrarily placed based on the selected state feedback gain.

A state feedback control law derived in [14] for computing a stator voltage reference $\boldsymbol{u}_{\mathrm{s,ref}}$ for PWM inverter is

$$\boldsymbol{u}_{\mathrm{s,ref}} = R_{\mathrm{s}}\boldsymbol{i}_{\mathrm{s}} + \omega_{\mathrm{s}}\mathbf{J}\boldsymbol{\psi}_{\mathrm{s,ref}} + \boldsymbol{K}_{\mathrm{c}}(\boldsymbol{\psi}_{\mathrm{s,ref}} - \hat{\boldsymbol{\psi}}_{\mathrm{s}}) \tag{19}$$

where $\boldsymbol{K}_{\mathrm{c}}$ is the state feedback control gain and $\hat{\boldsymbol{\psi}}_{\mathrm{s}}$ is the estimated stator flux.

Reduced-order observer model in control coordinates rotating at ω_{s} is defined as [14]

$$\frac{\mathrm{d}\hat{\boldsymbol{\psi}}_{\mathrm{s}}}{\mathrm{d}t} = \boldsymbol{u}_{\mathrm{s,ref}} - R_{\mathrm{s}}\boldsymbol{i}_{\mathrm{s}} - \omega_{\mathrm{s}}\mathbf{J}\hat{\boldsymbol{\psi}}_{\mathrm{s}} + \boldsymbol{K}_{\mathrm{o}}\boldsymbol{e} \tag{20a}$$

$$\frac{\mathrm{d}\hat{\delta}}{\mathrm{d}t} = \boldsymbol{k}_{\mathrm{o}}^{\mathrm{T}}\boldsymbol{e} \tag{20b}$$

where $\hat{\boldsymbol{\psi}}_{\mathrm{s}}$ and $\hat{\delta}$ are the estimated states of the stator flux and the load angle, $\boldsymbol{K}_{\mathrm{o}}$ is the observer gain matrix, $\boldsymbol{k}_{\mathrm{o}}^{\mathrm{T}}$ is the observer gain vector, and $\boldsymbol{e}$ is the correction vector.

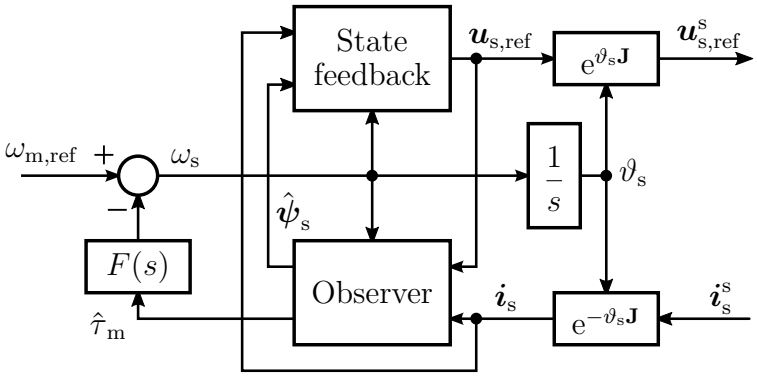

Figure 18: Block diagram of the observer-based V/Hz control system [14]. The state-feedback control law is defined in (19), the HPF transfer function $F(s)$ in (29), and the observer in (20).

3.2 Proposed observer-based V/Hz control for SM drives with LC filter

Figure 19 and Figure 20 show simplified block diagrams of SM drives with the LC filters. The grey areas mark the proposed observer-based V/Hz control methods. Figure 19 shows an observer-based V/Hz control with a reduced-order observer, in which both $\boldsymbol{i}_{\mathrm{c}}$ and $\boldsymbol{i}_{\mathrm{s}}$ are measured. This control method is analogous to the observer-based V/Hz control without the filter (Figure 18), meaning that the observer and state-feedback have similar equations, obtained by a substitution: $\hat{\boldsymbol{\psi}}_{\mathrm{s}} \longrightarrow \hat{\boldsymbol{\psi}}_{\mathrm{c}}$ and $\boldsymbol{u}_{\mathrm{s,ref}} \longrightarrow \boldsymbol{u}_{\mathrm{c,ref}}$. The estimated states from the reduced observer are $\hat{\boldsymbol{\psi}}_{\mathrm{c}}$ and $\hat{\delta}$.

Figure 20 shows an observer-based V/Hz control with a full-order observer, in which only $\boldsymbol{i}_{\mathrm{s}}$ is measured, and $\hat{\boldsymbol{i}}_{\mathrm{c}}$ is estimated. Additionally, stator voltage and converter current are estimated ($\hat{\boldsymbol{u}}_{\mathrm{s}}$ and $\hat{\boldsymbol{i}}_{\mathrm{c}}$).

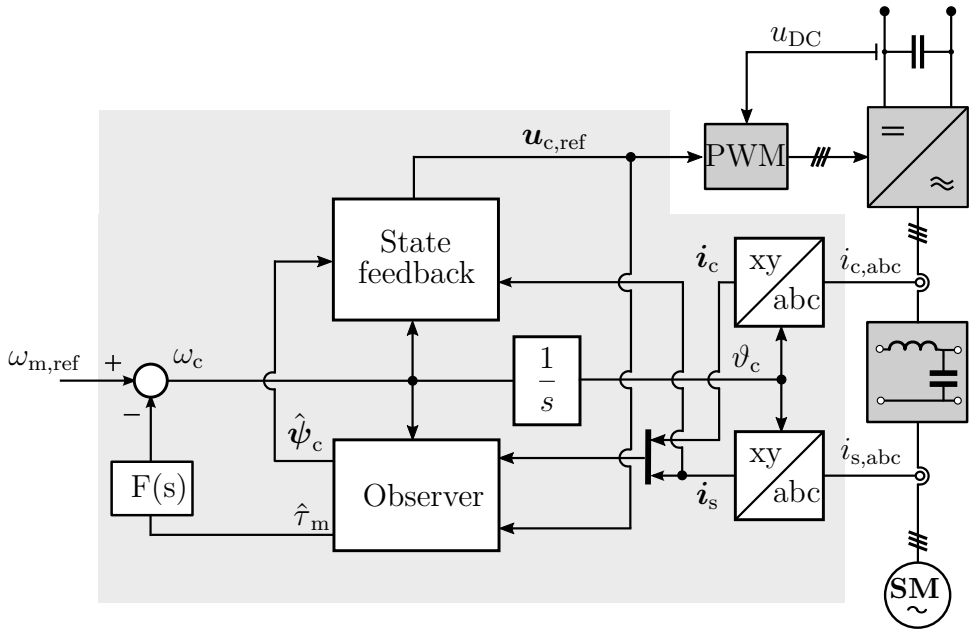

Figure 19: SM drive with the LC filter: V/Hz control with the reduced-order observer.

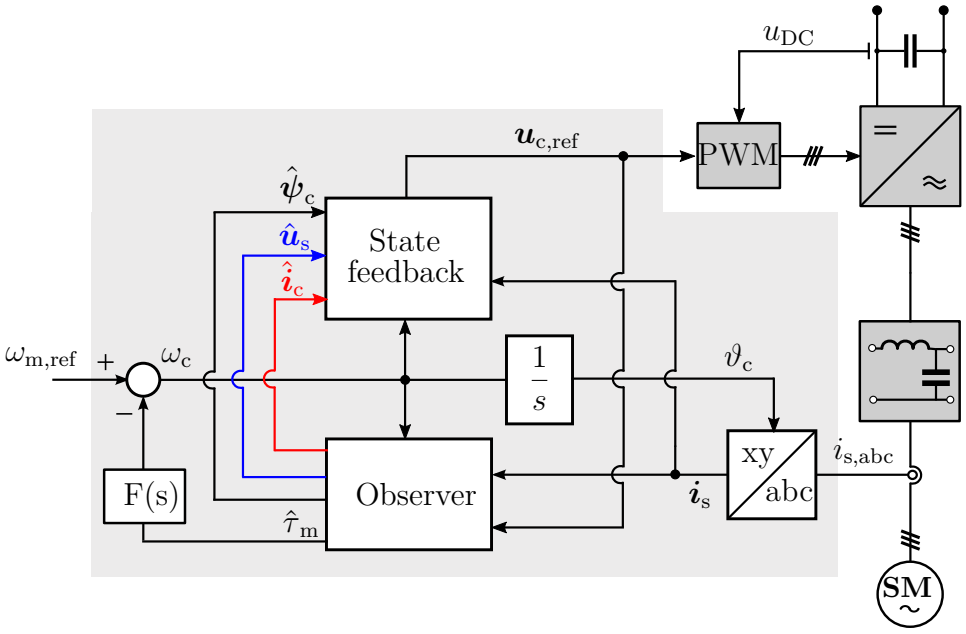

Figure 20: SM drive with the LC filter: V/Hz control with the full-order observer.

3.2.1 State feedback

The voltage reference for the PWM inverter, also known as converter voltage reference $\boldsymbol{u}_{\mathrm{c,ref}}$, is calculated based on the state feedback control law

$$\boldsymbol{u}_{\mathrm{c,ref}} = R_{\mathrm{s}}\boldsymbol{i}_{\mathrm{s}} + \omega_{\mathrm{c}}\mathbf{J}\boldsymbol{\psi}_{\mathrm{c,ref}} + \boldsymbol{K}_{\mathrm{c}}(\boldsymbol{\psi}_{\mathrm{c,ref}} - \hat{\boldsymbol{\psi}}_{\mathrm{c}}) \tag{21a}$$

where $\boldsymbol{\psi}_{\mathrm{c,ref}}$ is the converter flux reference given by the user. The quantities with the hat denote estimated quantities. A simple controller gain matrix $\boldsymbol{K}_{\mathrm{c}} = \alpha_{\mathrm{c}}\mathbf{I}$ is considered throughout the thesis. The selected $\boldsymbol{K}_{\mathrm{c}}$ together with the controller bandwidth $\alpha_{\mathrm{c}} > 0$ guarantees stable flux dynamics in [14].

Subsequently, the second control method with the full-order observer uses state feedback control law

$$\boldsymbol{u}_{\mathrm{c,ref}} = R_{\mathrm{s}}\boldsymbol{i}_{\mathrm{s}} + \omega_{\mathrm{c}}\mathbf{J}\boldsymbol{\psi}_{\mathrm{c,ref}} + \boldsymbol{K}_{\mathrm{c}}(\boldsymbol{\psi}_{\mathrm{c,ref}} - \hat{\boldsymbol{\psi}}_{\mathrm{c}}) - g(\boldsymbol{u}_{\mathrm{s,ref}} - \hat{\boldsymbol{u}}_{\mathrm{s}}) \tag{21b}$$

which contains two error correction gains to minimize the converter flux linkage and the stator voltage errors separately: Positive gain α_{c} is the gain of a closed-loop system, and the control gain g affects damping of the LC filter, and it is used to damp $\boldsymbol{i}_{\mathrm{c}}$. The stator voltage reference $\boldsymbol{u}_{\mathrm{s,ref}}$ is substituted to (21b), which is defined as

$$\boldsymbol{u}_{\mathrm{s,ref}} = R_{\mathrm{s}}\boldsymbol{i}_{\mathrm{s}} + \omega_{\mathrm{c}}\mathbf{J}(\hat{\boldsymbol{\psi}}_{\mathrm{c}} - L_{\mathrm{f}}\hat{\boldsymbol{i}}_{\mathrm{c}}) \tag{21c}$$

It can be noticed that in special case in (21b) is identical with (21a). This special case appears in the condition when $g = 0$ and $\boldsymbol{K}_{\mathrm{c}} = \alpha_{\mathrm{c}}\mathbf{I}$. Therefore, the control law in (21b) can be interpreted as a generalized formulation and used in both control strategies.

3.2.2 State observer

For compactness, let us define the states of the full-order observer. The following expressions are given in estimated synchronous coordinates rotating at ω_{c}

$$\frac{\mathrm{d}\hat{\boldsymbol{i}}_{\mathrm{c}}}{\mathrm{d}t} = \frac{1}{L_{\mathrm{f}}}(\boldsymbol{u}_{\mathrm{c,ref}} - \hat{\boldsymbol{u}}_{\mathrm{s}} - \omega_{\mathrm{c}}L_{\mathrm{f}}\mathbf{J}\hat{\boldsymbol{i}}_{\mathrm{c}} + \boldsymbol{K}_{\mathrm{L}}\boldsymbol{e}) \tag{22a}$$

$$\frac{\mathrm{d}\hat{\boldsymbol{u}}_{\mathrm{s}}}{\mathrm{d}t} = \frac{1}{C_{\mathrm{f}}}(\hat{\boldsymbol{i}}_{\mathrm{c}} - \boldsymbol{i}_{\mathrm{s}} - \omega_{\mathrm{c}}C_{\mathrm{f}}\mathbf{J}\hat{\boldsymbol{u}}_{\mathrm{s}}) \tag{22b}$$

$$\frac{\mathrm{d}\hat{\boldsymbol{\psi}}_{\mathrm{c}}}{\mathrm{d}t} = \boldsymbol{u}_{\mathrm{c,ref}} - R_{\mathrm{s}}\boldsymbol{i}_{\mathrm{s}} - \omega_{\mathrm{c}}\mathbf{J}\hat{\boldsymbol{\psi}}_{\mathrm{c}} + \boldsymbol{K}_{\mathrm{o}}\boldsymbol{e} \tag{22c}$$

$$\frac{\mathrm{d}\hat{\delta}}{\mathrm{d}t} = \boldsymbol{k}_{\mathrm{o}}^{\mathrm{T}}\boldsymbol{e} \tag{22d}$$

Reduced-order observer is composed of the states $\hat{\boldsymbol{\psi}}_{\mathrm{c}}$ and $\hat{\delta}$ from (22). The correction vector $\boldsymbol{e}$ is expressed as

$$\boldsymbol{e} = \boldsymbol{L}_{\mathrm{s}}(\hat{\delta})\boldsymbol{i}_{\mathrm{s}} + \boldsymbol{\psi}_{\mathrm{F}}(\hat{\delta}) - \hat{\boldsymbol{\psi}}_{\mathrm{s}} \tag{23}$$

The vector $\boldsymbol{e}$ differs from the stator flux estimation error $(\boldsymbol{\psi}_\mathrm{s} - \hat{\boldsymbol{\psi}}_\mathrm{s})$ in transient states, because of estimated rotor position; and it is equal to stator current error $(\boldsymbol{i}_\mathrm{s} - \hat{\boldsymbol{i}}_\mathrm{s})$, scaled by the inductance matrix $L_\mathrm{s}(\hat{\delta})$ [24].

Depending on the control method, $\hat{\boldsymbol{\psi}}_\mathrm{s}$ can be either expressed as a function of the measured current or observed converter current as

$$\hat{\boldsymbol{\psi}}_\mathrm{s} = \hat{\boldsymbol{\psi}}_\mathrm{c} - L_\mathrm{f}\boldsymbol{i}_\mathrm{c} \tag{24a}$$

$$\hat{\boldsymbol{\psi}}_\mathrm{s} = \hat{\boldsymbol{\psi}}_\mathrm{c} - L_\mathrm{f}\hat{\boldsymbol{i}}_\mathrm{c} \tag{24b}$$

Furthermore, observer gain matrices for the flux observer $\boldsymbol{K}_\mathrm{o}$ [14], converter current observer $\boldsymbol{K}_\mathrm{L}$ and observer gain vector of the load angle $\boldsymbol{k}_\mathrm{o}^\mathrm{T}$ [14] are defined as

$$\boldsymbol{K}_\mathrm{o} = 2\sigma_\mathrm{o}\frac{\hat{\boldsymbol{\psi}}_\mathrm{a}\hat{\boldsymbol{\psi}}_\mathrm{a}^\mathrm{T}}{\|\hat{\boldsymbol{\psi}}_\mathrm{a}\|^2} \tag{25a}$$

$$\boldsymbol{K}_\mathrm{L} = -\alpha_\mathrm{L}\frac{\hat{\boldsymbol{\psi}}_\mathrm{a}\hat{\boldsymbol{\psi}}_\mathrm{a}^\mathrm{T}}{\|\hat{\boldsymbol{\psi}}_\mathrm{a}\|^2} \tag{25b}$$

$$\boldsymbol{k}_\mathrm{o}^\mathrm{T} = -\alpha_\mathrm{o}\frac{\hat{\boldsymbol{\psi}}_\mathrm{a}^\mathrm{T}\mathbf{J}}{\|\hat{\boldsymbol{\psi}}_\mathrm{a}\|^2} \tag{25c}$$

where superscript T denotes the matrix transpose, σ_o is the desired decay rate of the flux estimation error, α_L is the converter current estimation bandwidth, and α_o is the load-angle estimation bandwidth. The gains selection intents to decouple estimation-error dynamics of the converter current, converter flux, and the load angle. To decouple these mechanical and electrical estimation-error dynamics, the auxiliary flux linkage $\hat{\boldsymbol{\psi}}_\mathrm{a} = \mathbf{J}(\partial\boldsymbol{e}/\partial\hat{\delta})$ [24] is defined as

$$\hat{\boldsymbol{\psi}}_\mathrm{a} = \hat{\boldsymbol{\psi}}_\mathrm{s} + \mathbf{J}\boldsymbol{L}_\mathrm{s}(\hat{\delta})\mathbf{J}\boldsymbol{i}_\mathrm{s} \tag{26}$$

The observer could be further extended with the PM flux adaptation [40]. This additional algorithm is out of the scope of the thesis, and therefore it is not implemented. Furthermore, σ_o can be selected as [14]

$$\sigma_\mathrm{o} = \zeta_\infty|\omega_\mathrm{c}| + \frac{R_\mathrm{s}}{4}\left(\frac{1}{L_\mathrm{d}} + \frac{1}{L_\mathrm{q}}\right) \tag{27}$$

where ζ_∞ is the selected damping ratio at high speeds. If the operating point angular speed is $\omega_{\mathrm{c}0} = 0$ Hz, poles should located at $s = 0$ and $s = -R_\mathrm{s}(L_\mathrm{d}+L_\mathrm{q})/(2L_\mathrm{d}L_\mathrm{q})$ [14]. Therefore, the motor should be magnetized and started in a stable manner. At higher speeds, poles are located at $s = -(\zeta_\infty \pm \mathrm{j}\sqrt{1-\zeta_\infty^2})\|\omega_{\mathrm{c}0}\|$ [14]. For example, if $\zeta_\infty = 0.7$ were chosen, observer poles would have 45° angle with the real axis.

3.2.3 HPF

The HPF output provides a negative feedback to increase the damping of the mechanical system [14]. The synchronous angular speed of xy coordinate system ω_c can be selected as

$$\omega_\mathrm{c} = \omega_\mathrm{m,ref} - g_\tau(\hat{\tau}_\mathrm{m} - \tau_\mathrm{ref}) \tag{28a}$$

where $\omega_{\mathrm{m,ref}}$ is the rate-limited rotor speed reference given by a user, and g_τ is the damping gain. The estimated electromagnetic torque $\hat{\tau}_{\mathrm{m}}$ has equivalent definition as the electromagnetic torque in (7). The only difference is that the estimated stator flux $\hat{\boldsymbol{\psi}}_{\mathrm{s}}$ is used from (24) instead of $\boldsymbol{\psi}_{\mathrm{s}}$. Furthermore, a low-pass-filtered (LPF) torque estimate τ_{ref} dynamics are defined as

$$\frac{\mathrm{d}\tau_{\mathrm{ref}}}{\mathrm{d}t} = \alpha_{\mathrm{f}} \left(\hat{\tau}_{\mathrm{m}} - \tau_{\mathrm{ref}} \right) \tag{28b}$$

where α_{f} is the low-pass filter bandwidth.

By isolating of τ_{ref} for (28b) and further substitution in (28a), the synchronous angular speed ω_{c} can be equivalently expressed as

$$\omega_{\mathrm{c}} = \omega_{\mathrm{m,ref}} - \underbrace{\frac{g_\tau s}{s + \alpha_{\mathrm{f}}}}_{F(s)} \hat{\tau}_{\mathrm{m}} \tag{29}$$

where $s = \mathrm{d}/\mathrm{d}t$ is the Laplace operator. The HPF transfer function $F(s)$ minimizes the angular speed error caused by the DC offset of the estimated load angle.

4 Linearized continuous-time model

4.1 Steady-state operating point

The steady-state operating point can be initially obtained by substituting $\mathrm{d}/\mathrm{d}t = 0$ into state equations for the SM and LC filter models (eq. (11), (9), and (15)). Hence, the steady-state operating point quantities can be expressed as

$$\boldsymbol{i}_{\mathrm{s0}} = \boldsymbol{L}_{\mathrm{s0}}^{-1}\left[\boldsymbol{\psi}_{\mathrm{s0}} - \boldsymbol{\psi}_{\mathrm{f0}}\right] \tag{30a}$$
$$\boldsymbol{i}_{\mathrm{c0}} = \boldsymbol{i}_{\mathrm{s0}} + \omega_{\mathrm{c0}} C_{\mathrm{f}} \mathbf{J} \boldsymbol{u}_{\mathrm{s0}} \tag{30b}$$
$$\boldsymbol{u}_{\mathrm{s0}} = R_{\mathrm{s}} \boldsymbol{i}_{\mathrm{s0}} + \omega_{\mathrm{c0}} \mathbf{J} \boldsymbol{\psi}_{\mathrm{s0}} \tag{30c}$$
$$\boldsymbol{u}_{\mathrm{c0}} = \boldsymbol{u}_{\mathrm{s0}} + \omega_{\mathrm{c0}} L_{\mathrm{f}} \mathbf{J} \boldsymbol{i}_{\mathrm{c0}} \tag{30d}$$

where subscript 0 refers to operating point quantities, such as the operating point stator inductance $\boldsymbol{L}_{\mathrm{s0}} = \boldsymbol{L}_{\mathrm{s}}(\delta_0)$ and operating point PM flux $\boldsymbol{\psi}_{\mathrm{f0}} = \boldsymbol{\psi}_{\mathrm{F}}(\delta_0)$. Stator current operating point equation (30a) cannot be directly used because operating point stator flux $\boldsymbol{\psi}_{\mathrm{s0}}$ is not directly defined in the model. However, it can be derived from the converter flux linkage operating point $\boldsymbol{\psi}_{\mathrm{c0}} = \boldsymbol{\psi}_{\mathrm{s0}} + L_{\mathrm{f}} \boldsymbol{i}_{\mathrm{c0}}$, which further requires a substitution of other operating point quantities from (30b) and (30c). Therefore, the resulting alternative expression for the operating point stator current $\boldsymbol{i}_{\mathrm{s0}}$ is

$$\boldsymbol{i}_{\mathrm{s0}} = \boldsymbol{L}_{\mathrm{sys}}^{-1}\left[\boldsymbol{\psi}_{\mathrm{c0}} - (1 - \omega_{\mathrm{c0}}^2/\omega_{\mathrm{r}}^2)\boldsymbol{\psi}_{\mathrm{f0}}\right] \tag{31a}$$
$$\boldsymbol{L}_{\mathrm{sys}} = (1 - \omega_{\mathrm{c0}}^2/\omega_{\mathrm{r}}^2)\boldsymbol{L}_{\mathrm{s0}} + L_{\mathrm{f}}\mathbf{I} + R_{\mathrm{s}}\omega_{\mathrm{c0}}/\omega_{\mathrm{r}}^2\mathbf{J} \tag{31b}$$

where $\boldsymbol{L}_{\mathrm{sys}}$ denotes the equivalent system inductance, and ω_{r} is the resonance frequency of the filter (13).

Furthermore, the operating point of the converter current $\boldsymbol{i}_{\mathrm{c0}}$ is also obtained from the alternative expression

$$\boldsymbol{i}_{\mathrm{c0}} = \frac{1}{L_{\mathrm{f}}}(\boldsymbol{\psi}_{\mathrm{c0}} - \boldsymbol{\psi}_{\mathrm{s0}}) \tag{31c}$$

where $\boldsymbol{\psi}_{\mathrm{s0}} = \boldsymbol{L}_{\mathrm{s0}}\boldsymbol{i}_{\mathrm{s0}} + \boldsymbol{\psi}_{\mathrm{f0}}$.

As a result, the remaining operating point quantities $\boldsymbol{u}_{\mathrm{s0}}$ and $\boldsymbol{u}_{\mathrm{c0}}$ can be obtained simply from (30c) and (30d), since $\boldsymbol{i}_{\mathrm{c0}}$ and $\boldsymbol{i}_{\mathrm{s0}}$ are already known.

The auxiliary flux operating point $\boldsymbol{\psi}_{\mathrm{a0}}$ is obtained by substituting operating point quantities into (26)

$$\boldsymbol{\psi}_{\mathrm{a0}} = \boldsymbol{\psi}_{\mathrm{s0}} + \mathbf{J}\boldsymbol{L}_{\mathrm{s0}}\mathbf{J}\boldsymbol{i}_{\mathrm{s0}} \tag{32}$$

where the transpose of the auxiliary flux linkage is $\boldsymbol{\psi}_{\mathrm{a0}}^T = \boldsymbol{\psi}_{\mathrm{s0}}^T + \boldsymbol{i}_{\mathrm{s0}}^T\mathbf{J}\boldsymbol{L}_{\mathrm{s0}}\mathbf{J}$.

4.2 Linearized model

4.2.1 Preliminaries

The SM with the LC filter is a non-linear system that consists of non-linear differential equations. However, the system analysis and control design are less difficult for

linear systems. Therefore, the non-linear system is reduced to a linear one using a small-signal linearization.

A small-signal linearization is a practical approach for analyzing the system stability. The main idea is based on the stability of the linearized system near a small vicinity of the operating point. The non-linear system is stable in a region with an equilibrium if the small-signal linearized model is stable and valid near the equilibrium [41]. The equilibrium for the stator flux is obtained by subtracting the stator flux from its operating point, denoted by $\Delta\boldsymbol{\psi}_\mathrm{s} = \boldsymbol{\psi}_\mathrm{s} - \boldsymbol{\psi}_\mathrm{s0}$. Other quantities, such as currents and voltages used in the small-signal linearized model, are similarly presented (marked with Δ).

Let us linearize some of the important quantities used in this chapter. First, linearization of stator flux, which is obtained by isolating $\boldsymbol{\psi}_\mathrm{s}$ in (11), gives us:

$$\Delta\boldsymbol{\psi}_\mathrm{s} = \boldsymbol{L}_\mathrm{s0}\Delta\boldsymbol{i}_\mathrm{s} - \mathbf{J}\boldsymbol{\psi}_\mathrm{a0}\Delta\delta \tag{33}$$

Consequently, a linearized stator current $\Delta\boldsymbol{i}_\mathrm{s}$ is expressed as

$$\Delta\boldsymbol{i}_\mathrm{s} = \boldsymbol{L}_\mathrm{s0}^{-1}(\Delta\boldsymbol{\psi}_\mathrm{s} + \mathbf{J}\boldsymbol{\psi}_\mathrm{a0}\Delta\delta) \tag{34}$$

A linearized stator flux linkage $\Delta\boldsymbol{\psi}_\mathrm{s}$ can be alternatively expressed as

$$\Delta\boldsymbol{\psi}_\mathrm{s} = \Delta\boldsymbol{\psi}_\mathrm{c} - L_\mathrm{f}\Delta\boldsymbol{i}_\mathrm{c} \tag{35}$$

Furthermore, the electromagnetic torque expression used in (7) is also linearized

$$\Delta\tau_\mathrm{m} = \frac{3p}{2}(\boldsymbol{i}_\mathrm{s0}^T\mathbf{J}\Delta\boldsymbol{\psi}_\mathrm{s} + \Delta\boldsymbol{i}_\mathrm{s}^T\mathbf{J}\boldsymbol{\psi}_\mathrm{s0}) = \frac{3p}{2}(\boldsymbol{i}_\mathrm{s0}^T\mathbf{J}\Delta\boldsymbol{\psi}_\mathrm{s} - \boldsymbol{\psi}_\mathrm{s0}^T\mathbf{J}\Delta\boldsymbol{i}_\mathrm{s}) \tag{36}$$

The operating point stator flux transpose $\boldsymbol{\psi}_\mathrm{s0}^T$ can be replaced by defined auxiliary flux transpose $\boldsymbol{\psi}_\mathrm{a0}^T$ in (32) to simplify the linearized torque expression. Furthermore, the expression could be alternatively expressed as a function of the linearized converter flux linkage, converter current, and angle by substitution of $\Delta\boldsymbol{i}_\mathrm{s}$ in (34) and $\Delta\boldsymbol{\psi}_\mathrm{s}$ obtained from (35)

$$\Delta\tau_\mathrm{m} = \frac{3p}{2}\left(\boldsymbol{\psi}_\mathrm{a0}^\mathrm{T}\mathbf{J}\boldsymbol{L}_\mathrm{s0}^{-1}L_\mathrm{f}\Delta\boldsymbol{i}_\mathrm{c} - \boldsymbol{\psi}_\mathrm{a0}^\mathrm{T}\mathbf{J}\boldsymbol{L}_\mathrm{s0}^{-1}\Delta\boldsymbol{\psi}_\mathrm{c} + \underbrace{\boldsymbol{\psi}_\mathrm{a0}^\mathrm{T}\left(\boldsymbol{i}_\mathrm{s0} - \mathbf{J}\boldsymbol{L}_\mathrm{s0}^{-1}\mathbf{J}\boldsymbol{\psi}_\mathrm{a0}\right)}_{c}\Delta\delta\right) \tag{37}$$

Another preliminary concept used in this chapter is an estimated quantity. Estimated quantities are obtained from a state observer, which includes an estimation error with respect to the actual quantity. In other words, the estimation error is a difference between the actual and estimated quantity. For example, the estimation error of the converter flux linkage is

$$\tilde{\boldsymbol{\psi}}_\mathrm{c} = \boldsymbol{\psi}_\mathrm{c} - \hat{\boldsymbol{\psi}}_\mathrm{c} \tag{38a}$$

Hence, its linearized form is

$$\Delta\tilde{\boldsymbol{\psi}}_\mathrm{c} = \Delta\boldsymbol{\psi}_\mathrm{c} - \Delta\hat{\boldsymbol{\psi}}_\mathrm{c} \tag{38b}$$

Alternatively, other quantities such as a converter current estimation error $\Delta\tilde{\boldsymbol{i}}_\mathrm{c}$, a stator voltage estimation error $\Delta\tilde{\boldsymbol{u}}_\mathrm{s}$, and a load angle estimation error $\Delta\tilde{\delta}$ are derived similarly.

4.2.2 Linearized system model

The linearized system model state equations, which are obtained from (9), (15) and (17), are presented as

$$\frac{\mathrm{d}\Delta \boldsymbol{i}_\mathrm{c}}{\mathrm{d}t} = -\omega_{\mathrm{c}0}\mathbf{J}\Delta \boldsymbol{i}_\mathrm{c} - \frac{\Delta \boldsymbol{u}_\mathrm{s}}{L_\mathrm{f}} + \frac{\Delta \boldsymbol{u}_\mathrm{c}}{L_\mathrm{f}} - \mathbf{J}\boldsymbol{i}_{\mathrm{c}0}\Delta\omega_\mathrm{c} \tag{39a}$$

$$\frac{\mathrm{d}\Delta \boldsymbol{u}_\mathrm{s}}{\mathrm{d}t} = \frac{\Delta \boldsymbol{i}_\mathrm{c}}{C_\mathrm{f}} - \omega_{\mathrm{c}0}\mathbf{J}\Delta \boldsymbol{u}_\mathrm{s} - \frac{\Delta \boldsymbol{i}_\mathrm{s}}{C_\mathrm{f}} - \mathbf{J}\boldsymbol{u}_{\mathrm{s}0}\Delta\omega_\mathrm{c} \tag{39b}$$

$$\frac{\mathrm{d}\Delta \boldsymbol{\psi}_\mathrm{c}}{\mathrm{d}t} = \Delta \boldsymbol{u}_\mathrm{c} - \omega_{\mathrm{c}0}\mathbf{J}\Delta \boldsymbol{\psi}_\mathrm{c} - R_\mathrm{s}\Delta \boldsymbol{i}_\mathrm{s} - \mathbf{J}\boldsymbol{\psi}_{\mathrm{c}0}\Delta\omega_\mathrm{c} \tag{39c}$$

$$\frac{\mathrm{d}\Delta \delta}{\mathrm{d}t} = \Delta\omega_\mathrm{c} - \Delta\omega_\mathrm{m} \tag{39d}$$

where the inputs of the system are the converter voltage $\Delta \boldsymbol{u}_\mathrm{c}$, the angular speed $\Delta\omega_\mathrm{c}$ of the control coordinates frame, and the angular rotor speed $\Delta\omega_\mathrm{m}$. The linearized stator current $\Delta \boldsymbol{i}_\mathrm{s}$ (34) can be immediately substituted to the linearized state space model.

4.2.3 LPF dynamics

The HPF presented in Section 3.2.3 is linear. Nevertheless, small-signal notation is used for clear interpretation. LPF dynamics in (28b) are therefore expressed as

$$\frac{\mathrm{d}\Delta \tau_\mathrm{ref}}{\mathrm{d}t} = \alpha_\mathrm{f}(\Delta\hat{\tau}_\mathrm{m} - \Delta\tau_\mathrm{ref}) \tag{40}$$

where the linearized electromagnetic torque estimate $\Delta\hat{\tau}_\mathrm{m}$ can be further developed in similar manner as $\Delta\tau_\mathrm{m}$ in (37), which leads to

$$\begin{aligned}\Delta\hat{\tau}_\mathrm{m} =& \frac{3p}{2}[\boldsymbol{\psi}_{\mathrm{a}0}^\mathrm{T}\mathbf{J}\boldsymbol{L}_{\mathrm{s}0}^{-1}L_\mathrm{f}\Delta \boldsymbol{i}_\mathrm{c} - \boldsymbol{\psi}_{\mathrm{a}0}^\mathrm{T}\mathbf{J}\boldsymbol{L}_{\mathrm{s}0}^{-1}\Delta \boldsymbol{\psi}_\mathrm{c} + \underbrace{\boldsymbol{\psi}_{\mathrm{a}0}^\mathrm{T}\left(\boldsymbol{i}_{\mathrm{s}0} - \mathbf{J}\boldsymbol{L}_{\mathrm{s}0}^{-1}\mathbf{J}\boldsymbol{\psi}_{\mathrm{a}0}\right)}_{c}\Delta\delta \\ &+ \boldsymbol{i}_{\mathrm{s}0}^\mathrm{T}\mathbf{J}L_\mathrm{f}\Delta\tilde{\boldsymbol{i}}_\mathrm{c} - \boldsymbol{i}_{\mathrm{s}0}^\mathrm{T}\mathbf{J}\Delta\tilde{\boldsymbol{\psi}}_\mathrm{c}]\end{aligned} \tag{41}$$

Please notice that the above expression considers the converter current estimation error $\Delta\tilde{\boldsymbol{i}}_\mathrm{c}$. However, in the case when the converter current $\boldsymbol{i}_\mathrm{c}$ is measured, $\Delta\tilde{\boldsymbol{i}}_\mathrm{c} = 0$ and therefore the term $\boldsymbol{i}_{\mathrm{s}0}^\mathrm{T}\mathbf{J}L_\mathrm{f}\Delta\tilde{\boldsymbol{i}}_\mathrm{c}$ disappears. Another important assumption in the model is the equality of the control model and plant model parameters. Therefore, parameter error quantities are neglected.

4.2.4 Linearized mechanical dynamics

Mechanical subsystem used in (8) is linearized and $\Delta\tau_\mathrm{m}$ further substituted from (37), which leads to

$$\frac{\mathrm{d}\Delta\omega_\mathrm{m}}{\mathrm{d}t} = \frac{p}{J_\mathrm{m}}\frac{3p}{2}(\boldsymbol{\psi}_{\mathrm{a}0}^T\mathbf{J}\boldsymbol{L}_{\mathrm{s}0}^{-1}L_\mathrm{f}\Delta \boldsymbol{i}_\mathrm{c} - \boldsymbol{\psi}_{\mathrm{a}0}^T\mathbf{J}\boldsymbol{L}_{\mathrm{s}0}^{-1}\Delta \boldsymbol{\psi}_\mathrm{c} + c\Delta\delta) - \frac{p}{J_\mathrm{m}}\Delta\tau_\mathrm{L} \tag{42}$$

4.2.5 Linearized state feedback control laws

The control law, for which both currents are measured (21a), is further linearized

$$\Delta \boldsymbol{u}_\mathrm{c} = R_\mathrm{s}\Delta \boldsymbol{i}_\mathrm{s} + (\omega_\mathrm{c0}\mathbf{J} + \boldsymbol{K}_\mathrm{c})\Delta\boldsymbol{\psi}_\mathrm{c,ref} + \mathbf{J}\boldsymbol{\psi}_\mathrm{c0}\Delta\omega_\mathrm{c} - \boldsymbol{K}_\mathrm{c}\Delta\hat{\boldsymbol{\psi}}_\mathrm{c} \tag{43a}$$

Subsequently, second control method, where only stator current is measured (21b), is also linearized

$$\begin{aligned}\Delta \boldsymbol{u}_\mathrm{c} = {} & g\omega_\mathrm{c0}\mathbf{J}L_\mathrm{f}\Delta\hat{\boldsymbol{i}}_\mathrm{c} + g\Delta\hat{\boldsymbol{u}}_\mathrm{s} + (1-g)R_\mathrm{s}\Delta\boldsymbol{i}_\mathrm{s} - (\alpha_\mathrm{c}\mathbf{I} + g\omega_\mathrm{c0}\mathbf{J})\Delta\hat{\boldsymbol{\psi}}_\mathrm{c} \\ & + \mathbf{J}(\boldsymbol{\psi}_\mathrm{c0} - g\boldsymbol{\psi}_\mathrm{s0})\Delta\omega_\mathrm{c} + (\alpha_\mathrm{c}\mathbf{I} + \omega_\mathrm{c0}\mathbf{J})\Delta\boldsymbol{\psi}_\mathrm{c,ref}\end{aligned} \tag{43b}$$

where the linearized internal stator frequency of the control coordinate system $\Delta\omega_\mathrm{c}$ from (28a) is expressed as

$$\Delta\omega_\mathrm{c} = \Delta\omega_\mathrm{m,ref} - g_\tau(\Delta\hat{\tau}_\mathrm{m} - \Delta\tau_\mathrm{ref}) \tag{44}$$

4.2.6 Linearized estimation-error dynamics of the state observer

Derivatives of estimation-error quantities with respect to time are obtained by subtraction of observer state equations (22) from large-signal system model state equations ((9),(17) and (15)) followed by the small-signal linearization. Consequently, a small-signal linearized model of observer estimation-error dynamics is

$$\frac{\mathrm{d}\Delta\tilde{\boldsymbol{i}}_\mathrm{c}}{\mathrm{d}t} = -(\omega_\mathrm{c0}\mathbf{J} - \boldsymbol{K}_\mathrm{L})\Delta\tilde{\boldsymbol{i}}_\mathrm{c} - \frac{\Delta\tilde{\boldsymbol{u}}_\mathrm{s}}{L_\mathrm{f}} - \frac{\boldsymbol{K}_\mathrm{L}}{L_\mathrm{f}}(\Delta\tilde{\boldsymbol{\psi}}_\mathrm{c} + \mathbf{J}\boldsymbol{\psi}_\mathrm{a0}\Delta\tilde{\delta}) \tag{45a}$$

$$\frac{\mathrm{d}\Delta\tilde{\boldsymbol{u}}_\mathrm{s}}{\mathrm{d}t} = \frac{\Delta\tilde{\boldsymbol{i}}_\mathrm{c}}{C_\mathrm{f}} - \omega_\mathrm{c0}\mathbf{J}\Delta\tilde{\boldsymbol{u}}_\mathrm{s} \tag{45b}$$

$$\frac{\mathrm{d}\Delta\tilde{\boldsymbol{\psi}}_\mathrm{c}}{\mathrm{d}t} = L_\mathrm{f}\boldsymbol{K}_\mathrm{o}\Delta\tilde{\boldsymbol{i}}_\mathrm{c} - (\omega_\mathrm{c0}\mathbf{J} + \boldsymbol{K}_\mathrm{o})\Delta\tilde{\boldsymbol{\psi}}_\mathrm{c} - \boldsymbol{K}_\mathrm{o}\mathbf{J}\boldsymbol{\psi}_\mathrm{a0}\Delta\tilde{\delta} \tag{45c}$$

$$\frac{\mathrm{d}\Delta\tilde{\delta}}{\mathrm{d}t} = L_\mathrm{f}\boldsymbol{k}_\mathrm{o}^\mathrm{T}\Delta\tilde{\boldsymbol{i}}_\mathrm{c} - \boldsymbol{k}_\mathrm{o}^\mathrm{T}\Delta\tilde{\boldsymbol{\psi}}_\mathrm{c} - \boldsymbol{k}_\mathrm{o}^\mathrm{T}\mathbf{J}\boldsymbol{\psi}_\mathrm{a0}\Delta\tilde{\delta} + \Delta\omega_\mathrm{c} - \Delta\omega_\mathrm{m} \tag{45d}$$

As a result of using design guidelines in [24], terms $\boldsymbol{K}_\mathrm{L}\mathbf{J}\boldsymbol{\psi}_\mathrm{a0} = \mathbf{0}_{2,1}$ and $\boldsymbol{K}_\mathrm{o}\mathbf{J}\boldsymbol{\psi}_\mathrm{a0} = \mathbf{0}_{2,1}$ allow decoupling of the load angle from converter current estimation dynamics and converter flux linkage estimation dynamics, respectively. This gain choice aims to possibly passivate the system.

4.2.7 Closed-loop system

State feedback control

The state space representation of the linearized system model in (39):

$$\frac{\mathrm{d}\Delta\boldsymbol{x}}{\mathrm{d}t} = \underbrace{\begin{bmatrix} -\omega_{\mathrm{c}0}\mathbf{J} & -L_{\mathrm{f}}^{-1}\mathbf{I} & \mathbf{0} & \mathbf{0}_{2,1} \\ C_{\mathrm{f}}^{-1}(\mathbf{I}+L_{\mathrm{f}}\boldsymbol{L}_{\mathrm{s}0}^{-1}) & -\omega_{\mathrm{c}0}\mathbf{J} & -C_{\mathrm{f}}^{-1}\boldsymbol{L}_{\mathrm{s}0}^{-1} & -C_{\mathrm{f}}^{-1}\boldsymbol{L}_{\mathrm{s}0}^{-1}\mathbf{J}\boldsymbol{\psi}_{\mathrm{a}0} \\ R_{\mathrm{s}}L_{\mathrm{f}}\boldsymbol{L}_{\mathrm{s}0}^{-1} & \mathbf{0} & -(\omega_{\mathrm{c}0}\mathbf{J}+R_{\mathrm{s}}\boldsymbol{L}_{\mathrm{s}0}^{-1}) & -R_{\mathrm{s}}\boldsymbol{L}_{\mathrm{s}0}^{-1}\mathbf{J}\boldsymbol{\psi}_{\mathrm{a}0} \\ \mathbf{0}_{1,2} & \mathbf{0}_{1,2} & \mathbf{0}_{1,2} & 0 \end{bmatrix}}_{\boldsymbol{A}}\Delta\boldsymbol{x} + \underbrace{\begin{bmatrix} L_{\mathrm{f}}^{-1}\mathbf{I} \\ \mathbf{0} \\ \mathbf{I} \\ \mathbf{0}_{1,2} \end{bmatrix}}_{\boldsymbol{B}}\Delta\boldsymbol{u}_{\mathrm{c}} + \underbrace{\begin{bmatrix} -\mathbf{J}\boldsymbol{i}_{\mathrm{c}0} \\ -\mathbf{J}\boldsymbol{u}_{\mathrm{c}0} \\ -\mathbf{J}\boldsymbol{\psi}_{\mathrm{s}0} \\ 1 \end{bmatrix}}_{\boldsymbol{b}_{\boldsymbol{\omega}}}\Delta\omega_{\mathrm{c}} + \underbrace{\begin{bmatrix} \mathbf{0}_{2,1} \\ \mathbf{0}_{2,1} \\ \mathbf{0}_{2,1} \\ -1 \end{bmatrix}}_{\boldsymbol{b}_{\mathbf{m}}}\Delta\omega_{\mathrm{m}} \tag{46a}$$

where $\Delta\boldsymbol{x} = [\Delta\boldsymbol{i}_{\mathrm{c}}^{\mathrm{T}}, \Delta\boldsymbol{u}_{\mathrm{s}}^{\mathrm{T}}, \Delta\boldsymbol{\psi}_{\mathrm{c}}^{\mathrm{T}}, \Delta\delta]^{\mathrm{T}}$, is the state vector and the proposed gain design is used. The output equation for the electromagnetic torque originates from (37) and can be written as

$$\Delta\tau_{\mathrm{m}} = \frac{3p}{2}\underbrace{\begin{bmatrix}\boldsymbol{\psi}_{\mathrm{a}0}^{\mathrm{T}}\mathbf{J}\boldsymbol{L}_{\mathrm{s}0}^{-1}L_{\mathrm{f}} & \mathbf{0}_{1,2} & -\boldsymbol{\psi}_{\mathrm{a}0}^{\mathrm{T}}\mathbf{J}\boldsymbol{L}_{\mathrm{s}0}^{-1} & c\end{bmatrix}}_{\boldsymbol{c}_{\tau}^{\mathrm{T}}}\Delta\boldsymbol{x} \tag{46b}$$

and the output equation for the converter flux linkage is

$$\Delta\boldsymbol{\psi}_{\mathrm{c}} = \underbrace{\begin{bmatrix}\mathbf{0} & \mathbf{0} & I & \mathbf{0}_{2,1}\end{bmatrix}}_{\boldsymbol{C}}\Delta\boldsymbol{x} \tag{46c}$$

The linearized state feedback control law from (43a) is

$$\begin{aligned}\Delta\boldsymbol{u}_{\mathrm{c}} = &\underbrace{\begin{bmatrix}-R_{\mathrm{s}}\boldsymbol{L}_{\mathrm{s}0}^{-1}L_{\mathrm{f}}, & \mathbf{0}, & R_{\mathrm{s}}\boldsymbol{L}_{\mathrm{s}0}^{-1}-\boldsymbol{K}_{\mathrm{c}}, & R_{\mathrm{s}}\boldsymbol{L}_{\mathrm{s}0}^{-1}\mathbf{J}\boldsymbol{\psi}_{\mathrm{a}0}\end{bmatrix}}_{\boldsymbol{K}}\Delta\boldsymbol{x}+ \\ &+\underbrace{\begin{bmatrix}\boldsymbol{K}_{\mathrm{c}}, & \mathbf{0}_{2,1}\end{bmatrix}}_{\tilde{\boldsymbol{K}}}\Delta\tilde{\boldsymbol{x}} + \underbrace{\mathbf{J}\boldsymbol{\psi}_{\mathrm{c}0}}_{\boldsymbol{k}}\Delta\omega_{\mathrm{c}} + \underbrace{(\boldsymbol{K}_{\mathrm{c}}+\omega_{\mathrm{c}0}\mathbf{J})}_{\boldsymbol{K}_{\mathbf{t}}}\Delta\boldsymbol{\psi}_{\mathrm{c,ref}}\end{aligned} \tag{47a}$$

where $\Delta\tilde{\boldsymbol{x}} = [\Delta\tilde{\boldsymbol{\psi}}_{\mathrm{c}}^{\mathrm{T}}, \Delta\tilde{\delta}]^{\mathrm{T}}$, is the reduced-order observer error vector. The linearized control law used in (43b) is

$$\begin{aligned}\Delta\boldsymbol{u}_{\mathrm{c}} = &\underbrace{\begin{bmatrix}g\omega_{\mathrm{c}0}\mathbf{J}L_{\mathrm{f}}-g^{'}R_{\mathrm{s}}\boldsymbol{L}_{\mathrm{s}0}^{-1}L_{\mathrm{f}}, & g\mathbf{I}, & g^{'}R_{\mathrm{s}}\boldsymbol{L}_{\mathrm{s}0}^{-1}-\alpha_{\mathrm{c}}\mathbf{I}-g\omega_{\mathrm{c}0}\mathbf{J}, & g^{'}R_{\mathrm{s}}\boldsymbol{L}_{\mathrm{s}0}^{-1}\mathbf{J}\boldsymbol{\psi}_{\mathrm{a}0}\end{bmatrix}}_{\boldsymbol{K}}\Delta\boldsymbol{x}+ \\ &+\underbrace{\begin{bmatrix}-g\omega_{\mathrm{c}0}\mathbf{J}L_{\mathrm{f}}, & -g\mathbf{I}, & \alpha_{\mathrm{c}}\mathbf{I}+g\omega_{\mathrm{c}0}\mathbf{J}, & \mathbf{0}_{2,1}\end{bmatrix}}_{\tilde{\boldsymbol{K}}}\Delta\tilde{\boldsymbol{x}}+ \\ &+\underbrace{\mathbf{J}(\boldsymbol{\psi}_{\mathrm{c}0}-g\boldsymbol{\psi}_{\mathrm{s}0})}_{\boldsymbol{k}}\Delta\omega_{\mathrm{c}} + \underbrace{(\alpha_{\mathrm{c}}\mathbf{I}+\omega_{\mathrm{c}0}\mathbf{J})}_{\boldsymbol{K}_{\mathbf{t}}}\Delta\boldsymbol{\psi}_{\mathrm{c,ref}}\end{aligned} \tag{47b}$$

where $g^{'} = 1 - g$ and $\Delta\tilde{\boldsymbol{x}} = [\Delta\tilde{\boldsymbol{i}}_{\mathrm{c}}^{\mathrm{T}}, \Delta\tilde{\boldsymbol{u}}_{\mathrm{s}}^{\mathrm{T}}, \Delta\tilde{\boldsymbol{\psi}}_{\mathrm{c}}^{\mathrm{T}}, \Delta\tilde{\delta}]^{\mathrm{T}}$, is the full-order observer error vector. The general form of the closed-loop system is

$$\frac{\mathrm{d}\Delta\boldsymbol{x}}{\mathrm{d}t} = \underbrace{(\boldsymbol{A} + \boldsymbol{B}\boldsymbol{K})}_{\boldsymbol{A}_{\mathrm{c}}}\Delta\boldsymbol{x} + \boldsymbol{B}\tilde{\boldsymbol{K}}\Delta\tilde{\boldsymbol{x}} + \underbrace{(\boldsymbol{B}\boldsymbol{k} + \boldsymbol{b}_{\boldsymbol{\omega}})}_{\boldsymbol{b}_{\mathrm{c}}}\Delta\omega_{\mathrm{c}} + \boldsymbol{b}_{\mathbf{m}}\Delta\omega_{\mathrm{m}} + \boldsymbol{B}\boldsymbol{K}_{\mathbf{t}}\Delta\boldsymbol{\psi}_{\mathrm{c,ref}} \quad (48)$$

Reduced-order observer estimation-error dynamics

Linearized reduced-order observer estimates are $\Delta\hat{\boldsymbol{\psi}}_{\mathrm{c}}$ and $\Delta\hat{\delta}$. Therefore, the estimation-error dynamics from (45) can be presented in the state space form as

$$\frac{\mathrm{d}\Delta\tilde{\boldsymbol{x}}}{\mathrm{d}t} = \underbrace{\begin{bmatrix} -(\omega_{\mathrm{c}0}\mathbf{J} + \boldsymbol{K}_{\mathrm{o}}) & \mathbf{0}_{2,1} \\ -\boldsymbol{k}_{\mathrm{o}}^{\mathrm{T}} & -\boldsymbol{k}_{\mathrm{o}}^{\mathrm{T}}\mathbf{J}\boldsymbol{\psi}_{\mathrm{a}0} \end{bmatrix}}_{\boldsymbol{A}_{\mathrm{o}}}\Delta\tilde{\boldsymbol{x}} + \underbrace{\begin{bmatrix} \mathbf{0}_{2,1} \\ 1 \end{bmatrix}}_{\boldsymbol{b}_{\mathrm{o}}}\Delta\omega_{\mathrm{c}} + \underbrace{\begin{bmatrix} \mathbf{0}_{2,1} \\ -1 \end{bmatrix}}_{\boldsymbol{b}_{\mathbf{mo}}}\Delta\omega_{\mathrm{m}} \quad (49a)$$

Full-order observer estimation-error dynamics

Alternatively, estimation-error dynamics of the full-order observer (45) are presented in the state space form as

$$\frac{\mathrm{d}\Delta\tilde{\boldsymbol{x}}}{\mathrm{d}t} = \underbrace{\begin{bmatrix} -(\omega_{\mathrm{c}0}\mathbf{J} - \boldsymbol{K}_{\mathrm{L}}) & -L_{\mathrm{f}}^{-1}\mathbf{I} & -L_{\mathrm{f}}^{-1}\boldsymbol{K}_{\mathrm{L}} & \mathbf{0}_{2,1} \\ C_{\mathrm{f}}^{-1}\mathbf{I} & -\omega_{\mathrm{c}0}\mathbf{J} & \mathbf{0} & \mathbf{0}_{2,1} \\ L_{\mathrm{f}}\boldsymbol{K}_{\mathrm{o}} & \mathbf{0} & -(\omega_{\mathrm{c}0}\mathbf{J} + \boldsymbol{K}_{\mathrm{o}}) & \mathbf{0}_{2,1} \\ L_{\mathrm{f}}\boldsymbol{k}_{\mathrm{o}}^{\mathrm{T}} & \mathbf{0}_{1,2} & -\boldsymbol{k}_{\mathrm{o}}^{\mathrm{T}} & -\boldsymbol{k}_{\mathrm{o}}^{\mathrm{T}}\mathbf{J}\boldsymbol{\psi}_{\mathrm{a}0} \end{bmatrix}}_{\boldsymbol{A}_{\mathrm{o}}}\Delta\tilde{\boldsymbol{x}}$$
$$+ \underbrace{\begin{bmatrix} \mathbf{0}_{2,1} \\ \mathbf{0}_{2,1} \\ \mathbf{0}_{2,1} \\ 1 \end{bmatrix}}_{\boldsymbol{b}_{\mathrm{o}}}\Delta\omega_{\mathrm{c}} + \underbrace{\begin{bmatrix} \mathbf{0}_{2,1} \\ \mathbf{0}_{2,1} \\ \mathbf{0}_{2,1} \\ -1 \end{bmatrix}}_{\boldsymbol{b}_{\mathbf{mo}}}\Delta\omega_{\mathrm{m}} \quad (49b)$$

Overall system

A simplified general form of state space representation of the overall system containing state vectors $\Delta\boldsymbol{x}$ and $\Delta\tilde{\boldsymbol{x}}$ is

$$\begin{bmatrix} \frac{\mathrm{d}\Delta\boldsymbol{x}}{\mathrm{d}t} \\ \frac{\mathrm{d}\Delta\tilde{\boldsymbol{x}}}{\mathrm{d}t} \end{bmatrix} = \underbrace{\begin{bmatrix} \boldsymbol{A}_{\mathrm{c}} & \boldsymbol{B}\tilde{\boldsymbol{K}} \\ \mathbf{0}_{m,7} & \boldsymbol{A}_{\mathrm{o}} \end{bmatrix}}_{\boldsymbol{A}_{\mathrm{s}}}\underbrace{\begin{bmatrix} \Delta\boldsymbol{x} \\ \Delta\tilde{\boldsymbol{x}} \end{bmatrix}}_{\Delta\boldsymbol{x}_{\mathrm{s}}} + \underbrace{\begin{bmatrix} \boldsymbol{b}_{\mathrm{c}} \\ \boldsymbol{b}_{\mathrm{o}} \end{bmatrix}}_{\boldsymbol{b}_{\mathbf{s}\boldsymbol{\omega},\mathbf{ref}}}\Delta\omega_{\mathrm{c}} + \underbrace{\begin{bmatrix} \boldsymbol{b}_{\mathbf{m}} \\ \boldsymbol{b}_{\mathbf{mo}} \end{bmatrix}}_{\boldsymbol{b}_{\mathbf{s}\boldsymbol{\omega}}}\Delta\omega_{\mathrm{m}} +$$
$$+ \underbrace{\begin{bmatrix} \boldsymbol{B}\boldsymbol{K}_{\mathbf{t}} \\ \mathbf{0}_{m,2} \end{bmatrix}}_{\boldsymbol{B}_{\boldsymbol{\psi}}}\Delta\boldsymbol{\psi}_{\mathrm{c,ref}} \quad (50)$$

where the number of rows m of zero matrices depends on the observer type. In the case of the reduced-order observer $m = 3$ and for the full-order observer $m = 7$. The HPF is not included in the previous state space representations. Additionally,

the mechanical subsystem is also not present there. Hence, the final state space representation of the overall system with mechanical dynamics and LPF dynamics is

$$\begin{bmatrix} \frac{\mathrm{d}\Delta \boldsymbol{x}_\mathrm{s}}{\mathrm{d}t} \\ \frac{\mathrm{d}\Delta \tau_\mathrm{ref}}{\mathrm{d}t} \\ \frac{\mathrm{d}\Delta \omega_\mathrm{m}}{\mathrm{d}t} \end{bmatrix} = \underbrace{\begin{bmatrix} \boldsymbol{A}_\mathrm{s} & \boldsymbol{0}_{(m+7),1} & \boldsymbol{b}_{\mathrm{s}\omega} \\ \alpha_\mathrm{f} \boldsymbol{a}_\delta & -\alpha_\mathrm{f} & 0 \\ p J_\mathrm{m}^{-1} \boldsymbol{a}_\omega & 0 & 0 \end{bmatrix}}_{\boldsymbol{A}_\mathrm{M}} \underbrace{\begin{bmatrix} \Delta \boldsymbol{x}_\mathrm{s} \\ \Delta \tau_\mathrm{ref} \\ \Delta \omega_\mathrm{m} \end{bmatrix}}_{\Delta \boldsymbol{x}_\mathrm{T}} + \underbrace{\begin{bmatrix} \boldsymbol{b}_{\mathrm{s}\omega,\mathrm{ref}} \\ 0 \\ 0 \end{bmatrix}}_{\boldsymbol{b}_\mathrm{M}} \Delta \omega_\mathrm{c} + \\ + \underbrace{\begin{bmatrix} \boldsymbol{B}_\psi \\ \boldsymbol{0}_{1,2} \\ \boldsymbol{0}_{1,2} \end{bmatrix}}_{\boldsymbol{B}_\psi} \Delta \boldsymbol{\psi}_\mathrm{c,ref} + \underbrace{\begin{bmatrix} \boldsymbol{0}_{(m+7),1} \\ 0 \\ -p J_\mathrm{m}^{-1} \end{bmatrix}}_{\boldsymbol{b}_\tau} \Delta \tau_\mathrm{L} \tag{51}$$

where $\Delta \boldsymbol{x}_\mathrm{T} = [\Delta \boldsymbol{i}_\mathrm{c}^\mathrm{T}, \Delta \boldsymbol{u}_\mathrm{s}^\mathrm{T}, \Delta \boldsymbol{\psi}_\mathrm{c}^\mathrm{T}, \Delta\delta, \Delta \tilde{\boldsymbol{\psi}}_\mathrm{c}^\mathrm{T}, \Delta\tilde{\delta}, \Delta\tau_\mathrm{ref}, \Delta\omega_\mathrm{m}]^\mathrm{T}$ is the state vector of the overall system with the reduced-order observer when considering LPF and mechanical dynamics. Vector $\boldsymbol{a}_\delta = \frac{3p}{2}[\boldsymbol{c}_\tau^\mathrm{T}, -\boldsymbol{i}_{\mathrm{s}0}^\mathrm{T}\mathbf{J}, 0]$ is used in the LPF dynamics expression (40) and vector $\boldsymbol{a}_\omega = \frac{3p}{2}[\boldsymbol{c}_\tau^\mathrm{T}, \boldsymbol{0}_{1,2}, 0]$ is used in the mechanical dynamics expression (46b). It is worth noticing that the output equation for electromagnetic torque in (37) is implemented in the last row of the system matrix $\boldsymbol{A}_\mathrm{M}$.

Alternatively, the full-order observer has the state vector $\Delta \boldsymbol{x}_\mathrm{T} = [\Delta \boldsymbol{i}_\mathrm{c}^\mathrm{T}, \Delta \boldsymbol{u}_\mathrm{s}^\mathrm{T}, \Delta \boldsymbol{\psi}_\mathrm{c}^\mathrm{T}, \Delta\delta, \Delta \tilde{\boldsymbol{i}}_\mathrm{c}^\mathrm{T}, \Delta \tilde{\boldsymbol{u}}_\mathrm{s}^\mathrm{T}, \Delta \tilde{\boldsymbol{\psi}}_\mathrm{c}^\mathrm{T}, \Delta\tilde{\delta}, \Delta\tau_\mathrm{ref}, \Delta\omega_\mathrm{m}]^\mathrm{T}$, vectors $\boldsymbol{a}_\delta = \frac{3p}{2}[\boldsymbol{c}_\tau^\mathrm{T}, \boldsymbol{i}_{\mathrm{s}0}^\mathrm{T}\mathbf{J}L_\mathrm{f}, \boldsymbol{0}_{1,2}, -\boldsymbol{i}_{\mathrm{s}0}^\mathrm{T}\mathbf{J}, 0]$ and $\boldsymbol{a}_\omega = \frac{3p}{2}[\boldsymbol{c}_\tau^\mathrm{T}, \boldsymbol{0}_{1,2}, \boldsymbol{0}_{1,2}, \boldsymbol{0}_{1,2}, 0]$. The difference between the reduced-order and full-order observer vectors is that corresponding zero sub-vectors $\boldsymbol{0}_{1,2}$ disappear from the vectors $\boldsymbol{a}_\delta$ and $\boldsymbol{a}_\omega$, because the states $\Delta\tilde{\boldsymbol{i}}_\mathrm{c}$ and $\Delta\tilde{\boldsymbol{u}}_\mathrm{s}$ are absent in the reduced-order observer. Additionally, $\boldsymbol{a}_\delta$ in the full-order observer includes $\boldsymbol{i}_{\mathrm{s}0}^\mathrm{T}\mathbf{J}L_\mathrm{f}\Delta\tilde{\boldsymbol{i}}_\mathrm{c}$, which results from (41).

Furthermore, linearized synchronous angular speed from (44) is expressed as

$$\Delta\omega_\mathrm{c} = \Delta\omega_\mathrm{m,ref} + \underbrace{\begin{bmatrix} -g_\tau \boldsymbol{a}_\delta & g_\tau & 0 \end{bmatrix}}_{\boldsymbol{k}_\sigma^\mathrm{T}} \Delta \boldsymbol{x}_\mathrm{T} \tag{52}$$

which can be further substituted to (51). Therefore, the final closed-loop system can be expressed as

$$\frac{\mathrm{d}\Delta \boldsymbol{x}_\mathrm{T}}{\mathrm{d}t} = \underbrace{(\boldsymbol{A}_\mathrm{M} + \boldsymbol{b}_\mathrm{M}\boldsymbol{k}_\sigma^\mathrm{T})}_{\boldsymbol{A}_\mathrm{T}} \Delta \boldsymbol{x}_\mathrm{T} + \boldsymbol{b}_\mathrm{M}\Delta\omega_\mathrm{m,ref} + \boldsymbol{B}_\psi \Delta \boldsymbol{\psi}_\mathrm{c,ref} + \boldsymbol{b}_\tau \Delta\tau_\mathrm{L} \tag{53}$$

where $\boldsymbol{A}_\mathrm{T}$ is a system matrix of the resulting overall system. Eigenvalues of $\boldsymbol{A}_\mathrm{T}$ symbolize poles of the system.

The system stability can be checked by illustrating the root loci of dominating poles. The system is stable if all the poles are located in the left-half plane, meaning that imaginary parts of poles are negative. The system can be marginally stable if any of poles are located on the imaginary axis. The system is unstable if the poles are on the right-half plane.

5 Results

5.1 Small-signal linearization

5.1.1 Root loci of dominating poles

Let us first consider state space representation derived in (51) without substitution of the input $\Delta\omega_c$ in (52). Therefore, the eigenvalues of $\boldsymbol{A}_M$ represent the poles of the overall system. Figure 21 shows the root loci for V/Hz control with the reduced-order observer. In this example, operating point load torque is set to zero, and ω_{c0} is changed (0 - 2 p.u.). Default parameter and control gain settings are considered (Appendix A). Root loci of dominating poles for the control with full-order observer are found in Figure 22.

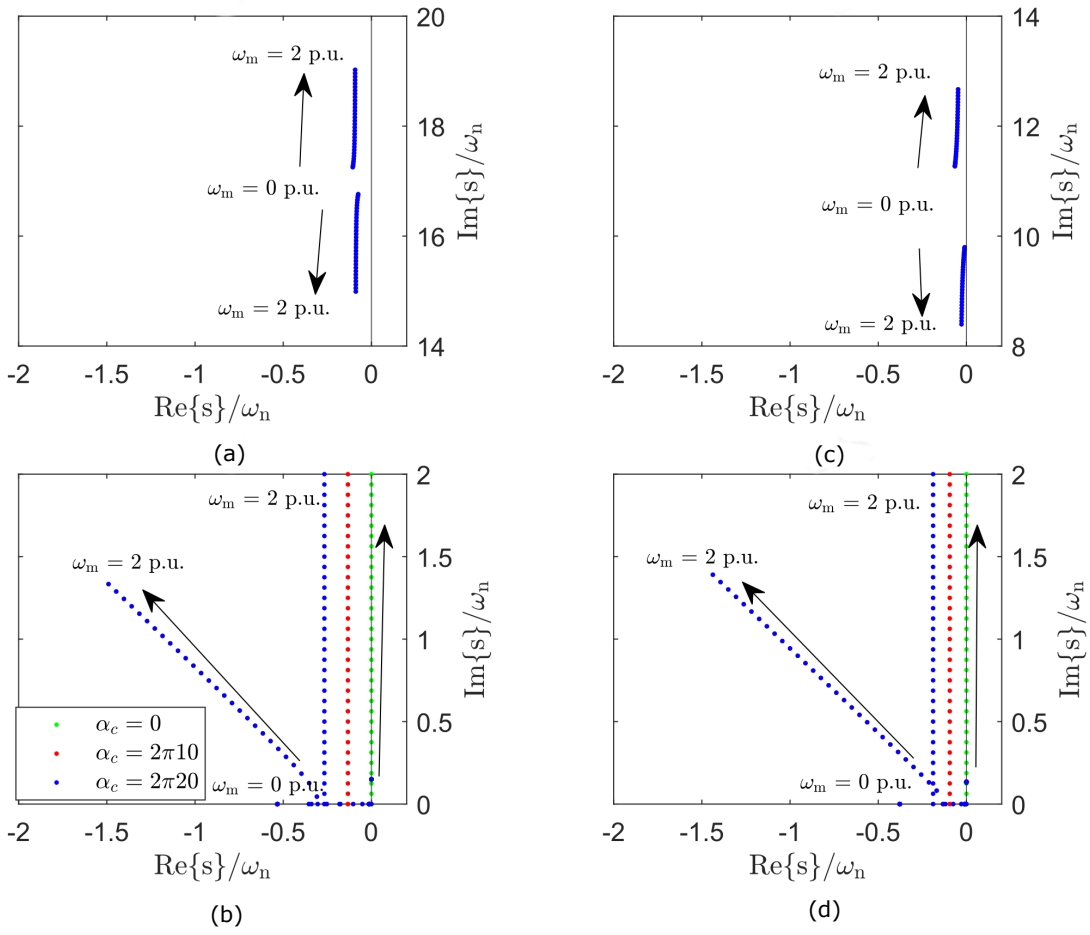

Figure 21: Root loci of dominating poles for the SM control with the reduced-order observer: (a) High-frequency poles of the PMSM with the LC filter; (b) Low-frequency poles of the PMSM with the LC filter; (c) High-frequency poles of the SyRM with the LC filter; (d) Low-frequency poles of the SyRM with the LC filter.

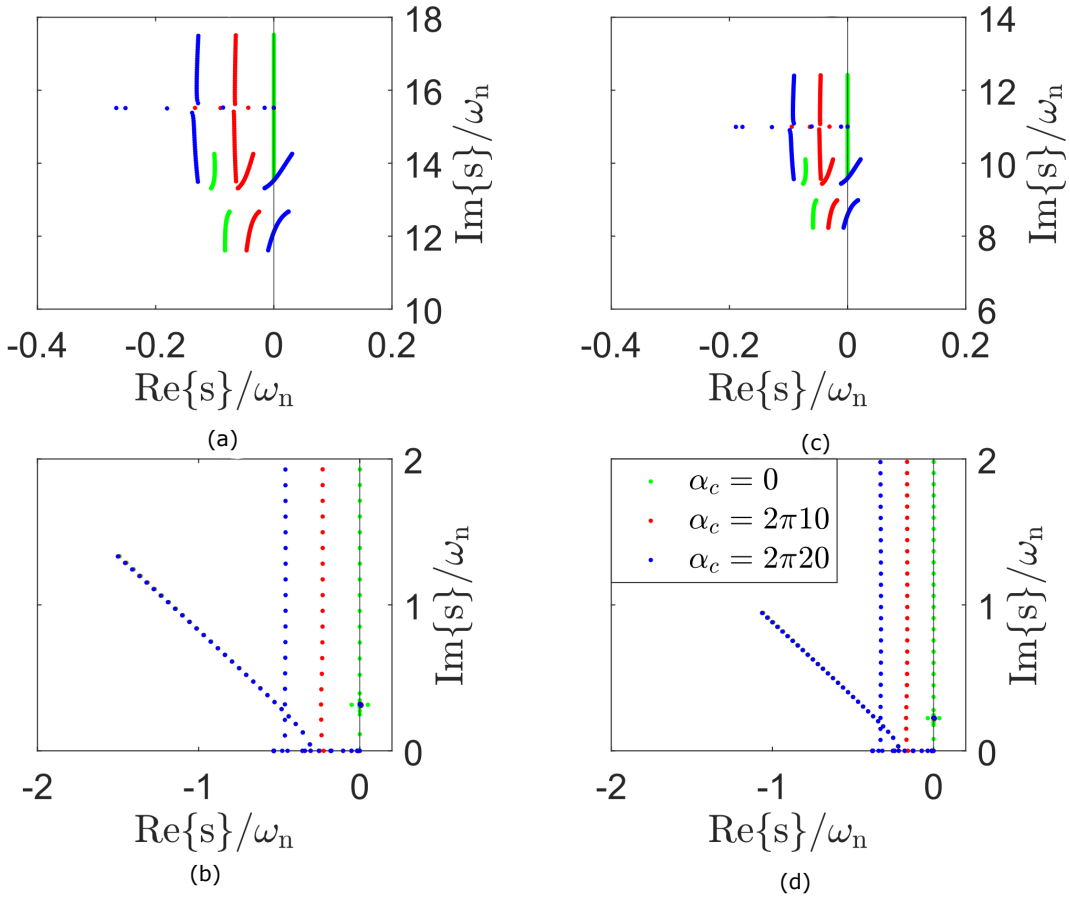

Figure 22: Root loci of dominating poles for the SM control with the full-order observer: (a) High-frequency poles of the PMSM with the LC filter; (b) Low-frequency poles of the PMSM with the LC filter; (c) High-frequency poles of the SyRM with the LC filter; (d) Low-frequency poles of the SyRM with the LC filter.

It can be shown that high-frequency poles originate from the LC filter dynamics, and they are not present in SM drives without the LC filter [14]. Furthermore, low-frequency control poles originating from the state feedback controller are parallel with the imaginary axis. With the higher controller gain α_c, the further away poles move from the y-axis. However, in the full-order observer case (Figure 22), the increase of α_c has an adverse effect on the stability. Conversely, control poles are closer to the y-axis with lower α_c. Therefore, the gain $\alpha_c = 2\pi 10$ rad/s from Appendix A is feasible from the stability perspective according to root loci in Figure 22.

Additionally, the damping ratio $\zeta_\infty = 0.7$ locates the observer poles with 45° angle as expected in [14]. However, the system analysis based on the small-signal linearized model in CT is not further discussed in this thesis due to existing problems described in the next section.

5.1.2 Shortages of the developed linearized model

The system stability was initially studied by plotting eigenvalues of the overall system matrix $\boldsymbol{A}_{\mathrm{T}}$ derived in (53) instead of $\boldsymbol{A}_{\mathrm{M}}$. However, the eigenvalues of $\boldsymbol{A}_{\mathrm{T}}$ showed that the system was unstable for both motor types with any of the selected control methods (Figures 19 and 20), thus leading to incorrect assumptions that the overall system is unstable in the following development stages (simulations and experiments).

Furthermore, it was originally expected that the CT model would predict the behavior of the DT model. However, it was later shown that the linearized CT model is inaccurate due to the DT delays as discussed in Section 2.2.3. Because of this inaccuracy, the root loci of the CT model does not match with the DT model loci. Therefore, the presented root loci of dominating poles for $\boldsymbol{A}_{\mathrm{M}}$ only serve as an illustration showing existence of high-frequency poles as well as the low-frequency poles originating from the observer and the state feedback. Moreover, the overall system stability cannot be discussed based on the obtained root loci. Additionally, it is tedious to compare pole locations numerically with the resulting transfer function of the system because its denominator includes high-order terms due to inclusion of the LC filter in the system.

To demonstrate the instability of the linearized CT model, the sampling period T_{s} was reduced to simulate the control in CT. Figure 23 shows the effect of reduced T_{s} on $\boldsymbol{\psi}_{\mathrm{c}}$. The flux oscillates around the reference point with a slow increase in its amplitude. As a result, this leads to the unstable operation of the SyRM. The flux was constant when the same simulation test was repeated for the PMSM, meaning the stability was satisfied.

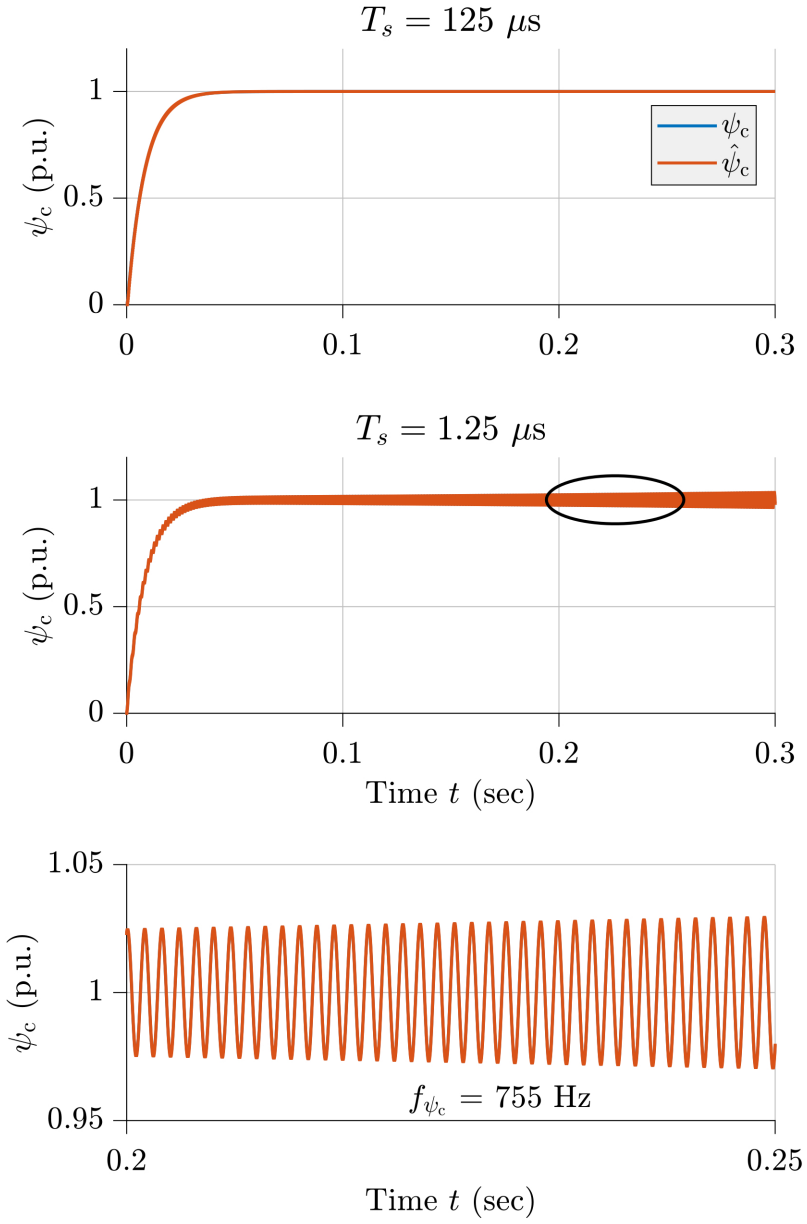

Figure 23: Effect of the sampling period on $\hat{\boldsymbol{\psi}}_c$ (SyRM, full-order observer).

5.2 Simulations

5.2.1 Proposed control methods

Simulation models are developed in MATLAB/Simulink for controlling 2.2 kW PMSM and 6.7 kW SyRM, which are also used for the experiments. However, if the motor and filter parameters are known, the simulation models are universal for any SM with an LC filter. The motor and LC filter specifications and the control parameters are found in Appendix A. The control and plant model parameters used in the simulations are constant and equal.

The thesis does not discuss reference speeds above the rated speed, i.e., operation in the field-weakening region. The speed reference is ramped from 0 to 1 p.u. with a specific rate, which depends on the motor type. The SyRM needs longer acceleration and deceleration times because the load angle can reach its threshold limit due to the high saliency of the machine.

Simulation results for the PMSM with the LC filter (Figure 24 and 25) are almost identical for both control methods. The only major difference is in the higher converter current ripple when using the reduced-order observer (Figure 24) in comparison with the (Figure 25). Based on the simulations, both control methods can be used in medium-performance PMSM drives with LC filters loaded by passive and active loads.

Simulation results for the SyRM with the LC filter are shown in Figure 26 for the full-order observer. This control method is suitable for medium-performance drives based on the simulation results. However, the simulation for the SyRM with the reduced-order observer showed that the system was unstable. The currents $\boldsymbol{i}_{\mathrm{c}}$ and $\boldsymbol{i}_{\mathrm{s}}$ start oscillating at steady-state to immeasurably high values. Nevertheless, the control was stable when the same control model was used for the PMSM (Figure 24).

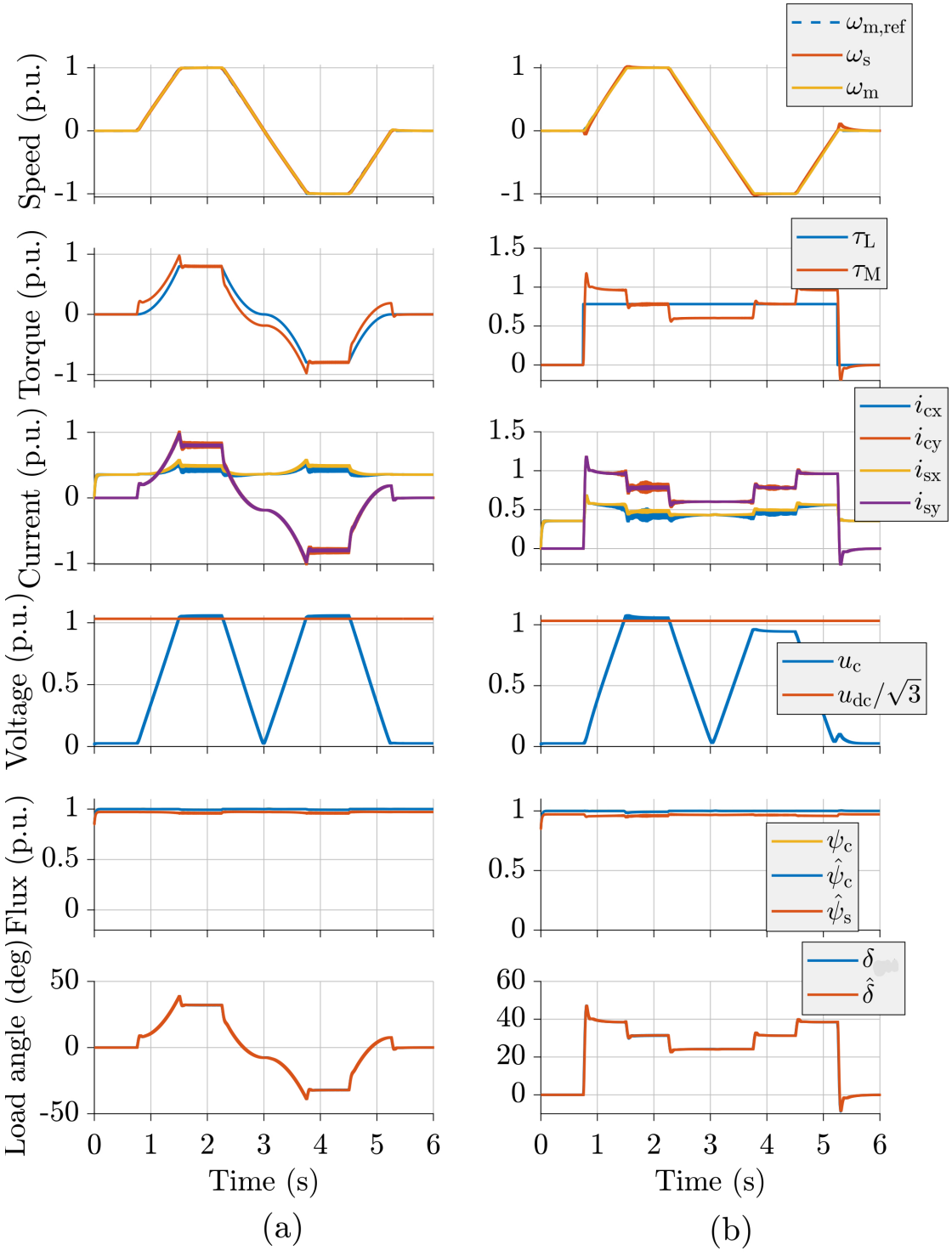

Figure 24: Simulation results of the observer-based V/Hz control (reduced-order observer) for the PMSM with the LC filter. The speed reference is ramped: $0 \rightarrow 1$ p.u. in $t = 0.75$ s. The load sequences are (a) quadratic load from zero to its rated value and (b) load step starts at $t = 0.75$ s and stops at $t = 5.25$ s.

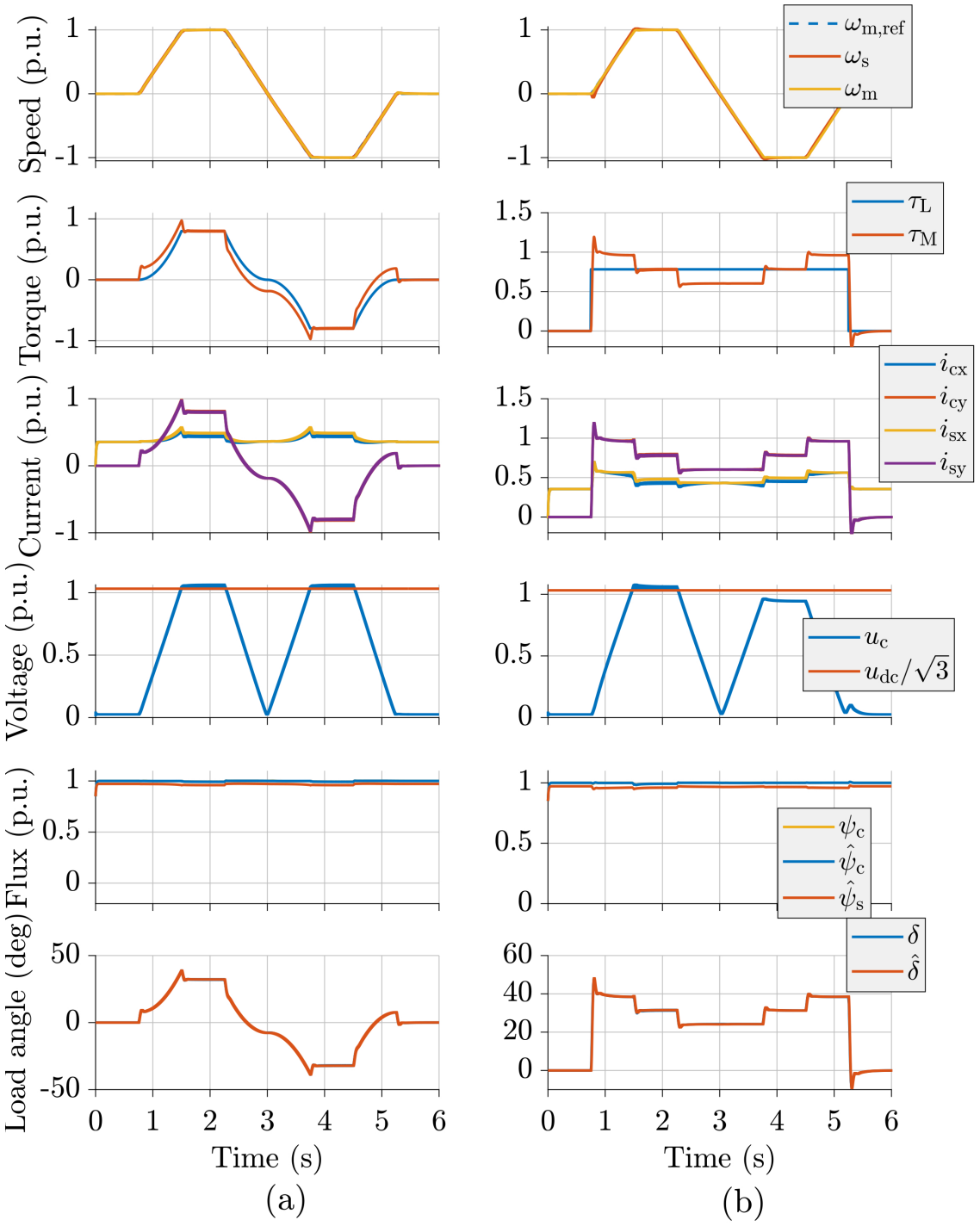

Figure 25: Simulation results of the observer-based V/Hz control (full-order observer) for the PMSM with the LC filter. The speed reference is ramped: $0 \rightarrow 1$ p.u. in $t = 0.75$ s. The load sequences are (a) quadratic load from zero to its rated value and (b) load step starts at $t = 0.75$ s and stops at $t = 5.25$ s.

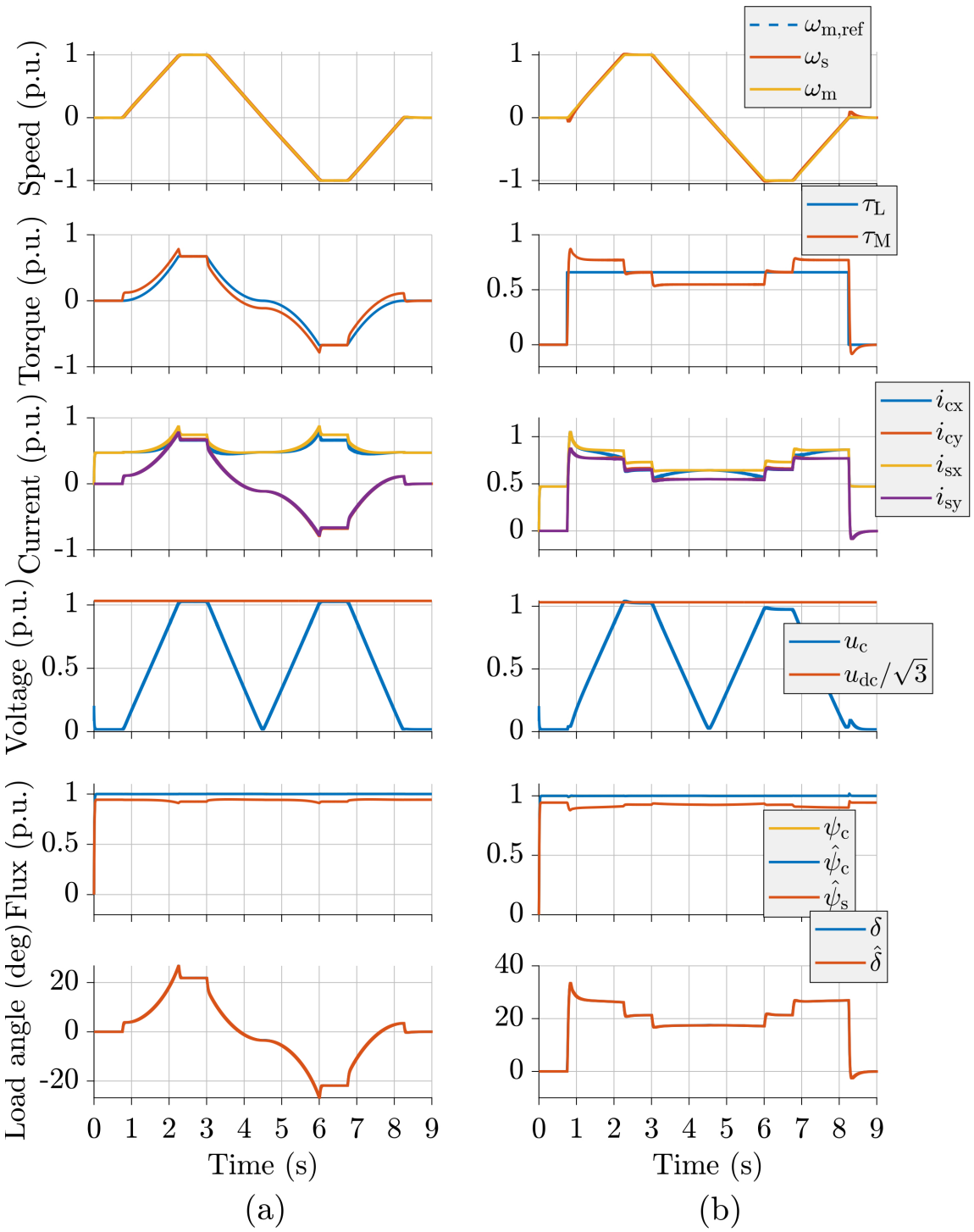

Figure 26: Simulation results of the observer-based V/Hz control (full-order observer) for the SyRM with the LC filter. The speed reference is ramped: $0 \rightarrow 1$ p.u. in $t = 1.5$ s. The load sequences are (a) quadratic load from zero to its rated value and (b) load step starts at $t = 0.75$ s and stops at $t = 8.25$ s.

5.2.2 Parameter sensitivity

Simulation results in Section 5.2 show an ideal case in which the motor parameters are constant and equal for the plant model as well as for the control model. However, in a real scenario, the motor characteristics are non-linear. Therefore, a difference exists between the constant control and the motor parameters, degrading the machine dynamic performance. For this reason, parameter sensitivity can be examined before the measurements to unveil possible problems in the lab and to tune the control parameters accordingly.

Stator d-axis inductance L_d

In practice, the inductance L_d can be lower than its datasheet value due to the magnetic saturation. Additionally, manufacturing defects cause a deviation of L_d. The datasheet L_d value typically refers to the rated operating current condition. With a higher operating current, the inductance L_d heavily drops after reaching the flux linkage saturation point. As a result, the mismatch between L_d and $\hat{L}_\mathrm{d}$ causes additional torque oscillations at zero speeds and in steady-state.

Damping constant g_τ should be carefully chosen. A too low value of g_τ results in insufficient damping of electromagnetic torque oscillations. The torque oscillations are eliminated in the simulated scenario (Figure 27), in which $g_\tau = 3\ \mathrm{N^{-1}m^{-1}rad{\cdot}s^{-1}}$.

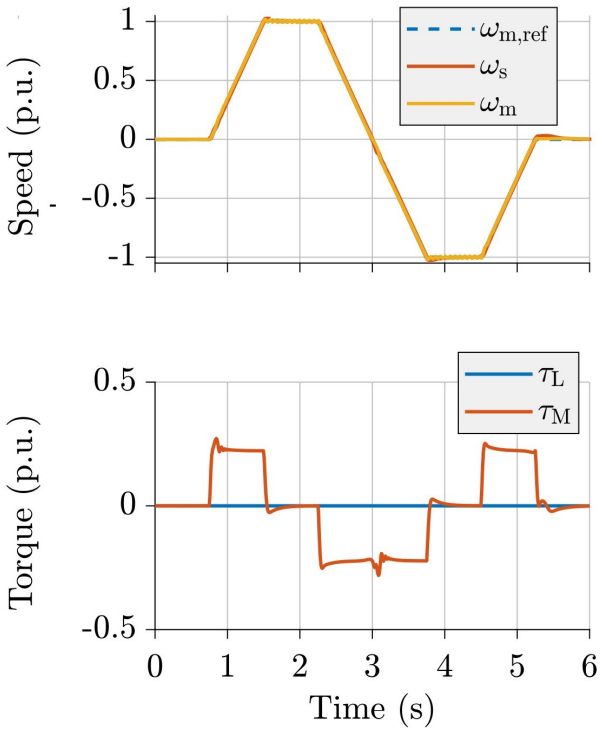

Figure 27: L_d sensitivity for the SyRM with the LC filter at no load: a d-inductances ratio $\hat{L}_\mathrm{d}/L_\mathrm{d} = 0.8$ and the HPF damping constant $g_\tau = 3\ \mathrm{N^{-1}m^{-1}rad{\cdot}s^{-1}}$.

Stator resistance R_s

The filter resistance R_f is neglected, and R_s is assumed to be constant in the simulation model. However, real resistances are temperature-dependent and therefore non-linear. For this reason, the resulting $\hat{R}_s$ is a sum of the temperature-dependent R_s and R_f.

Figure 28 shows an effect of R_s sensitivity on $\boldsymbol{\psi}_c$. Control stator resistance $\hat{R}_s$ was increased by 15%.

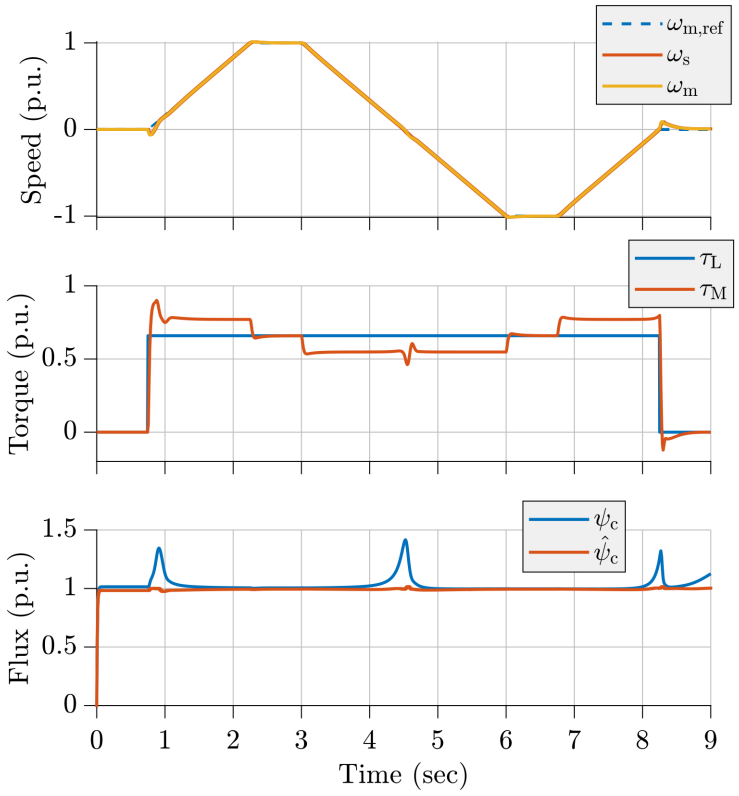

Figure 28: R_s sensitivity for the SyRM with the LC filter at no load: a stator resistance ratio $\hat{R}_s/R_s = 1.15$ with HPF damping constant $g_\tau = 3$ $\mathrm{N^{-1}m^{-1}rads^{-1}}$.

It can be noticed that $\frac{\mathrm{d}\boldsymbol{\psi}_c}{\mathrm{d}t}$ is high at zero speeds. At zero speed in steady-state (simulation time 8.25-9 sec.), $\boldsymbol{\psi}_c$ will increase with a lower rate. If the simulation continues, $\boldsymbol{\psi}_c$ keeps increasing until the simulation breaks. A non-zero $\frac{\mathrm{d}\boldsymbol{\psi}_c}{\mathrm{d}t}$ at zero speed can be explained by inserting a control law with $\hat{R}_s$ (Section 3.2.1) to (16). Additionally, equation (31a) shows that $\boldsymbol{i}_{s0}$ depends on $\boldsymbol{L}_s$ and L_f at zero speed.

In reality, however, magnetic flux is non-linear and saturates after reaching a certain point. As mentioned earlier, the non-linear behavior of $\boldsymbol{\psi}_s$ causes a higher current to be needed after crossing the saturation point. Therefore, the operation is interrupted by over-current protection in the physical SM drive.

Filter capacitance C_f and inductance L_f

The physical filter capacitance C_f and inductance L_f deviate due to manufacturing defects. Moreover, the capacitor degrades its capacitance by aging, and L_f is not constant due to the non-linear behavior of the magnetic flux. Therefore, it is needed to check capacitance and inductance sensitivities by varying control filter parameters. The parameter sensitivity of the filter is done separately for each parameter ($\hat{C}_\mathrm{f}$ or $\hat{L}_\mathrm{f}$).

Based on the simulations, the ratios $\hat{C}_\mathrm{f}/C_\mathrm{f} = 0.92$ and $\hat{L}_\mathrm{f}/L_\mathrm{f} = 0.87$ for the PMSM, as well as $\hat{C}_\mathrm{f}/C_\mathrm{f} = 0.94$ and $\hat{L}_\mathrm{f}/L_\mathrm{f} = 0.85$ for the SyRM cause unstable operation when only $\boldsymbol{i}_\mathrm{s}$ is measured with the gain settings in Appendix A and the load step. It is worth mentioning that the simulated results are not affected before reaching the threshold ratios ($\hat{C}_\mathrm{f}/C_\mathrm{f}$ and $\hat{L}_\mathrm{f}/L_\mathrm{f}$). However, the sensitivity of the filter capacitance and inductance can be significantly improved by increasing the LC filter damping constant ($g = 0.5$ by default). Nevertheless, a method with both $\boldsymbol{i}_\mathrm{s}$ and $\boldsymbol{i}_\mathrm{c}$ current measurement lead to a versatile selection of $\hat{C}_\mathrm{f}$ and $\hat{L}_\mathrm{f}$, and the control works even with $\hat{C}_\mathrm{f} = 0$ and $\hat{L}_\mathrm{f} = 0$.

5.3 Experiments

5.3.1 Experimental drive setup

Figure 29 shows an overview of the experimental setup used in the thesis. The investigated motor (PMSM or SyRM) is connected to the LC filter output terminals. Each motor has a different LC filter, whose specifications can be found in Appendix A. A PM servo motor loads the investigated motor with a load torque given by a user. The PM servo and the tested motors are driven by the frequency converters ABB ACS880.

The frequency converters share a common DC bus meaning that both buses are connected in parallel. The purpose of the braking resistor is to dissipate kinetic energy of the rotor coming to the DC bus when the motor is braking. Therefore, the voltage in the DC bus increases, thus leading to possible capacitor breakdown.

MicroLabBox is a development system with multiple input and output channels, suitable for motor control laboratory setups. MicroLabBox processes the analog data such as measured voltages, phase currents, and speed. Light-colored signals (ω_m and u_LL) in Figure 29 are only used for monitoring and not in the feedback control. MicroLabBox also conveys PWM, braking and other control signals to the frequency converter. The sampling frequency of 8 kHz is used, double the switching frequency (4 kHz).

A user sends from a computer input commands, and the computer displays desired variables. The developed control methods were programmed in MATLAB Simulink software. The Simulink file is then converted into a dSPACE-supported file (.sdf). The software dSPACE ControlDesk is used for controlling and monitoring the tested motor. The monitored data can be exported to a MATLAB-supported file (.mat).

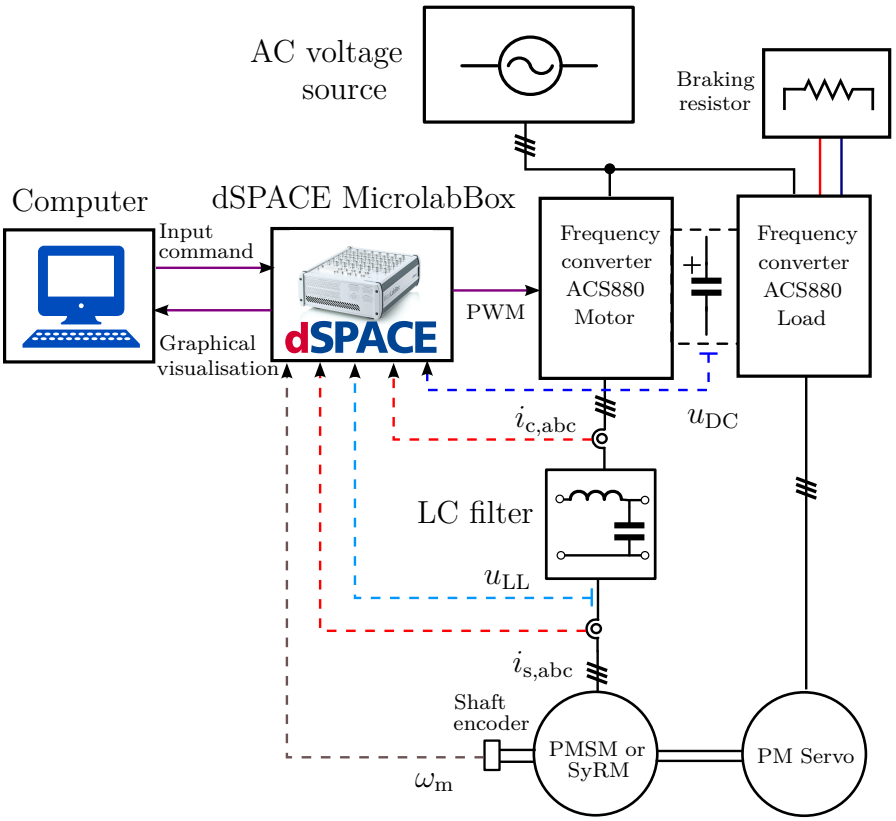

Figure 29: Experimental drive setup.

5.3.2 Obtained measurement results

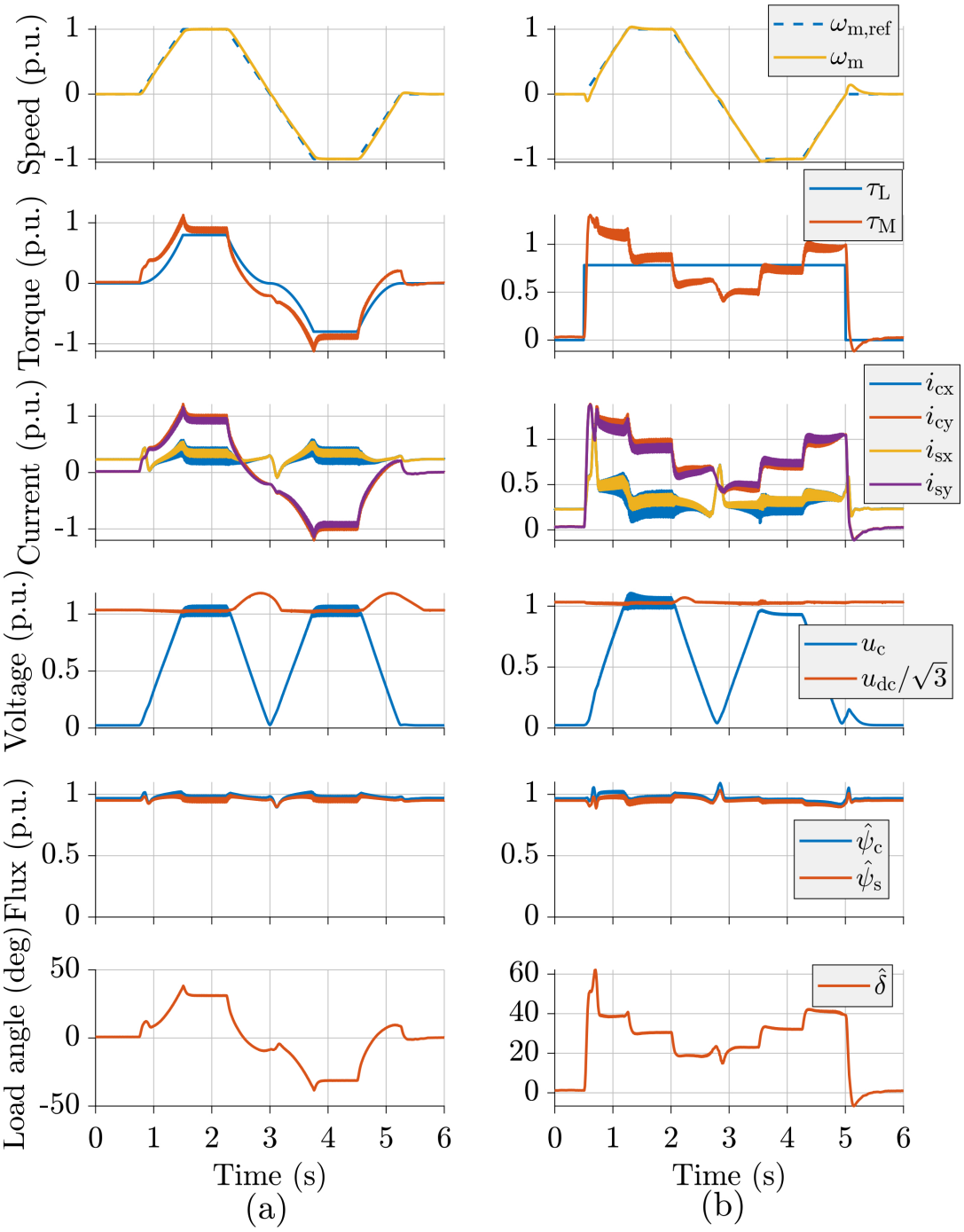

Figure 30: Experimental results of the observer-based V/Hz control (reduced-order observer) for the PMSM with the LC filter. The speed reference is ramped: $0 \rightarrow 1$ p.u. in $t = 0.75$ s. The load sequences are (a) quadratic load from zero to its rated value and (b) load step starts at $t = 0.75$ s and stops at $t = 5.25$ s.

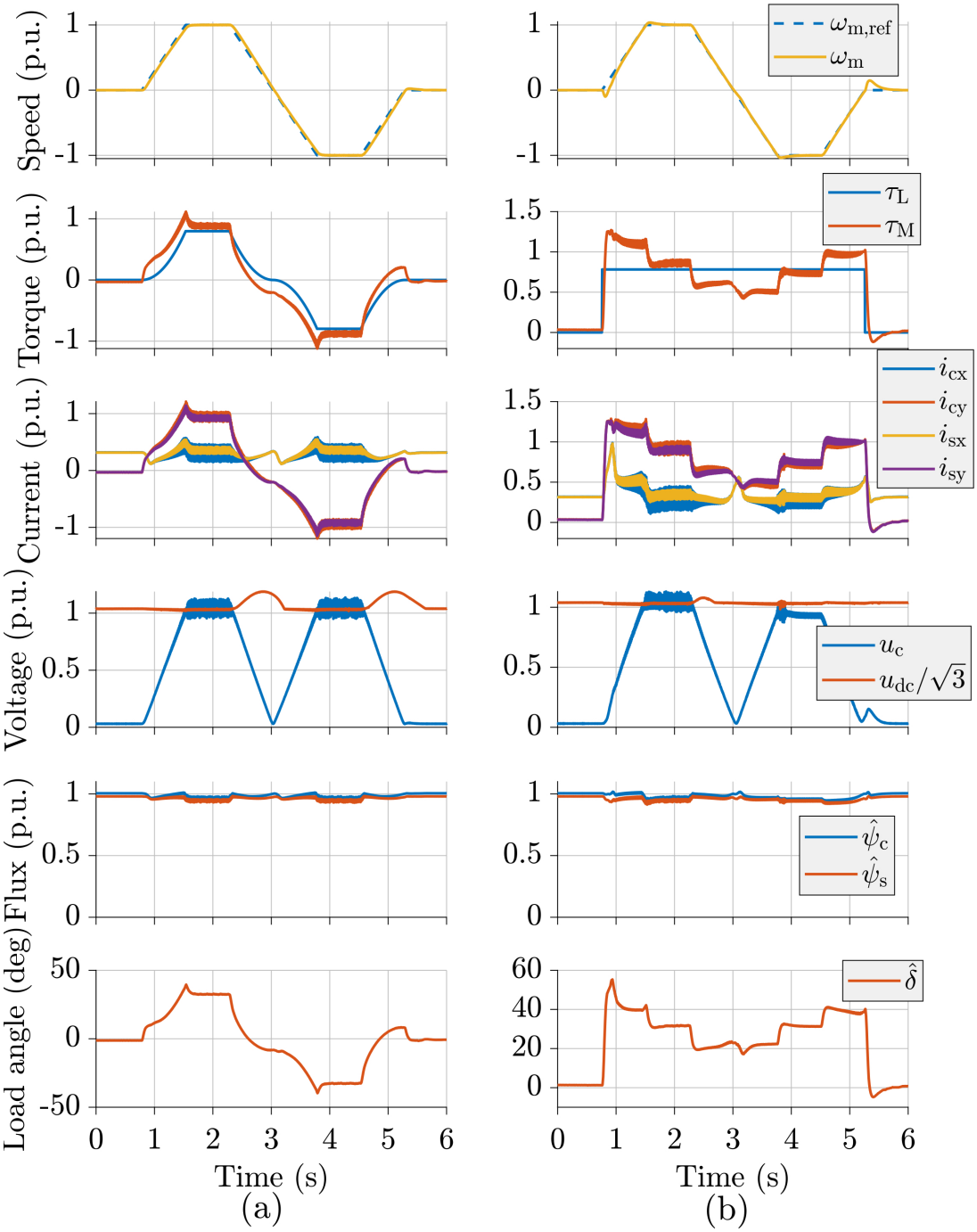

Figure 31: Experimental results of the observer-based V/Hz control (full-order observer) for the PMSM with the LC filter. The speed reference is ramped: $0 \rightarrow 1$ p.u. in $t = 0.75$ s. The load sequences are (a) quadratic load from zero to its rated value and (b) load step starts at $t = 0.75$ s and stops at $t = 5.25$ s.

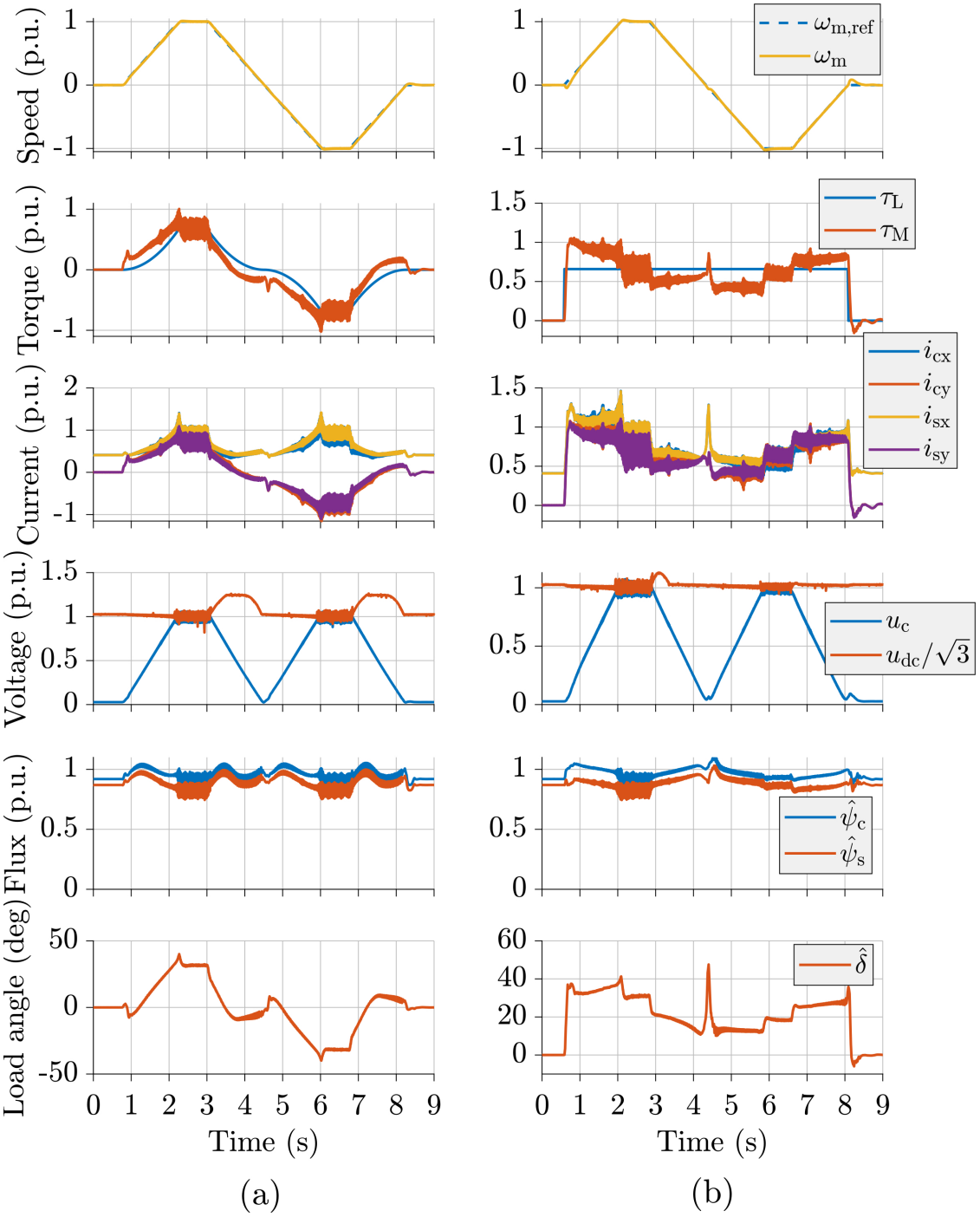

Figure 32: Experimental results of the observer-based V/Hz control (reduced-order observer) for the SyRM with the LC filter. The speed reference is ramped: $0 \rightarrow 1$ p.u. in $t = 1.5$ s. The load sequences are (a) quadratic load from zero to its rated value and (b) load step starts at $t = 0.75$ s and stops at $t = 8.25$ s.

Several differences exist by comparing experimental results with the corresponding simulation results. As mentioned in Section 5.2.2, the parameters of the physical motor and filter differ from datasheet parameters due to its non-linearities, manufacturing defects, and material aging. Moreover, R_f, the friction of the bearings, the effect of dead-time, and other non-linearities are neglected in the simulations. Nevertheless, is was shown that the simulations are a good approximation of the measurements in almost all cases.

It was shown through the simulations that the observer-based V/Hz control is sensitive to the error of R_s. For the reason of non-zero R_f, $\hat{R}_\mathrm{s}$ was adjusted to $\hat{R}_\mathrm{s} = 4.1\ \Omega$ ($\hat{R}_\mathrm{s}/R_\mathrm{s} = 1.14$) for the PMSM and $\hat{R}_\mathrm{s} = 0.67\ \Omega$ ($\hat{R}_\mathrm{s}/R_\mathrm{s} = 1.24$) for the SyRM. To keep the experimental measurements simple, other parameter settings are set as default because the heuristic tuning requires a lot of time. It is therefore recommended to use or develop automatic identification methods for SM drives with the LC filter. For example, signal injection-based methods similar to [42], developed for the PMSM with the LC filter.

PMSM

Figure 30 shows experimental results of reduced-order observer V/Hz control for the PMSM with the LC filter. Let us compare the experimental results with the corresponding simulation results (Figure 24). Similar findings also hold when comparing experimental and simulations results for full-order observer V/Hz control (Figure 31 and Figure 25).

First, τ_m is higher in the experiments due to the friction drag of the bearings, which is omitted in the simulations. Additionally, the peak load angle is considerably higher for a load step sequence because of a mismatch between R_s and $\hat{R}_\mathrm{s}$, as well as inverter nonlinearities. Second, $\boldsymbol{\psi}_\mathrm{c}$ increases and then drops at the time instants when the speed is zero. The x-axis current also increases and decreases, so the machine draws more current than needed and demagnetizes itself. The problem causes inaccurate estimation of $\hat{R}_\mathrm{s}$ (see Figure 28) in combination with inaccurate filter parameters $\hat{C}_\mathrm{f}$ and $\hat{L}_\mathrm{f}$. Third, the DC bus voltage of the real converter is not constant; u_DC increases when the motor is braking. Last, $\boldsymbol{i}_\mathrm{c}$ and $\boldsymbol{i}_\mathrm{s}$ have higher ripple in the measurements, caused when converter voltage reference is higher than the maximum available voltage ($u_\mathrm{DC}/\sqrt{3}$) and also by inaccurate parameter estimates. The current and torque ripples can be reduced by lowering $\boldsymbol{\psi}_\mathrm{c,ref}$ at speeds close to the rated speed, so the $\boldsymbol{u}_\mathrm{c,ref}$ is below $u_\mathrm{DC}/\sqrt{3}$. However, the reduced flux introduces lower maximum torque capability. The effect of lower $\boldsymbol{u}_\mathrm{c,ref}$ on the current or torque ripple can be seen from Figures 30(b) and 31(b) when comparing the ripple in the positive with the negative direction of $\omega_\mathrm{m,ref}$.

By comparing the experimental results, i.e., Figure 30 and Figure 31, x-axis current spikes at zero speed instants are higher for the reduced-order observer. The undesired demagnetization at the zero speeds and the peak load angle are lower for the full-order observer. Additionally, $\boldsymbol{u}_\mathrm{c,ref}$ at steady state has a higher ripple for the full-order observer, meaning that the current and torque ripples are also higher.

SyRM

The main disadvantages of SyRMs are high torque ripple and poor power factor due to the saliency and high leakage inductances [43]. The high saliency makes the SyRM difficult to control and find an accurate rotor position. The initial rotor position is set to align the d-axis of the rotor with the α-axis of the stator by adding a simple 2-degree-of-freedom PI current controller from [44], whereas, in the PMSM, the rotor position alignment was unrequired. Additionally, the speed rate limit of the SyRM is decreased compared to the PMSM because of existing difficulties with high current spikes at the load step.

Experimental results for the reduced-order observer are shown in Figure 32. These results cannot be compared with the corresponding simulation results because the simulations indicated that the system is unstable.

The SyRM was unstable in the experiments for the full-order observer. In other words, the SyRM could not run, and the overcurrent protection tripped at zero speeds in the first attempts. Therefore, it was attempted to change other control parameters such that the machine would run ($g = 0.25$, $\hat{R}_\mathrm{s} = 0.66\ \Omega$, $\hat{C}_\mathrm{f} = 11\ \mu$F, $\hat{L}_\mathrm{f} = 2.5$ mH and $\zeta_\infty = 0.85$). The machine only ran at no load after these changes. Therefore, the results of the loaded SyRM with the LC filter for the full-order observer are not included in this thesis.

Overall, the performance of the SyRM with the LC filter has shortages. The torque waveform for the SyRM has a higher ripple than for the PMSM, which is also accompanied by higher noise and vibrations. Moreover, $\hat{\delta}$ has a reversed sign at low speeds for the quadratic load sequence in Figure 32(a) and a high $\hat{\delta}$ spike at zero speed in the middle of the simulation for the load step. Additionally, u_DC is oscillating together with $\boldsymbol{u}_\mathrm{c,ref}$ when the voltage reference reaches its maximum available voltage limit ($u_\mathrm{DC}/\sqrt{3}$). Similarly, as in the PMSM, the ripples can be minimized by limiting $\boldsymbol{u}_\mathrm{c,ref}$ at the rated speed by reducing $\boldsymbol{\psi}_\mathrm{c,ref}$.

6 Conclusions

The thesis aimed to develop the observer-based V/Hz control for SM drives with LC filters. This was achieved by employing LC filter dynamics to the recently developed observer-based V/Hz control [14]. Consequently, two control strategies were developed: (a) with the reduced-order observer (stator and converter currents are measured) and (b) with the full-order observer (stator currents are measured and converter currents are estimated).

The literature review shows that state-of-the-art sensorless control methods are infeasible for medium-performance plug-and-play AC motor drives. The reason is that the methods either contain several cascaded control loops, require cumbersome parameter tuning, are sensitive to parameter errors, or have a limited operating speed range. On the contrary, the observer-based V/Hz control showed compelling attributes, such as relatively low sensitivity to parameter errors, simple and general control structure, and common control gains for all SM types. These attributes indicate that the observer-based V/Hz control can be implemented on medium-performance drives ensuring robust and stable operation at a wide range of speeds.

The linearized continuous-time model was initially developed to examine the system stability. However, it was revealed that the linearized continuous-time model is inaccurate because it does not include the effects of the discrete-time delays. Therefore, the developed linearized continuous-time model introduces unstable regions, which are absent in the simulations with the discretized controller.

The next step was to build simulation models where discrete-time delays were considered. The simulations worked for almost all the examined cases, except for the SyRM with the reduced-order observer. Unfortunately, the reason causing this problem was not identified.

Parameter sensitivity of the control system was examined by means of simulations. For example, the mismatch between real and estimated stator d-inductances could cause undesired torque oscillations at zero speeds. Furthermore, estimated values of the stator and filter resistances lower than their actual values could interrupt the motor operation at low speeds due to overcurrents. The control was less sensitive to the filter parameter errors when the measured converter and stator currents were used in the controller. However, the control is more sensitive when one of the currents was estimated. The parameter sensitivity could be lowered by increasing the LC filter damping gain.

Experimental measurements validated the control performance. The measurements were successfully performed for the PMSM with both control methods. However, the measurements could not be taken for the loaded SyRM with the full-order observer. The SyRM could only run without the load after changing control parameters and decreasing the LC filter damping gain. The SyRM unstable operation could be caused by the inaccurate selection of the control parameters or an unsuitable observer for the SyRM. The filter resistance could not be neglected, as expected from the parameter sensitivity simulations. As a result, the estimated stator resistance was increased to include the non-zero filter resistance. Moreover, the control parameters were not ideally tuned in all cases, and the current ripple was considerably high when

the voltage reference exceeded the maximum available voltage limit.

The proposed methods use the stator current measurement, which is impractical in LC-filtered drives with long lead cables because of the sensor distance from the control unit. A more practical solution adopts only the converter current measurement, close to the converter output. Therefore, future development can be focused on modifying the control methods for the converter current measurement, as shown in the sensorless vector control for AC drives with an LC filter [11] and also in the observer-based current control for grid-connected converters with an LCL filter [45].

Other future work recommendations may include developing a linearized discrete-time model with distinguished control model parameters from plant model parameters, providing a more accurate and deeper stability analysis. Furthermore, the developed control structures could also include a parameter identification method for SM drives with the LC filter to estimate filter and motor parameters with sufficient accuracy. The existing algorithms could also be extended by high-frequency signal injection method [25] to improve operation at low speeds and standstill. The torque ripple at the rated speeds can be reduced by decreasing the converter flux linkage reference, thus preventing the converter voltage reference from reaching the maximum available voltage limit. The operation of the SM with the LC filter in the field-weakening region could also be considered. Future master's theses could develop an observer-based V/Hz control for parallel-connected SMs using a single frequency converter.

References

[1] IEA (2017), *World Energy Outlook 2017*. Paris: OECD Publishing, 2017, ISBN: 978-92-64-28230-8. [Online]. Available: https://iea.blob.core.windows.net/assets/4a50d774-5e8c-457e-bcc9-513357f9b2fb/World_Energy_Outlook_2017.pdf

[2] H. A. A. Awan, "Control Methods for Permanent-Magnet Synchronous Reluctance Motor Drives," Doctoral thesis, School of Electrical Engineering, 2019. [Online]. Available: http://urn.fi/URN:ISBN:978-952-60-8765-8

[3] A. Boglietti and M. Pastorelli, "Induction and synchronous reluctance motors comparison," in *2008 34th Annual Conference of IEEE Industrial Electronics*, 2008, pp. 2041–2044. [Online]. Available: http://dx.doi.org/10.1109/IECON.2008.4758270

[4] J. Pyrhonen, V. Hrabovcova, and R. S. Semken, *Electrical machine drives control: An introduction*. John Wiley & Sons, 2016, ISBN: 978-1119260455.

[5] M. Smochek, A. F. Pollice, M. Rastogi, and M. Harshman, "Long cable applications from a medium-voltage drives perspective," *IEEE Transactions on Industry Applications*, vol. 52, no. 1, pp. 645–652, 2016. [Online]. Available: http://dx.doi.org/10.1109/TIA.2015.2463760

[6] *DU/dt filters*, Muuntosähkö Oy Trafox, March 2021, rev6. [Online]. Available: http://www.trafox.fi/wp-content/uploads/2015/05/DUdtFilters_rev6.pdf

[7] M. I. Ansari and H. Misra, "Impact of sine-wave lc filter on two-level pwm vsi fed im drive considering the long leads," in *2020 21st National Power Systems Conference (NPSC)*, 2020, pp. 1–6. [Online]. Available: http://dx.doi.org/10.1109/NPSC49263.2020.9331949

[8] A. Frederiksen, "Sensorless vector control techniques for efficient motor control continues," Norwood, MA, p. 4, 2013, mS-2549. [Online]. Available: https://www.analog.com/media/en/technical-documentation/tech-articles/Sensorless-Vector-Control-Techniques-for-Efficient-Motor-Control-Continues-MS-2549.pdf

[9] F. Perez-Pinal, C. Nunez, and R. Alvarez, "A novel speed control approach in parallel-connected induction motor by using a single inverter and electronic virtual line-shafting," in *2005 IEEE 36th Power Electronics Specialists Conference*, 2005, pp. 1339–1345. [Online]. Available: http://dx.doi.org/10.1109/PESC.2005.1581803

[10] T. Batzel and K. Lee, "Electric propulsion with sensorless permanent magnet synchronous motor: implementation and performance," *IEEE Transactions on Energy Conversion*, vol. 20, no. 3, pp. 575–583, 2005. [Online]. Available: http://dx.doi.org/10.1109/TEC.2005.852956

[11] J. Salomäki, "Sensorless control of ac drives equipped with an inverter output filter," 2007. [Online]. Available: http://lib.tkk.fi/Diss/2007/isbn9789512291304/isbn9789512291304.pdf

[12] J. Liu, J. Dai, S. Royak, P. Schmidt, E. Al-nabi, and T. Nondahl, "Design and implementation of position sensorless starting control in industrial drives with output filter and transformer for oil/pump applications," in *2017 IEEE Applied Power Electronics Conference and Exposition (APEC)*, 2017, pp. 578–584. [Online]. Available: http://dx.doi.org/10.1109/APEC.2017.7930752

[13] Z. Li, Q. Zhang, H. Luo, H. Wang, J. Wang, F. Han, A. Wang, X. Liu, X. Yu, and L. Zhou, "Sensorless starting control of permanent magnet synchronous motors with step-up transformer for downhole electric drilling," in *IECON 2018 - 44th Annual Conference of the IEEE Industrial Electronics Society*, Oct 2018, pp. 689–694, ISSN: 2577-1647. [Online]. Available: http://dx.doi.org/10.1109/IECON.2018.8591852

[14] L. Tiitinen, M. Hinkkanen, J. Kukkola, R. Mikko, G. Pellegrino, and L. Harnefors, "Stable and passive observer-based V/Hz control for synchronous motors." in *Proc. IEEE ECCE*, Detroit, MI, Oct. 2022.

[15] L. Harnefors, M. Hinkkanen, O. Wallmark, and A. G. Yepes, "Control of voltage-source converters and variable-speed drives," p. 267.

[16] B. K. Bose, *Power Electronics and Variable Frequency Drives: Technology and Applications*. 345 East 47th Street, NY: IEEE PRESS, 1997, ISBN: 0-7803-1084-5.

[17] D. Holmes, T. Lipo, and T. Lipo, *Pulse Width Modulation for Power Converters: Principles and Practice*, ser. IEEE Press Series on Power Engineering. Wiley, 2003. [Online]. Available: https://books.google.fi/books?id=J5pTAAAAMAAJ

[18] B.-H. Bae and S.-K. Sul, "A compensation method for time delay of full-digital synchronous frame current regulator of pwm ac drives," *IEEE Transactions on Industry Applications*, vol. 39, no. 3, pp. 802–810, 2003. [Online]. Available: http://dx.doi.org/10.1109/TIA.2003.810660

[19] D. Van de Sype, K. De Gusseme, A. Van den Bossche, and J. Melkebeek, "Small-signal laplace-domain analysis of uniformly-sampled pulse-width modulators," in *2004 IEEE 35th Annual Power Electronics Specialists Conference (IEEE Cat. No.04CH37551)*, vol. 6, 2004, pp. 4292–4298 Vol.6. [Online]. Available: http://dx.doi.org/10.1109/PESC.2004.1354760

[20] M. Hinkkanen, "Lecture 11: Sensorless synchronous motor drives," Spring 2020, ELEC-E8402 Control of Electric Drives and Power Converters, Aalto University School of Electrical Engineering. [Online]. Available: https://mycourses.aalto.fi/pluginfile.php/1188836/mod_resource/content/13/lecture11.pdf

[21] A. Consoli, G. Scarcella, and A. Testa, "Industry application of zero-speed sensorless control techniques for pm synchronous motors," *IEEE Transactions on Industry Applications*, vol. 37, no. 2, pp. 513–521, 2001. [Online]. Available: http://dx.doi.org/10.1109/28.913716

[22] J.-I. Itoh, N. Nomura, and H. Ohsawa, "A comparison between v/f control and position-sensorless vector control for the permanent magnet synchronous motor," in *Proceedings of the Power Conversion Conference-Osaka 2002 (Cat. No.02TH8579)*, vol. 3, April 2002, pp. 1310–1315 vol.3. [Online]. Available: http://dx.doi.org/10.1109/PCC.2002.998163

[23] M. Farza, M. M'Saad, T. Ménard, A. Ltaief, and T. Maatoug, "Adaptive observer design for a class of nonlinear systems. application to speed sensorless induction motor," *Automatica*, vol. 90, pp. 239–247, 2018, ISSN: 0005-1098. [Online]. Available: https://www.sciencedirect.com/science/article/pii/S0005109817306453

[24] M. Hinkkanen, S. E. Saarakkala, H. A. A. Awan, E. Mölsä, and T. Tuovinen, "Observers for sensorless synchronous motor drives: Framework for design and analysis," *IEEE Transactions on Industry Applications*, vol. 54, no. 6, pp. 6090–6100, 2018. [Online]. Available: http://dx.doi.org/10.1109/TIA.2018.2858753

[25] A. Piippo and J. Luomi, "Adaptive observer combined with hf signal injection for sensorless control of pmsm drives," in *IEEE International Conference on Electric Machines and Drives, 2005.*, 2005, pp. 674–681. [Online]. Available: http://dx.doi.org/10.1109/IEMDC.2005.195796

[26] W. Villet and M. Kamper, "Position sensorless control of a reluctance synchronous wind generator drive with an lc inverter filter," *Electric Power Components and Systems*, vol. 43, 04 2015. [Online]. Available: http://dx.doi.org/10.1080/15325008.2015.1023909

[27] C.-M. Liang, Y.-J. Lin, J.-Y. Chen, G.-R. Chen, and S.-C. Yang, "Sensorless lc filter implementation for permanent magnet machine drive using observer-based voltage and current estimation," *Sensors*, vol. 21, p. 3596, 05 2021. [Online]. Available: http://dx.doi.org/10.3390/s21113596

[28] Y. Xu, M. Wang, W. Zhang, and J. Zou, "Sliding mode observer for sensorless control of surface permanent magnet synchronous motor equipped with lc filter," *IET Power Electronics*, vol. 12, no. 4, pp. 686–692, 2019. [Online]. Available: https://ietresearch.onlinelibrary.wiley.com/doi/abs/10.1049/iet-pel.2018.5218

[29] R. Sreejith and B. Singh, "Sensorless predictive current control of pmsm ev drive using dsogi-fll based sliding mode observer," *IEEE Transactions on Industrial Electronics*, vol. 68, no. 7, pp. 5537–5547, 2021. [Online]. Available: http://dx.doi.org/10.1109/TIE.2020.2996159

[30] F. Jukić, L. Pravica, T. Bariša, and D. Sumina, "Flying-start and continuous operation of a permanent-magnet wind generator based on discontinuous currents, discrete second-order sliding-mode observer and phase-locked loop," *IET Renewable Power Generation*, vol. 14, no. 1, pp. 90–99, 2020. [Online]. Available: https://ietresearch.onlinelibrary.wiley.com/doi/abs/10.1049/iet-rpg.2019.0461

[31] R. W. Hejny and R. D. Lorenz, "Evaluating the practical low-speed limits for back-emf tracking-based sensorless speed control using drive stiffness as a key metric," *IEEE Transactions on Industry Applications*, vol. 47, no. 3, pp. 1337–1343, 2011. [Online]. Available: http://dx.doi.org/10.1109/TIA.2011.2126013

[32] P. Perera, F. Blaabjerg, J. Pedersen, and P. Thogersen, "A sensorless, stable v/f control method for permanent-magnet synchronous motor drives," *IEEE Transactions on Industry Applications*, vol. 39, no. 3, pp. 783–791, 2003. [Online]. Available: http://dx.doi.org/10.1109/TIA.2003.810624

[33] S.-C. Agarlita, C.-E. Coman, G.-D. Andreescu, and I. Boldea, "Stable v/f control system with controlled power factor angle for permanent magnet synchronous motor drives," *IET Electric Power Applications*, vol. 7, no. 4, pp. 278–286, 2013. [Online]. Available: https://ietresearch.onlinelibrary.wiley.com/doi/abs/10.1049/iet-epa.2012.0392

[34] K. Yang, X. Yang, H. Xie, Y. Liu, Y. Zhang, and X. Wei, "Stable sensorless v/f and $cos\phi = 1$ control for permanent magnet synchronous motor drives," in *2014 17th International Conference on Electrical Machines and Systems (ICEMS)*, 2014, pp. 3564–3568. [Online]. Available: http://dx.doi.org/10.1109/ICEMS.2014.7014107

[35] C. Aijun and J. Xinhai, "A stable v/f control method for permanent magnet synchronous motor drives," in *2017 IEEE Transportation Electrification Conference and Expo, Asia-Pacific (ITEC Asia-Pacific)*, 2017, pp. 1–5. [Online]. Available: http://dx.doi.org/10.1109/ITEC-AP.2017.8080913

[36] Z. Tang, X. Li, S. Dusmez, and B. Akin, "A new v/f-based sensorless mtpa control for ipmsm drives," *IEEE Transactions on Power Electronics*, vol. 31, no. 6, pp. 4400–4415, 2016. [Online]. Available: http://dx.doi.org/10.1109/TPEL.2015.2470177

[37] D. Stellas, M. T. Hansen, T. Thiringer, T. Strømsvik, and H. B. Ulvestad, "Position-sensorless control of a submersible pmsm fed over a long cable and two transformers," in *2014 16th European Conference on Power Electronics and Applications*, 2014, pp. 1–10. [Online]. Available: http://dx.doi.org/10.1109/EPE.2014.6910696

[38] K. J. Astrom and R. M. Murray, *Feedback Systems: An Introduction for Scientists and Engineers*. USA: Princeton University Press, 2008, ISBN:0-691-13576-2, v2.11b(28.Sep.2012).

[39] M. S. Fadali and A. Visioli, "Chapter 9 - state feedback control," in *Digital Control Engineering (Third Edition)*, 3rd ed., M. S. Fadali and A. Visioli, Eds. Academic Press, 2020, pp. 387–439. [Online]. Available: https://www.sciencedirect.com/science/article/pii/B9780128144336000090

[40] T. Tuovinen, H. A. A. Awan, J. Kukkola, S. E. Saarakkala, and M. Hinkkanen, "Permanent-magnet flux adaptation for sensorless synchronous motor drives," in *Proc. IEEE SLED*, Helsinki, Finland, Sep. 2018, pp. 138–143.

[41] G. F. Franklin, J. D. Powell, and A. Emami-Naeini, *Feedback Control of Dynamic Systems*, 7th ed. USA: Prentice Hall Press, 2014, ISBN: 978-0-13-349659-8.

[42] P. Szczupak and M. Pacas, "Automatic identification of a pmsm drive equipped with an output lc-filter," in *IECON 2006 - 32nd Annual Conference on IEEE Industrial Electronics*, Nov 2006, pp. 1143–1148, ISSN: 1553-572X. [Online]. Available: http://dx.doi.org/10.1109/IECON.2006.347724

[43] B. L. Mbula and S. P. Daniel Chowdhury, "Performance improvement of synchronous reluctance motors: A review," in *2017 IEEE PES PowerAfrica*, 2017, pp. 402–406. [Online]. Available: http://dx.doi.org/10.1109/PowerAfrica.2017.7991258

[44] M. Hinkkanen, "Lecture 7: Control of a dc motor drive," Autumn 2019, ELEC-E8405 Electric Drives, Aalto University School of Electrical Engineering. [Online]. Available: https://mycourses.aalto.fi/pluginfile.php/1055630/mod_resource/content/13/Lecture7.pdf

[45] J. Kukkola and M. Hinkkanen, "Observer-based state-space current control for a three-phase grid-connected converter equipped with an lcl filter," *IEEE Transactions on Industry Applications*, vol. 50, no. 4, pp. 2700–2709, 2014. [Online]. Available: http://dx.doi.org/10.1109/TIA.2013.2295461

A Input parameters

Table A1: Data of the 2.2-kW 6-pole PMSM with the LC filter.

Motor - Rated values	
Voltage (line-to-neutral, peak value)	$\sqrt{2/3}$·370 V
Current (peak value)	$\sqrt{2}$·4.3 A
Frequency	75 Hz
Speed	1 500 rpm
Torque	14 Nm
Filter (B84143V0006R229) - Rated values	
Voltage (line-to-neutral, peak value)	300 V
Current (peak value)	$\sqrt{2}$·6 A
Operating motor frequency	0...100 Hz
Motor - Parameters	
Stator resistance R_s	3.6 Ω
d-axis inductance L_d	36 mH
q-axis inductance L_q	51 mH
PM flux linkage $\boldsymbol{\psi}_\mathrm{F}$	0.545 Wb
Total inertia J_m	0.015 kgm^2
Filter (B84143V0006R229) - Parameters	
Filter resistance R_f	290 $m\Omega$
Filter inductance L_f	8.5 mH
Filter capacitance C_f	2.2 μF
Resonance frequency f_r	1.16 kHz

Table A2: Data of the 6.7-kW 4-Pole SyRM with the LC filter.

Motor - Rated values	
Voltage (line-to-neutral, peak value)	$\sqrt{2/3}$·370 V
Current (peak value)	$\sqrt{2}$·15.5 A
Frequency	105.8 Hz
Speed	3 175 rpm
Torque	20.1 Nm
Filter (B84143V0025R229) - Rated values	
Voltage (line-to-neutral, peak value)	300 V
Current (peak value)	$\sqrt{2}$·25 A
Operating motor frequency	0...100 Hz
Motor - Parameters	
Stator resistance R_s	0.55 Ω
d-axis inductance L_d	46 mH
q-axis inductance L_q	6.8 mH
PM flux linkage $\boldsymbol{\psi}_\mathrm{F}$	0 Wb
Total inertia J_m	0.015 kgm^2
Filter (B84143V0025R229) - Parameters	
Filter resistance R_f	25 $m\Omega$
Filter inductance L_f	2.5 mH
Filter capacitance C_f	10.0 μF
Resonance frequency f_r	1.01 kHz

Table A3: Control parameters.

Sampling frequency f_s	8 kHz
Converter flux linkage reference $\boldsymbol{\psi}_\mathrm{c,ref}$	0.6411 Wb
Closed-loop controller bandwidth α_c	2π10 rad·s^{-1}
Load angle estimation bandwidth α_o	2π40 rad·s^{-1}
Converter current estimation bandwidth α_L	2π20 rad·s^{-1}
Bandwidth of LPF α_f	2π1 rad·s^{-1}
Damping gain of HPF g_τ	3 N^{-1}m^{-1}rad·s^{-1}
Damping gain of the LC filter g	0.5
Desired damping ratio at high speeds ζ_∞	0.7